Study of the interaction of plasma radicals with malignant tumor cells by means of Molecular Dynamics simulation

Proefschrift voorgelegd tot het behalen van de graad van doctor in de Wetenschappen aan de Universiteit Antwerpen te verdedigen door

Maryam Ghasemitarei

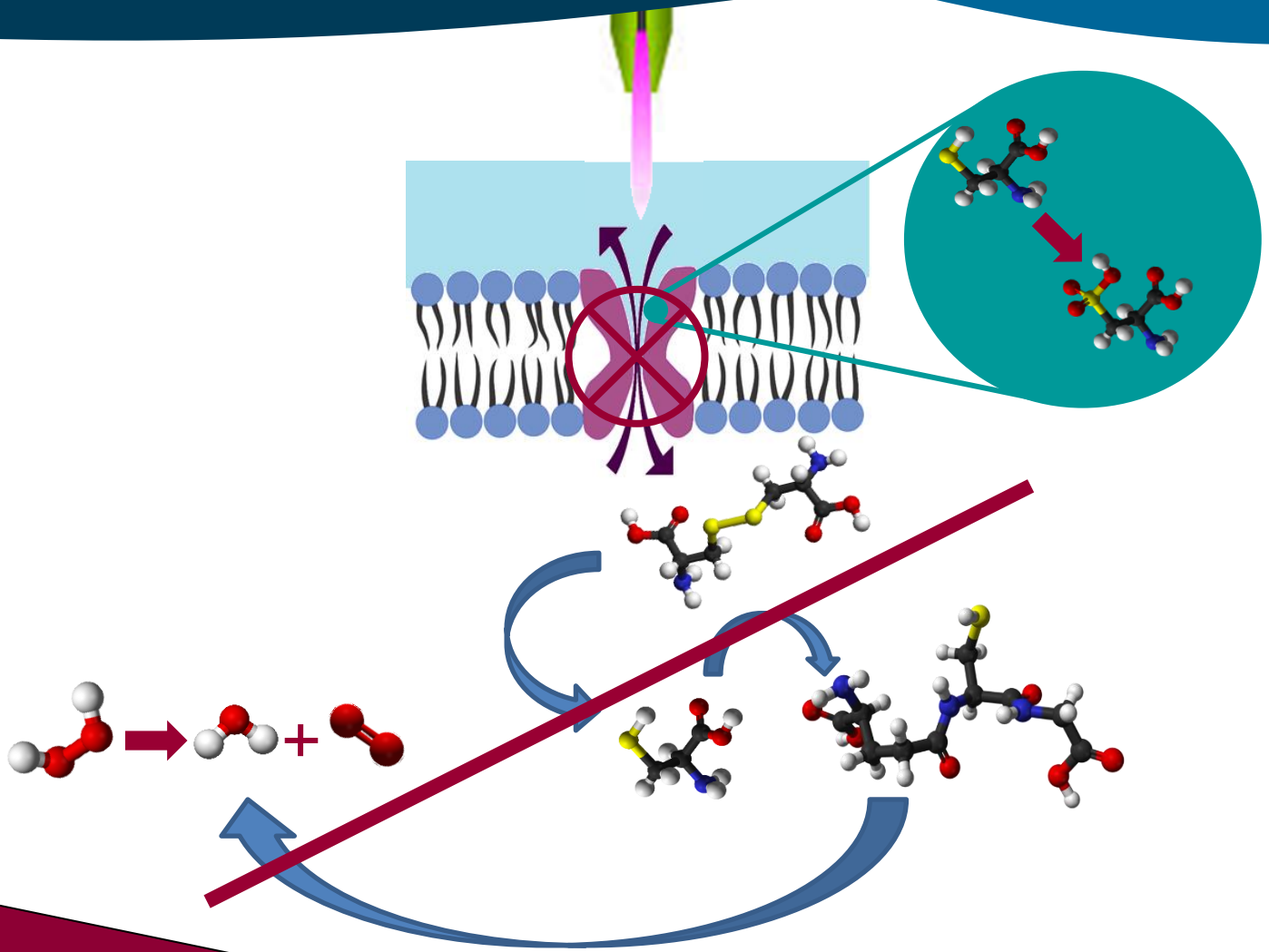

Promotoren
prof. dr. Annemie Bogaerts
prof. dr. Babak Shkri

Faculteit Wetenschappen
Departement Chemie
Antwerpen 2019

Universiteit Antwerpen

Faculteit Wetenschappen

Departement Chemie

Study of the interaction of plasma radicals with malignant tumor cells by means of Molecular Dynamics simulation

Studie van de interactie van plasma radicalen met kwaadaardige tumorcellen door middel van Moleculaire Dynamica simulatie

Proefschrift voorgelegd tot het behalen van de graad van doctor in de Chemie aan de Universiteit Antwerpen te verdedigen door

Maryam Ghasemitarei

Promotors: Prof. Dr. Annemie Bogaerts,

Prof. Dr. Babak Shokri

Tehran 2019

ACKNOWLEDGEMENTS ..... **V**

CHAPTER 1: BACKGROUND **1**

1.1 Introduction **2**

1.2 The role of ROS in cancer cells **3**
1.2.1 Characteristic of cancer cells 3
1.2.2 Cancer treatment by excessive ROS levels 4

1.3 Biochemistry of proteins **5**
1.3.1 Structure and characteristic of amino acids 6
1.3.2 pK_a values of amino acids 9

1.4 xC^- Antiporter **10**
1.4.1 Cystine uptake and glutathione 10
1.4.2 The xC^- antiporter as a target for therapy of cancer 12
1.4.3 Structure of xC^- antiporter 12
1.4.4 Upregulation of xC^- transporter in cancer cells 14

1.5 *CYC* uptake **15**
1.5.1 *CYC* uptake and *pH* 15
1.5.2 $O2$ and $H2O2$ dependency with *CYC* uptake 17
1.5.3 pH effects on cysteine oxidation 19

1.6 Aim of this study **22**

CHAPTER 2: COMPUTATIONAL METHODOLOGY **24**

2.1 Introduction **25**

2.2 Computer simulation methods **25**

2.3 Molecular Dynamics **27**
2.3.1 Molecular interaction 27
2.3.2 Integration algorithms 31
2.3.3 Force fields in MD simulations 33
2.3.4 Periodic boundary conditions (PBCs) 33
2.3.5 Thermodynamic ensembles 35
2.3.6 Thermostat and barostat 36
2.3.7 Steps of MD simulations 42

2.4 Steered MD (SMD) **42**
2.4.1 Constant velocity pulling 43
2.4.2 Constant force pulling 44

2.5 Targeted MD (TMD) **45**

2.6 Umbrella sampling (US) **47**

2.7 Conclusion 49

CHAPTER 3: INVESTIGATION OF THE STRUCTURE OF THE XCT SUBUNIT 50

3.1 Introduction 51

3.2 Preparation of the xCT subunit structure 53
3.2.1 Choosing the model systems 53
3.2.2 Preparation of the model systems 54
3.2.3 Validation of the model system 54

3.3 Computational details 56
3.3.1 MD simulation protocol 56
3.3.2 US simulations protocol 58

3.4 Determination of substrate binding site 60
3.4.1 Funnel radii of the OF, OCC and IF structures 60
3.4.2 Determination of the substrate binding site in the OF conformation. 61
3.4.3 Occlusion of the OF structure 63
3.4.4 Transition from the OCC to the IF structure 64

3.5 US simulations 65

3.6 Conclusion 67

3.7 Appendix 69

CHAPTER 4: OXIDATIVE STRESS ON CYC TRANSPORTATION 75

4.1 Introduction 76

4.2 Computational details 77
4.2.1 Model system 77
4.2.2 Molecular dynamics simulation protocols for investigation of *Cys*$_{327}$ oxidation. 77
4.2.3 Molecular dynamics simulation protocols for investigation of lipid peroxidation effects 79
4.2.4 Calculation of the funnel radii 80
4.2.5 Umbrella sampling (US) simulations 80

4.3 Investigation of CYC translocation from native and oxidized OF structure 81
4.3.1 Funnel radii analysis 81
4.3.2 Conformations of the native and oxidized OF structures 83
4.3.3 Analysis of the interaction energies 84
4.3.4 Free energy profiles (FEPs) 90

4.4 Investigation of CYC translocation from OF structure located in the native and oxidized POPC 91
4.4.1 Funnel radii analysis 91
4.4.2 Investigation of structures stability 92

4.5 Conclusion 93

4.6 Appendix 94

SUMMARY 98

SAMENVATTING 102

ACADEMIC CURRICULUM VITAE 106

List of publications included in this thesis 106

Conference contributions 106

BIBLIOGRAPHY 108

Acknowledgements

The accomplishment of this work would not be possible without the help and support of many people, to whom I wish to express my thankfulness.

First of all, I would like to express my sincere gratitude and deep respect to my supervisor and advisor, head of the research group PLASMANT, Prof. Dr. Annemie Bogaerts for her patience, motivation and knowledge. Annemie, thank you very much for giving me the opportunity of being in your group as a double PhD student. I am grateful for your trust, permanent encouragement and support which helped me to carry out my thesis, as well as for your useful scientific advices in completing and writing this dissertation. You are the most inspiring woman, who is the greatest, strongest and smartest one in every branch of her life. Your dynamism, manner, sincerity and vision have deeply inspired me. I could not have imagined having a better supervisor for my Ph.D study. I feel proud of having you as a supervisor. Thank you very much for your support and understanding!

I am deeply indebted to my other supervisor and advisor, Prof. Dr. Babak. Shokri. Babak, intimate thanks for your experienced guidance and confidence in my work. I want to express my big gratitude for everything you did to help me throughout the past years. Thank you very much for your belief in me!

I am especially thankful to Maksudbek Yusupov for all the work he did to improve this thesis, as well as my other publications. He was the best colleague I ever had, who supported and trusted me, while I was completely disappointed. And also, whenever I lost my self-confidence, he was the only one who motivated me. I also really appreciate all supports of Jamoliddin Razzokov, who helped me to do the umbrella sampling simulation parts of this thesis.

During my PhD, I spent an interesting time with the PLASMANT group members, Maryam Aghaei, Amin Jafarzadeh, Charlotta Bengtson, Fatme Jardali, Umedjon Khalilov, Priyanka Shaw and Parisa Nematollahi. I had great pleasure working with you! Maryam Aghaei, Friends are God”s way of taking care of us

I also wish to thank Luc Van‘t dack for the administrative and technical support, as well as the secretaries of the Chemistry Department, Fabiana Quiroz and Ingrid Swenters, for taking care of all non-scientific tasks.

The Turing HPC infrastructure at the CalcUA core facility of the Universiteit Antwerpen, a division of the Flemish Supercomputer Center VSC, funded by the Hercules Foundation, the Flemish Government (department EWI), and the Universiteit Antwerpen is also acknowledged for calculation support.

Special thanks go to my friends Amirshahriar Mashayekh and Parisa Shali for their useful ideas and scientific discussions, and most importantly for their friendship.

I am also forever in debt to my parents, Azam Naghibimahmoudabadi and Morteza Ghasemitarei, and my younger brother Hamidreza Ghasemitarei for their love and blessings, support and understanding, as well as their encouragements in every step of my life. You are the best family everyone wish to have.

Chapter 1: Background

1.1 Introduction

Cold atmospheric plasma (CAP) is applied frequently in biology and medicine in recent years [1]. Plasma is an ionized gas, consisting of neutral species (molecules, radicals and excited species), ions, electrons and photons [1, 2]. The treatment of dental cavities [3], blood coagulation, sterilization of tissue surfaces [4], cancer treatment [5] and wound healing [6] are some examples of CAP application in biology and medicine. Clearly, the complexity of plasma and also biological systems leads to the complex mechanisms of plasma interaction with living systems.

The composition and type of reactive species produced by CAP can be different for different conditions. For example, the plasma generator sources (e.g. DBD, plasma jet sources) and the external parameters of plasma (e.g., voltage, frequency and gas mixture composition) determine the combination of generated reactive species. Realizing the interaction mechanisms of these species with biochemical structures, as well as controlling the processes occurring in the plasma, can be helpful in finding an efficient ways to cure some diseases.

Particularly, in the last decade, CAP has shown a considerable anti-cancer capacity for various types of cancer cells [7]. CAP (or simply plasma) can selectively treat cancer cells, without damaging or having less damage to the normal cells [8-10]. Up to now, cancer cells have not yet developed resistance against plasma treatment [11-14]. The generally accepted theory about the anti-cancer ability of plasma is based on oxidative stress [15]. The reactive oxygen species (ROS) formed in plasma, which can also be generated by some other traditional anti-cancer therapies, are believed to be responsible for apoptosis in cancer cells. The different cell cycle of healthy and cancer cells [16], the higher concentration of ROS and RNS (i.e. reactive nitrogen species) found in cancer cells [17], the higher expression of aquaporin channels in cancer cell membranes [18, 19], and the different composition of lipids and cholesterol fraction in the membrane of healthy and cancer cells (i.e. cancer cells have a significantly lower concentration of cholesterol in their plasma membrane) [2] may explain why cancer cells are more vulnerable to plasma treatment. Another theory suggests that plasma species are able to attenuate the antioxidative system of cancer cells [20]. Some amino acids such as cysteine and tryptophan are the main targets of effective species in CAP. The oxidation of amino acids by CAP, especially the oxidation of the thiol group of *Cys* residue, can disturb the normal function of

some antioxidant enzymes [21]. Moreover, the ROS-induced protein modification can alter the protein structures and disrupt their function [22].

In particular, a recent study on CAP oxidation of the human epidermal growth factor demonstrated that the oxidation leads to a change in structural conformation of this protein as well as its binding affinity with the receptor [23]. Hence, in my study I will take another step towards the understanding of the selective anti-cancer capacity of plasma, based on the transmembrane protein xC^- antiporter.

In the following sections, a brief introduction of the role of ROS in cancer cells will be presented (section 1.2), as well as the biochemistry of proteins (section 1.3), the characteristic of transporters in general and the xC^- antiporter in particular (section 1.4), and the role of pH in cysteine uptake, in the presence or absence of ROS (section 1.5). Finally, the aim of this work (section 1.6) will be given.

1.2 The role of ROS in cancer cells

1.2.1 Characteristic of cancer cells

In general, the level of ROS in cancer cells is higher than in normal cells [17]. In fact, ROS are responsible for the preservation of the cancer phenotypes. Continuous ROS stress may induce adaptive stress responses. Therefore, cancer cells enable to survive with high levels of ROS [24]. Generally, ROS are parts of a signaling network of cells and can control cell functions, and proper levels of ROS play an essential role in the modulation of several physiologic responses. In cancer cells, excessive intracellular levels of ROS, as well as attenuation of the antioxidant system, can give rise to pathological conditions, and even encourage the progression of these conditions [25].

Persistence inducing oxidative stress is one of the main characteristics of cancer cells. A lot of factors support the preservation of a pro-oxidative cancer phenotype, such as the oncogenic transformation, alterations in metabolic activity and the loss of functional p53 [26]. Therefore, cancer cells require high levels of energy, amino acids, nucleotides and lipids as a result of increasing metabolic activity, preserving a high rate of cell growth and proliferation. Moreover, to

promote oxidative phosphorylation and glycolysis, a shift in cell metabolism is needed, which helps the cancer cells to survive and propagate easily [27]. In comparison with oxidative phosphorylation, producing ATP at a higher rate, but with lower efficiency by glycolysis, may selectively give advantage to cancer cells when competing for energy resources [28]. Cancer cells have complicated mechanisms to protect themselves from intrinsic oxidative stress and have a sophisticated adaptation system that essentially involves the rearrangement of the antioxidant functions and the upregulation of pro-survival molecules [29]. In comparison with normal cells, cancer cells have higher levels of antioxidant enzymes. Based on literature, in some cancer cells such as human ovarian [30], gastric and esophageal carcinomas [31], higher level of manganese-dependent superoxide dismutase (MnSOD) is observed. Moreover, increased expression of both SOD and catalase has been observed in primary human leukemia cells [31]. However, several lines of evidence strongly support the idea that increased antioxidant defenses are engaged by cancer cells to escape severe oxidative damage and to survive in the presence of intrinsic oxidative stress.

1.2.2 Cancer treatment by excessive ROS levels

High levels of ROS can damage and even kill cells. Although cancer cells have developed adaptive mechanisms to minimize the damage of oxidative stress, excessive levels of ROS can disturb redox homeostasis. Hence, by irreversibly damaging cellular macromolecules, including DNA, carbohydrates, proteins, and lipids [32], or by modulating redox-sensitive signaling proteins at the levels of signal transduction or transcriptional regulation, the cell viability will be affected. Proteins can be severely damaged by oxidative stress. Carbonylation, S-nitrosylation, glutathionylation, and tyrosine nitration are some ways of protein damage that can be happen by oxidative stress. Among protein oxidative modifications, carbonylation is extremely important, as it occurs at high levels in vivo and is often used as a marker of oxidative stress [24]. Carbonylations are formed either by a direct oxidative attack on the amino acid side chains of *Pro*, *Arg*, *Lys*, and *Thr*, or by an indirect reaction of the primary amino-group of *Cys*, *Lys*, and *His* with reactive carbonyl compounds or with carbonyl-containing oxidized lipids [33]. Carbonylation has two main effects. Firstly, heavily carbonylated proteins tend to form high molecular-weight aggregates that are resistant to degradation. They accumulate within the cell, as damaged or unfolded proteins that can also inhibit proteasome activity [34]. Secondly, carbonylation

can extremely alter both the structure and function of a variety of proteins. For instance, actin carbonylation causes the disruption of the actin cytoskeleton, leading to drastic cellular function impairments [35].

The most remarkable observation is related to the possibility of specifically targeting redox alterations, in order to ensure a good therapeutic selectivity for specific cancer cells. Disturbing the balance of redox homeostasis, as a result of exogenous compound effects that increase ROS generation or inhibit ROS elimination, accumulates excessive ROS in cancer cells. Hence, induction of cell damage or even cell death is observed in these cancer cells [24]. Several factors have been identified that promote ROS generation, such as mitochondrial electron transport chain modulators, redox-cycling compounds, inhibitors of SOD and catalase [36]. Moreover, disruption of antioxidant defenses, such as glutathione (i.e. GSH) depleting agents can be useful to generate excessive ROS [36]. Based on literature, overbalanced ROS as a result of GSH depletion in cancer cells leads to cancer cell death. GSH is one of the main cellular scavengers of free radicals, which is composed of three amino acids, i.e., *Glu*, *Cys* and *Gly*. These three amino acids play an important role in cell protection from drug-induced oxidative stress [37]. Inhibition of the xC^-, cystine/glutamate antiporter (see below in next section), may also deplete GSH by reducing the uptake of cystine, i.e. the oxidized dimer form of *Cys*; hence xC^- antiporter inhibitors are also interfered in the biosynthetic pathway of GSH [38]. The importance of this antiporter in the growth and progression of cancers has been demonstrated in human pancreatic cancer [39] as well as in small-cell lung cancer cell lines [40].

1.3 **Biochemistry of proteins**

Proteins are large and complex molecules that play a fundamental role in the body. They are needed for the structure, function, and regulation of the body's tissues and organs.

Proteins are composed of smaller units called amino acids, which are linked together in long chains. There are 20 different types of amino acids that can be combined together to make a protein. The sequence of amino acid twisted into a 3-D shape forms a protein, which has a specific function.

Proteins can be described based on their large range of functions in the body. Some important functions of proteins are listed in Table 1.1.

Table 1.1. List of some of the most important protein functions [41]

Function	**Description**
Enzymes	Enzymes are responsible for almost all of the thousands of intracellular chemical reactions. They also help to form a lot of new molecules by reading the genetic information stored in DNA
Antibody	Antibodies protect the body by binding to specific foreign particles, such as viruses and bacteria.
Messenger	Most important duties of messenger proteins, such as hormones, are transmitting signals and coordinating biological processes between different cells, tissues, and organs.
Structural component	These proteins are fibrous which provide cells and tissues with stiffness and rigidity. On a larger scale, they also allow the body to move.
Transport/storage	These proteins bind and carry atoms and small molecules within cells and throughout the body.
Translocation of ions/amino acids from membrane	These proteins are transmembrane proteins (TP), which permit the transport of special substrates (e.g., ions, amino acids) across the membrane. Their significant conformational changes lead to move the substrates through the membrane.

1.3.1 Structure and characteristic of amino acids

Amino acids are organic molecules, consisting of a basic amino group (—NH_2), an acidic carboxyl group (—COOH), and an organic R group (or side chain). The difference between different amino acids is related to their side chain. Each molecule contains a central carbon (C) atom, called the Cα, to which both an amino and a carboxyl group are attached. The remaining two bonds of the Cα atom are generally saturated by a hydrogen atom and the R group [41].

In general, there are 20 amino acids in nature, which are categorized in five different groups (see Figure 1.1)

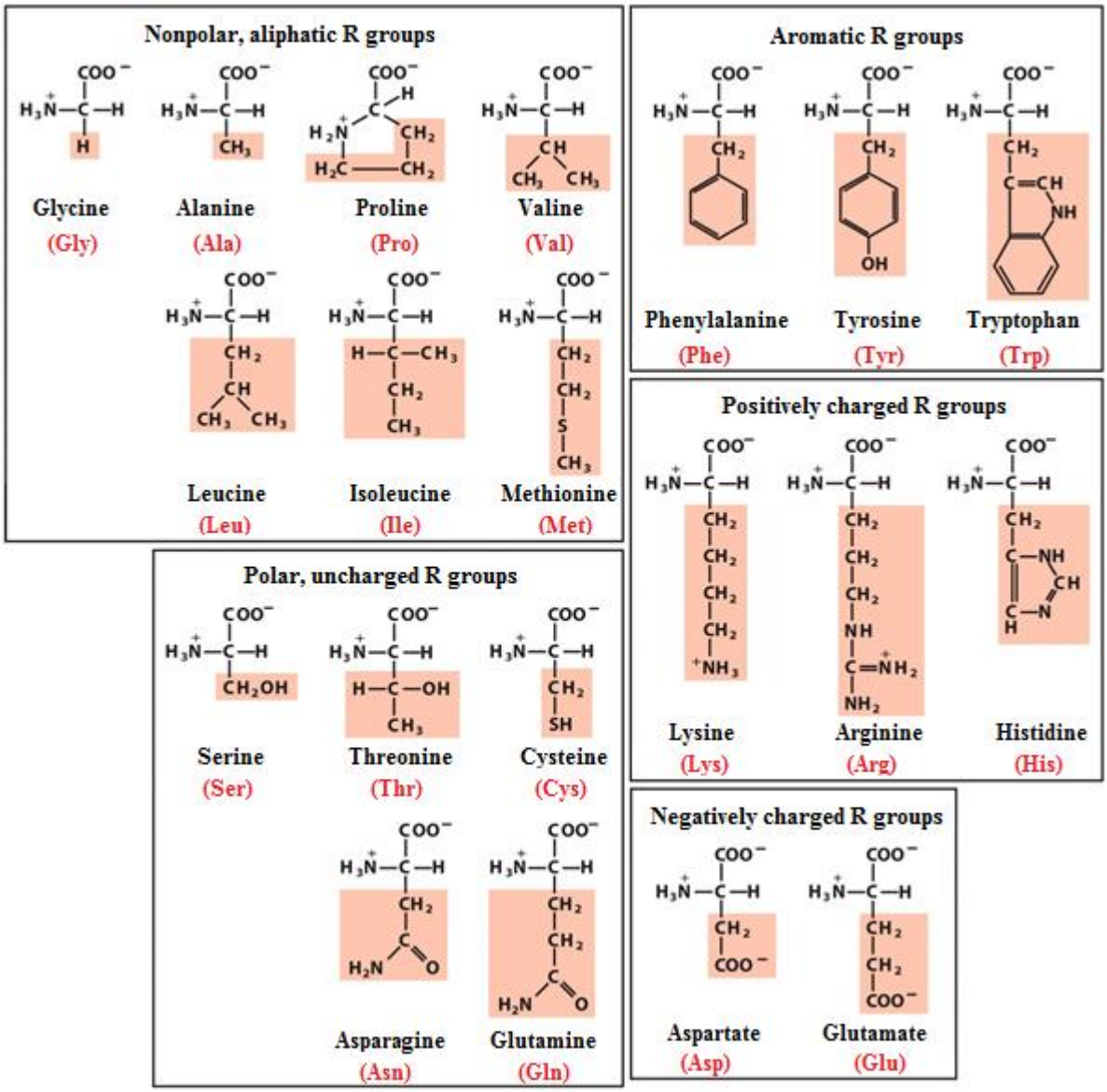

Figure 1.1. Schematic structures of the 20 amino acids found in nature, which are categorized in five different groups as a result of their side chains characteristics. Figure is adopted from[41].

Nonpolar, Aliphatic R groups

The R group of the amino acids in this group is nonpolar and hydrophobic. The hydrophobicity of these amino acids increases with increasing number of C atoms in the hydrocarbon chain.

Gly has the simplest and smallest side chain, and cannot contribute to the interactions driven by the hydrophobic effect. On the other hand, in protein structures, the side chains of *Ala*, *Val*, *Leu* and *Ile* tend to cluster together, stabilizing the protein structure through the hydrophobic effect. Among these amino acids, *Ala* is a special one, containing a methyl group as a side chain, which can hardly be involved in the function of proteins [42].

The thioether group of *Met* is slightly nonpolar, which can make a disulfide bridge bond (S-S) with other sulfur-containing amino acids, such as another *Met* and *Cys* [41].

Pro has an aliphatic side chain with a distinctive cyclic structure. The secondary amino (imino) group of *Pro* residue is held in a rigid conformation that reduces the structural flexibility of polypeptide regions containing *Pro*.

Aromatic R groups

Aromatic amino acids have unique and important properties. *Phe*, *Tyr*, and *Trp*, with their aromatic side chain (i.e. benzene ring) are generally hydrophobic, having an additional characteristic compared to simpler hydrophobic residues, such as *Leu* or *Val*. Although all aromatic amino acids can contribute to the hydrophobic effect, the nitrogen of *Trp* indole ring and hydroxyl group of *Tyr* can make a hydrogen bond. Hence, *Tyr* and *Trp* are significantly more polar than *Phe* [41].

Moreover, aromatic amino acids are substantially overrepresented at protein binding sites because of their capability to have cation-π interaction, a strong, noncovalent binding interaction. The cation-π interaction is a general binding force that could be formed between the benzene and the cations. In fact, the side chain of the aromatic amino acids makes a surface of negative electrostatic potential, and can bind to the positively charged amino acids [43].

Polar, uncharged R groups

The R groups of these amino acids are hydrophilic. Indeed, they can dissolve in water easier than nonpolar amino acids because of their functional group that forms a hydrogen bond with water. The hydroxyl groups of *Thr* and *Ser* side chain as well as the amide groups of *Asn* and *Gln* side chains are polar. Therefore, they are categorized in the polar group. *Cys* is an outlier here. The polarity of *Cys* is quite modest because of its sulfhydryl group. *Cys* is a weak acid and can make weak hydrogen bonds with oxygen or nitrogen. *Cys* can easily be oxidized to form a covalently linked dimeric amino acid called Cystine (i.e. *CYC*), in which two *Cys* molecules or residues are joined by a disulfide bond. The disulfide-linked residues are strongly hydrophobic (nonpolar). Disulfide bonds play a special role in the structure of many proteins by forming covalent links between parts of a polypeptide molecule or between two different polypeptide chains.

Positively (Basic) and negatively (Acidic) charged R groups

Amino acids of these two groups are the most hydrophilic R groups. The second primary amino group of the *Lys* side chain makes it the strongest positively charged amino acid at $pH = 7.0$. A guanidinium group of *Arg* with positive charge categorizes it in the positively charged R group. On the other hand, *His* with an aromatic imidazole group as a side chain with pK_a near neutrality can be positively charged (protonated form) or uncharged at $pH = 7.0$. The *His* residues facilitate many enzyme-catalyzed reactions by serving as proton donors/acceptors [41].

The two amino acids having a second carboxyl group with a net negative charge at $pH = 7.0$ are *Asp* and *Glu* [41].

1.3.2 pK_a values of amino acids

The pK_a is a measure of the tendency of a group to give up a proton, with the tendency decreasing tenfold as the pK_a increases by one unit.

Among the 20 natural amino acids, only 7 amino acids have functional side chains and are able to change their charges at different *pH*. Table 1.2 shows the side chain pK_a of these amino acids, which determines the expected charge of each residue at specified pH.

Table 1.2. pK_a values and charges of 7 functional amino acid side chains [44].

Amino acid	pK_a value Side chain	Side chain charge $pH = 7$	Side chain charge $pH \leq pK_a$	Side chain charge $pH \geq pK_a$
Arg	12.48	+1	+1	0
His	6.00	0	+1	0
Lys	10.53	+1	+1	0
Asp	3.65	−1	0	−1
Glu	4.25	−1	0	−1
Tyr	10.07	0	0	−1
Cys	8.18	0	0	−1

Based on literature, the *pH* value of the extracellular milieu of cancer cells are mostly between 5 and 7 ($5 < pH < 7$) [45, 46]. Hence, based on the side chain pK_a of amino acids, the charge of each residue will be different at

different *pH*. In this situation (in cancer cells), *His* residue is the only amino acid of which the charge can be changed in acidic *pH* environment.

1.4 xC^- Antiporter

1.4.1 Cystine uptake and glutathione

The cell membrane is a complex biomolecular structure, containing mostly proteins and lipids. Among the important proteins, transporters are essential for transporting small molecules, such as amino acids and ions, which are physiologically crucial for some processes. In neurotransmission [47], the efflux of toxic compounds [48] and the regulation of glucose [49], transporters play an important role. Transporters have a range of functions and are categorized into two main groups: primary and secondary active transporters (see transporter classification database on www.tcdb.org [50]), based on whether the transport function is regulated by chemical energy or a cellular electrochemical gradient, respectively. The secondary active transporters can be grouped into three general categories [51, 52], i.e., uniporter, symporter and antiporter. Uniporters mediate the transport of one molecule or ion, symporters carry two different ions or molecules in the same direction through the membrane, while antiporters transfer two different molecules (e.g., two specific amino acids) or ions through the membrane in opposite directions.

Antiporters play a key role in the preservation and proper functioning of some amino acid-dependent cellular processes, such as the energy metabolism, protein synthesis and cell protection [53]. The cells cannot sufficiently synthesize certain amino acids, and hence, for cell growth and viability, these amino acids need to be supplied from extracellular space.

One of the amino acids, vital for both normal and malignant cells, is *Cys* or its oxidized dimer form, cystine (*CYC*) [54, 55]. *Cys*/*CYC* is essential for general protein biosynthesis, specifically GSH. Since intracellular GSH has a short half-life, *CYC* uptake is of high value for the cell viability [56, 57].

Two distinct mechanisms for *CYC* uptake by normal cells have been reported [38]. 40-50% of *CYC* uptake is mediated by γ-glutamyl transpeptidase, which is located on the outer surface of the cell membrane and part of the γ-glutamyl cycle. The other 50-60% is thought to be provided by xC^- antiporter, which is a so-called electroneutral, anionic *CYC-Glu* transporter [38, 58]. Indeed, the anionic forms of extracellular *CYC* and intracellular *Glu* exchange with a stoichiometry

of 1:1[53, 59], and thus, no net charge is transported across the membrane. Figure 1.2 shows the schematic representation of this exchange.

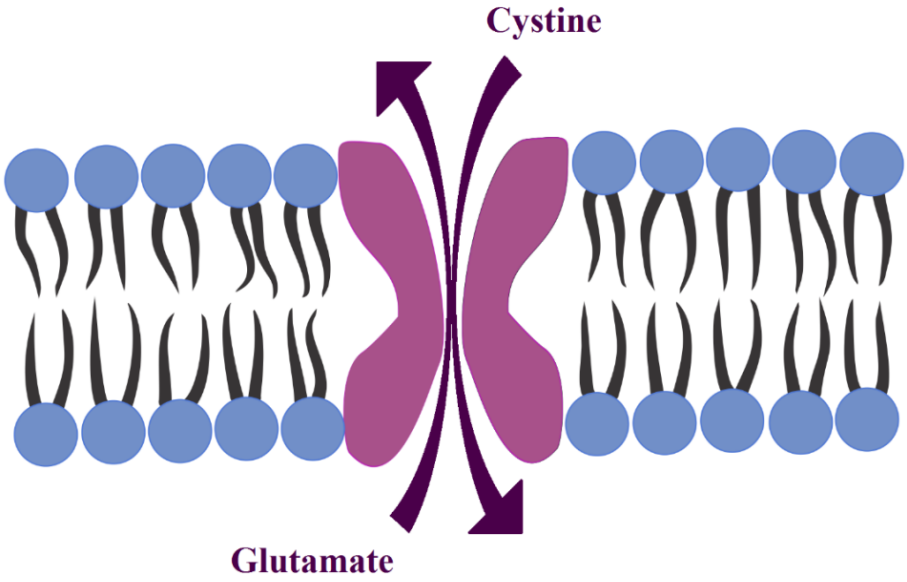

Figure 1.2. Schematic representation of amino acid exchange through xC⁻ antiporter

The xC⁻ antiporter has two important functions. Firstly, it assists with extracellular *CYC* uptake, increasing the intracellular level of GSH, which helps to protect cells from oxidative stress. Secondly, it helps to balance extracellular *CYC* and *Cys*, which is important for proliferation of T cells [60]. T cells (or T lymphocytes) play a central role in cell-mediated immunity.

After passing through the xC⁻ atiporter, *CYC* is reduced to *Cys* and is incorporated into the GSH structure. As mentioned before, GSH, a tripeptide thiol, plays an important role in cell protection from drug-induced oxidative stress as a free radical scavenger and detoxifying agent [38]. GSH is present at millimolar concentrations, and it works either as a nucleophile for efficient detoxification of reactive electrophiles, or as an antioxidant [24]. *CYC* uptake by xC⁻ antiporter can occur more frequently in two cases, i.e., (a) as a result of a low level of intracellular *CYC* compared to the extracellular level and (b) because of the high concentration of intracellular *Glu*. The latter can take place due to the transport of *Glu* by the *Ala-Ser-Cys* (ASC) transporter into the cell [38].

1.4.2 The xC^- antiporter as a target for therapy of cancer

The xC^- antiporter plays a critical role in many diseases, especially in cancer [61-63]. It has been reported that some cancer cells such as leukemia and lymphoma, are not able to synthesize *Cys* [64, 65]. This could be caused by the lack of γ-cystathionase, which is the enzyme that breaks down cystathionine to *Cys*, α-ketobutyrate, and ammonia. As a result, extracellular *CYC* uptake by e.g., the xC^- antiporter becomes important for cancer cell growth and viability. Since lymphoid cells cannot synthesize endogenous *Cys*, and *CYC* uptake in extracellular acidic *pH* conditions of cancer cells is depleted, they generally cannot have high *CYC* uptake (see section 1.5). Therefore, upregulation of xC^- activity in cancer cells is observed, which preserves the antioxidant defense.

Thus, cancer cells can uptake *CYC* directly by expressing the xC^- antiporters. As a consequence, the importance of these transporters could make them a cancer therapy target [66-68]. *CYC* uptake could be interrupted by inhibiting these transporters, which would reduce GSH synthesis, and thus, the cellular protection from oxidative stress, eventually leading to reduced viability and growth in cancer cells [69]. This antiporter also contributes to cancer cell drug resistance: *CYC* uptake enhances the biosynthesis of GSH which mediates the cellular detoxification of drugs. As a result, the inhibition of the xC^- antiporter, and consequently, reduction of GSH, not only inhibits cancer cell growth [70], but also reduces drug resistance [38, 71, 72].

Previous studies have shown that the viability of lymphoma and leukemia cells critically depends on the extracellular *CYC*/*Cys* concentration, and that the depletion of this amino acid in circulation can provide a useful therapeutic approach for these malignancies [38, 68, 73].

1.4.3 Structure of xC^- antiporter

Structurally, the xC^- antiporter is a member of the heteromeric amino acid transporter (HAT) family. These transporters are made of a light subunit (i.e. LSHAT) that belongs to the LAT family (i.e., the family of L amino acid transporters), and a heavy subunit (i.e. HSHAT) coupled to the light subunit by a disulfide bridge [74, 75]. The LAT family has 12 transmembrane (TM) domains and is non-N-glycosylated (see Figure 1.3) [52, 76]. The light and heavy subunits have different functions: the heavy subunit is involved in maintaining the entire

antiporter structure in the plasma membrane, while the light subunit is responsible for the transport [74, 75].

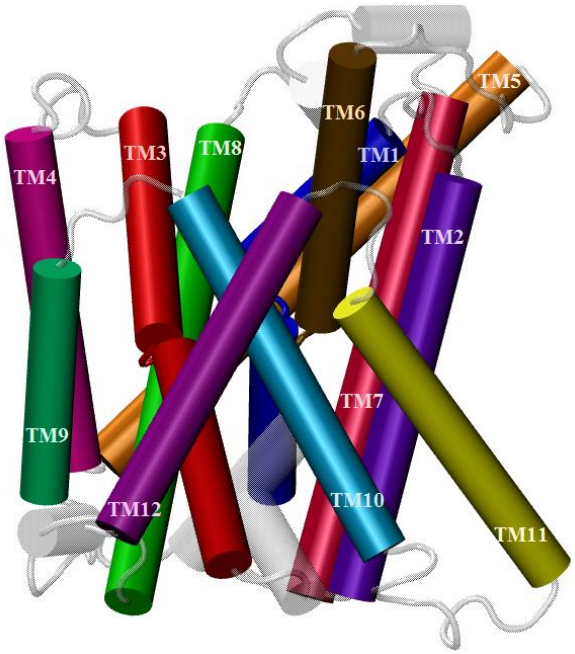

Figure 1.3.The 12 transmembrane (TM) domains of the light subunit of the xC⁻ antiporter

In the case of the human xC⁻ antiporter, a heavy subunit, determined 4F2hc, is coupled to xCT, a light subunit [74, 75]. The 4F2hc subunit is a type II membrane glycoprotein, commonly expressed in cells. This kind of HSHAT acts as a subunit for various amino acid transporters. It may be noted that the 4F2hc subunit of xC⁻ can be replaced by rBAT, another HSHAT, without any changes of the xC⁻ antiporter activity.

The previous studies indicated that the xCT subunit is responsible for transport of *CYC* and *Glu*, since the 4F2hc subunit, which has only a single transmembrane domain, is probably incapable of transport activity by itself [38]. Structural studies indicate that, similar as for other LAT family, the xCT subunit has 12 TM domains (TMDs) (see Figure 1.3). Moreover, a re-entrant loop between TMD 2 and 3 appears to participate in substrate binding and/or permeation [61].

Furthermore, *Cys* mutants generated via site-directed mutagenesis in some studies, revealed that Cys_{327} in the 8th putative TM domains of xCT is functionally the most important residue, accessible from the extracellular milieu and structurally linked to the permeation pathway and substrate-binding site.

Besides, it was shown that *Cys* residues of 4F2hc are not essential for transport activity. The expression of xCT together with 4F2hc *Cys*-less did not extremely affect the transport function, while as a result of interaction of thiol group of Cys_{327} of xCT subunit with *p*-chloromercuribenzoic acid (PCMB), the *CYC*/*Glu* transport was inhibited [77].

1.4.4 Upregulation of xC^- transporter in cancer cells

During tumor formation multiple cellular stresses, such as amino-acid deprivation, hypoxia, endoplasmic reticulum (ER) stress and high expression of Myc (i.e., a family of regulator genes and proto-oncogenes that code for transcription factors), lead to the inhibition of nonsense-mediated RNA decay (NMD). NMD is a main function to reduce errors in gene expression by eliminating mRNA transcripts that contain premature stop codons. Although NMD is originally responsible for the rapid degradation of mutated mRNAs, it also degrades selected non-mutated mRNAs, including multiple mRNAs which encode proteins that play a role in cellular stress responses [78].

Many of the mRNAs are upregulated when NMD is disabled and the suppression of NMD increases the intracellular concentrations of many amino acids. The regulation of the amino-acid metabolism has an important role in cancer, and particularly in metabolically stressed tumors, where they can serve as alternative sources of energy and, through the import of *Cys*, generate GSH to scavenge ROS [79].

Based on literature, the regulation of SLC7A11, which encodes for a subunit of the xCT transport system, has a significant role in cancer therapeutics. Reducing the amount of SLC7A11 decreases the intracellular GSH levels and increases the ability of several chemotherapeutic agents [80].

In cancer cells, SLC7A11 is upregulated as a result of cellular stress and NMD inhibition. The mRNAs of multiple genes which are responsible for amino-acid transport, are increased as a result of NMD inhibition. SLC7A11 is a direct NMD target and the inhibition of NMD by cellular stress has a significant contribution to the upregulation of SLC7A11 mRNA. Although upregulation of some kinds of mRNA, such as SLC7A11 mRNA, because of inhibition of NMD activity is observed, it is not necessary to see this upregulation in their encoded proteins. However, studies have shown that the stress-induced changes of

SLC7A11 mRNA are also reflected at the level of protein expression. SLC7A11 mediated intracellular transport of *CYC* is regulated by stress-induced inhibition of NMD. SLC7A11 is a component of the xCT transport system, which is responsible for intracellular *CYC* import [81]. In fact, xCT upregulation has been demonstrated at both mRNA and protein level in lymphomas, gliomas and pancreatic cancers [39, 59].

1.5 *CYC* uptake

1.5.1 *CYC* uptake and *pH*

Uncontrolled proliferation of cancer cells which consequently leads to significant metabolic changes, is a main mechanism in tumorigenesis. Cancer cells are able to upregulate anaerobic glycolysis, even in the presence of oxygen. Glycolysis is the pathway that converts glucose to pyruvate, which is useful to supply free energy to form high energy molecules, i.e., adenosine triphosphate (ATP) and nicotinamide adenine dinucleotide, bonded by a hydrogen atom (NADH). The anaerobic glycolysis stimulates the conversion of pyruvate to lactic acid [82]. To allow multiplication through continuous glycolysis and avoid acid-induced apoptosis, cancer cells develop mechanisms to decrease the extra lactic acid. Thus, several plasma membrane transporters and exchangers have been involved in the preservation of the intracellular *pH* of cancer cells, by exporting the accumulating acid (i.e. lactic acid) to the extracellular environment. Acidification of the extracellular milieu is the result of this process [83], leading to a decrease of the *CYC* uptake by xC^- antiporter of cancer cells. Because of the importance of *CYC* for cancer cell viability, the upregulation of the xCT subunit of the xC^- antiporter has been demonstrated in some cancers, as mentioned in last section.

Based on literature, the significant difference in the *pH* dependency of the *CYC* uptake and *Glu* removal seems to be related to different ionic states of *CYC* and *Glu* [38, 46, 84] . Studying the *pH* effects reveals that the carboxyl groups of these amino acids are fully dissociated, whereas the amino groups are not always protonated. The amino group of *Glu* is almost fully protonated at $5.8 < pH < 8.0$, since its pK_a value is 9.67. In contrast, the pK_a values of two amino groups of *CYC* are 7.48 and 9.02. From these values, three different kinds of *CYC* with different concentration are formed in the extracellular milieu, i.e., *CYC* with two carboxylate groups and two protonated amino groups (*CYC*-I), *CYC* with two carboxylate groups and one protonated and one neutral amino group (*CYC*-II) and

CYC with two carboxylate groups and two neutral amino groups (*CYC*-III). The relative concentrations of these different ionic forms of *CYC* as a function of *pH* are shown in Figure 1.4.

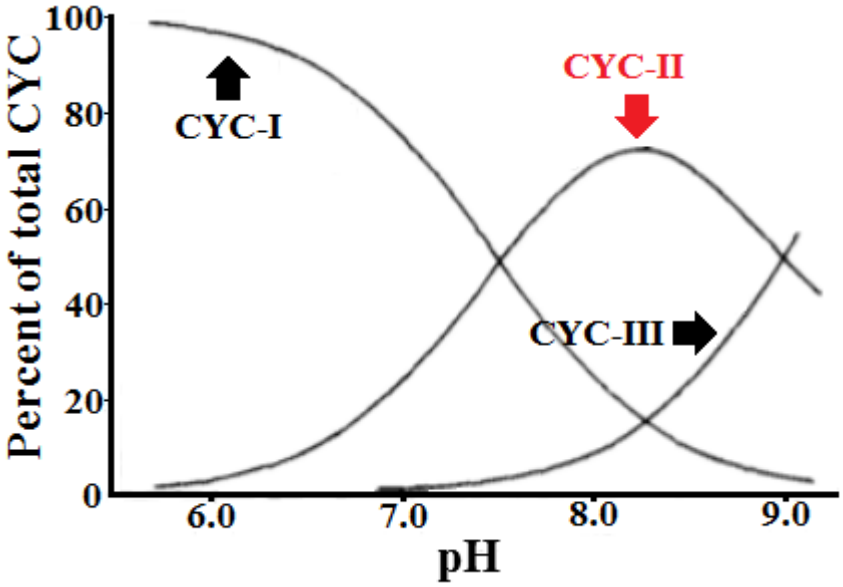

Figure 1.4. Concentration of the different ionic forms of CYC as a function of pH. Figure is adopted from [84].

It is obvious that the relative concentration of *CYC*-II increases as a result of increasing *pH*, up to $pH = 8.2$. Investigation of *CYC* uptake shows that *CYC*-II is the only one that is transportable through xC^- antiporters [84], because of some reasons such as the change in the concentration of *CYC*-II as a function of *pH* is well correlated with the *pH* profile for *CYC* uptake.

In addition, in another study, the *pH* dependency with *CYC* uptake was mentioned. The *pH* profiles of the *CYC* and *Glu* transport induced by the xC^- system in oocytes are shown in Figure 1.5. *CYC* transport is significantly dependent on *pH*. In acidic and basic *pH* range, *CYC* uptake increases and decreases as a result of increasing *pH*, respectively. On the other hand, *Glu* translocation was almost independent of the *pH*, although a tendency of translocation decreases in basic *pH* range [46].

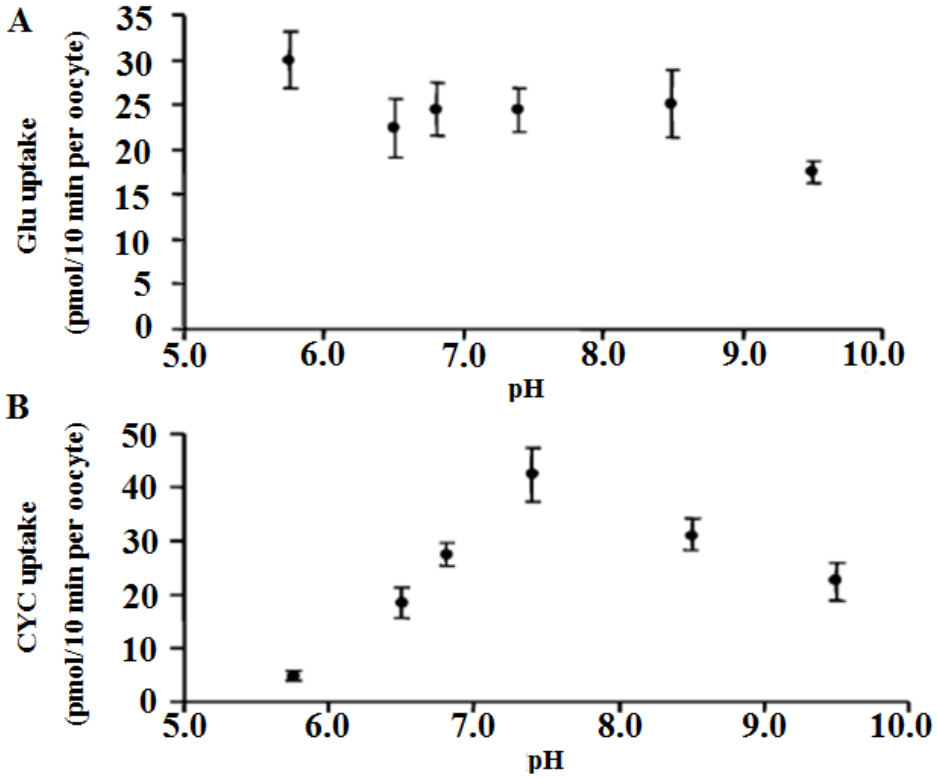

Figure 1.5. pH profile of (A) Glu and (B) CYC uptake by xC^- antiporter was determined for 10 min at different pH values (5.75, 6.5, 6.8, 7.4, 8.5 and 9.5) for oocyte. Figure is adopted from [46].

As a result, *CYC* transport showed a marked dependence on *pH* with an optimum of about 7.5. In contrast, *Glu* transport was almost independent of pH. Although *Glu* inhibited *CYC* uptake independently of *pH*, *CYC* inhibited *Glu* uptake in a *pH*-dependent manner [38].

1.5.2 O_2 and H_2O_2 dependency with *CYC* uptake

The transport of amino acids such as *CYC* is sensitive to environmental changes. In contrast to large concentration of intracellular *Glu*, the intracellular concentration of *CYC* is negligibly small, and it justifies that the physiologic transport via xC^- system is the entrance of *CYC* and the exit of *Glu*. The cycle consisting of the entrance of *CYC*, the intracellular reduction of CYC to *Cys*, the exit of *Cys* by neutral amino acid transport systems (ASC system), and the extracellular oxidation of *Cys* to *CYC*, can explain the reason of negligible intracellular *CYC* levels. This cycle is driven not only by the intracellular activities, but also by the redox state in the extracellular milieu [85].

Some investigations have expressed that the transport activity for *CYC* is induced by oxygen. Based on the studies of Bannai et al., the *CYC* transport of cultured human fibroblasts is decreased under a low oxygen concentration. Table 1.3 shows the rate of *CYC* uptake of cells cultured in ambient air and hypoxia in the different interval times. In this study, after the incubation for 48 h under 3% oxygen, the *CYC* transport was decreased to less than one-third of that of the control cells (see Table 1.3). The *CYC* transport increased by 50% after exposure of the cells to hyperoxia (40% oxygen) [85].

Table 1.3.The rate of CYC uptake in the cell cultured under 3% oxygen

Rate of CYC uptake (nmol/min/mg protein)	Culture condition for the experiments
0.99±0.22	Under room air for 2 days
0.57±0.10	Under 3% oxygen for 1 days
0.23±0.05	Under 3% oxygen for 2 days

This study has shown that the activity of the *CYC* transport, which could represent the activity of the xC^- system, is inducible by oxygen.

Furthermore, the effect of H_2O_2 on the *CYC* uptake is investigated in this study. Figure 1.6 indicates the effect of oxygen concentration on the induction of the *CYC* transport activity by various stimuli. In this figure, glucose oxidase enzyme is an oxido-reductase that catalyzes the oxidation of glucose to hydrogen peroxide (i.e. H_2O_2) and D-glucono-δ-lactone [85].

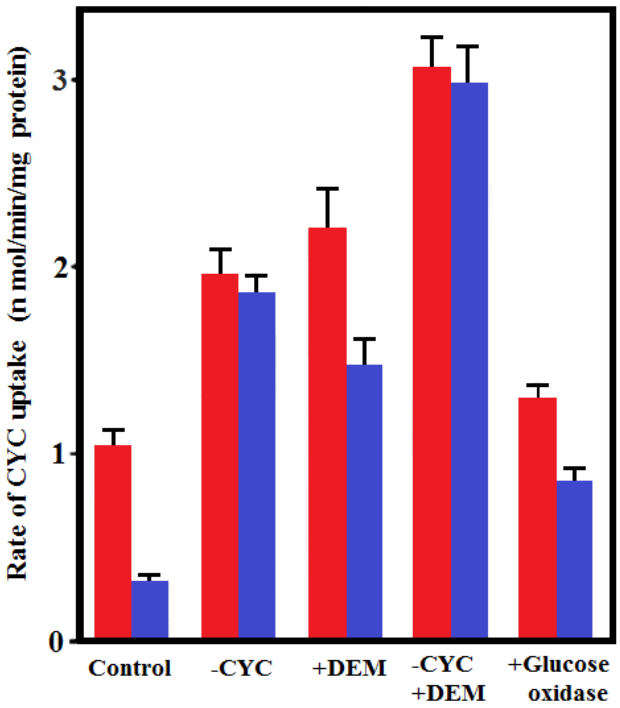

Figure 1.6. Effect of oxygen concentration on the induction of the CYC transport activity by various stimuli. Blue color bars, previously cultured cells under 3% oxygen were plated in dishes and cultured for 2 days under 3% oxygen (control). Red color bars, the cells routinely cultured under ambient air conditions were used. For the last 24 h in the culture, the cells were exposed to the CYC-free medium (-CYC) and/or 0.1 mM diethyl maleate (+DEM); for the last 42 h in the culture the cells were exposed to 2.5 milliunits/ml glucose oxidase (+Glucose oxidase). They were then assayed for the uptake of CYC (0. 05 mM). Figure is adopted from [85]

The results of glucose oxidase reveal that, under ambient air conditions, the *CYC* uptake was enhanced slightly by glucose oxidase relative to the control group, whereas under 3% oxygen the uptake was enhanced strongly by glucose oxidase. Thus the apparent effect of oxygen became less marked if glucose oxidase was present.

1.5.3 pH effects on cysteine oxidation

Oxidation of amino acid residues in various physiological and pathological conditions, such as aging, oxidative stress, and impairment of some biological functions, is able to induce protein modification. Although all amino acids can be biologically oxidized, the sulphur containing amino acids, such as *Cys* and *Met*, are readily oxidized by ROS and RNS [86]. The *Cys* oxidation pathway depends significantly on both the nature of the oxidant and the reaction conditions such as *pH*. Previous studies show that in basic *pH* and in the presence of H_2O_2, cysteine

oxidizes to cysteine sulfonic acid [87, 88] (see third structure in Figure 1.7). In acidic *pH*, and in the presence of hydroxyl radical (OH°), H_2O_2 and superoxide (O_2^-), which all are found in CAP, *Cys* is oxidized to cysteic acid [88] (see forth structure in Figure 1.7). These two kinds of oxidation are biologically irreversible reactions, while the oxidation of cysteine to *CYC* in neutral *pH* is a completely reversible reaction.

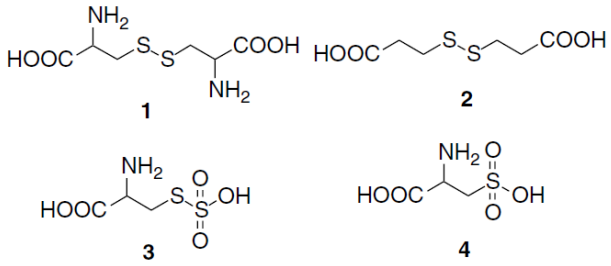

Figure 1.7. The schematic structure of all products of Cys oxidation: the structure of D, L-CYC (1) and its analog, 3,30-dithiobis(propionic acid) (2), as well as cysteine sulfonic acid, as a result of Cys oxidation in basic pH and in front of H_2O_2 (3) and cysteic acid as a result of Cys oxidation in acidic pH and in front of OH°, H_2O_2 and O_2^- (4). Figure is adopted from[87]

The experimental investigation of *Cys* oxidation by boron-doped diamond and glassy carbon electrodes revealed a change in the oxidation mechanism of *Cys* with increasing the *pH* of the electrolyte solution. The oxidation potential is pH dependent and decreases as a result of increasing *pH*. Although for $pH < 4.2$ the oxidation mechanism is *pH* independent. In acidic medium, *Cys* is present in the form of a cation, and consequently, protonated amino groups take part in the process, making cysteic acid as a main final oxidation product. Figure 1.8 shows a process of *Cys* oxidation to disulfides (i.e. *CYC*), which is a reversible reaction, and to cysteic acid, which is an irreversible reaction, under physiological condition [87, 88].

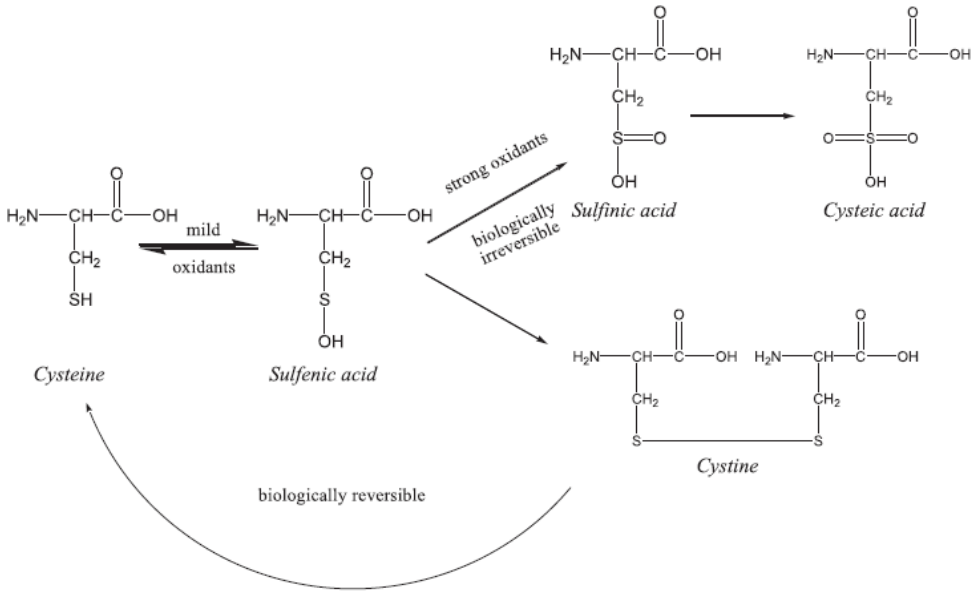

Figure 1.8. Schematic representation of Cys oxidation to produce CYC and cysteic acid. Figure is adopted from [89]

The oxidation of these amino acids is a diffusion-controlled pH-dependent process, all steps being irreversible, and happens in a complex cascade mechanism of electron and proton transfer. The amino acid *Cys* undergoes three consecutive oxidation reactions. In the first step, the sulfhydryl group of *Cys* is oxidized and forms a radical. This radical undergoes nucleophilic attack by water to give an intermediate which is oxidized in the second step to cysteic acid. Oxidation of the sulfhydryl group of *Cys* can also make a disulfide bridge between two *Cys*, leading to form *CYC* [89].

In addition, Purdie et al. claimed that the reaction of active radicals, such as OH°, H_2O_2, etc., with *Cys* appears to undergo some consecutive reactions (i.e. reactions1.1 to 1.8)

$$\boldsymbol{CyssCy + OH^{\circ} \rightarrow CysOH + Cys^{\circ}} \qquad \textbf{1.1}$$

Sulfenic acid and the unstable *Cys* radical are produced in this reaction.

$$\boldsymbol{CysOH + O_2^- \rightarrow CysO_3^- + H} \qquad \textbf{1.2}$$

$$\boldsymbol{CysOH + CySOH \rightarrow CysO_2H + CySH} \qquad \textbf{1.3}$$

$$\boldsymbol{CysOH + H_2O_2 \rightarrow CysO_2H + H_2O} \qquad \textbf{1.4}$$

Moreover, as a result of the combination of *Cys* radical with another *Cys* radical or oxygen, $CysO_2$ can be generated. Radicals of this type have been reported to be stable at room temperature.

Thus it is reasonable to assume that $CysO_2$ is sufficiently stable in aqueous solution to participate in secondary reactions.

$$\boldsymbol{CysO_2 + Cys \rightarrow CysO_2sCy} \qquad \textbf{1.5}$$

$$\boldsymbol{CysO_2 + CySO_2 \rightarrow CysO_2sO_2Cy} \qquad \textbf{1.6}$$

$$\boldsymbol{CysO_2sO_2Cy + H_2O \rightarrow CysO_2H + CysO_3H} \qquad \textbf{1.7}$$

The S, S-dioxide produced in reaction 1.5 has been detected in acidic solutions but is unstable at *pH=5* and decomposes as follows:

$$\boldsymbol{CysO_2sCy + H_2O \rightarrow CysO_2H + CysOH} \qquad \textbf{1.8}$$

As indicated in reactions 1.1 to 1.8, the main oxidation products, $CysO_2H$ (L-Alaninesulfinic acid) and $CysO_3H$ (L-cysteic acid), can be formed from the same intermediates by different reactions in acidic pH [87].

1.6 Aim of this study

Based on the considerations mentioned above, in this thesis, the structure of xCT, the light subunit of the xC^- antiporter is investigated. By using homology modeling and two different states of AdiC [90] and one state of GLU/GABA (GadC) [91] transporters, the xCT subunit of the xC^- antiporter is modeled.

In Chapter 3:, by applying several different simulation techniques, the transport of *CYC* through xCT subunit of the xC^- antiporter, which is responsible for the *CYC* and *Glu* translocation, is investigated. Specifically, the permeation of *CYC* across three model systems, i.e., outward facing (OF), occluded (OCC) and inward facing (IF) configurations of xCT is studied. In addition, in order to qualitatively compare the computational results with experimental observations and thus, to validate these simulations, the effect of mutation of Cys_{327} to *Ala* within xCT, which was also studied experimentally in literature, is investigated.

Hence, these simulations provide a molecular level mechanism of the transport of *CYC* across the xC^- antiporter, more specifically, which amino acid residues in the xC^- antiporter play a key role in the uptake, transport and release of *CYC*.

In Chapter 4:, I will try to provide another possible explanation towards the selective anti-cancer capacity of plasma, based on the transmembrane protein xC^- antiporter. I investigated the effect of Cys_{327} oxidation to cysteic acid on the transport of *CYC* across native and oxidized xCT, by applying US simulations. For this purpose, I used the OF conformation of the xCT subunit.

Finally, I investigated whether, if CAP oxidizes membrane lipids, this lipid peroxidation will affect the xCT subunit conformation or not.

Chapter 2: Computational methodology

2.1 Introduction

In recent years, computer simulations play an essential role in research. Computer simulation methods are important in research because of their ability to make connection between theory and experiment. One of the important advantages of computer simulations is that process parameter interdependencies can be resolved, which might be difficult or impossible to do in a real experiment. Moreover, computer simulations provide solutions to problems and answer questions that often cannot be satisfactory explained by theory and experiment alone. In addition, they can simulate the experimental conditions, and the obtained results can be compared directly with experimental observations. Computer simulations are an extremely powerful tool to understand phenomena underlying experimental observations, study regions that are not accessible experimentally and predict functional effects that are a result of system manipulations before experimental investigation.

Finally, computer simulations are very practical in research as they are a cheap, accessible and also safe method, especially in biological research.

2.2 Computer simulation methods

Using powerful and fast computers makes it possible to investigate complex biological systems at the atomic scale. Monte-Carlo (MC) and Molecular Dynamics (MD) simulations are two main families of simulation techniques. The characteristics of the phenomena under investigation determine which techniques are more useful.

In this work I focused on MD simulation techniques which are more suitable for my study. The first proper MD simulation was reported by Alder and Wainwright in 1956, see [92], who studied the dynamics of an assembly of hard spheres. MD simulation are not based on random numbers (in contrast to MC simulation). The basis of MD simulations is the integration of the equations of motion of the particles. Many wide range of problems, including physics, chemistry, material science, biology (e.g., dynamics of large biomolecules, protein folding, molecular structures, structure of membranes), and so on [93] can be investigated by MD simulation techniques. The advantages and disadvantages of MD simulation methods related to other simulation techniques are illustrated in Table 2.1.

Table 2.1 Advantages and disadvantages of the MD simulation method

Advantages	Disadvantages
The transport properties can be determined, whereas the MC method lacks an objective definition of time.	The description of the electronic (quantum) or excited states is difficult.
The dynamical properties of the system can be investigated	The accuracy of chemical reactions as simulated by classical MD is lower than by DFT or quantum-chemical methods
In classical MD simulation, different time scales are available (in the order of nanoseconds or microsecond).	Classical MD simulation relies on empirical force fields without accounting for electronic properties (change in chemical nature, bond breaking or formation; the latter can be described by reactive MD, but not by non-reactive MD)
In quantum (or ab initio) MD simulations (which were developed by Car and Parinello for the first time [94]), chemical reactions can be described with very high accuracy.	
Classical MD simulation can be performed on systems with composition of several thousand atoms (~10^3-10^6 atoms)	

In biology, MD simulation techniques are strong tools for understanding and studying the dynamics and mechanics of all related steps [95]. They are able to find conformational transitions in large-scale proteins, such as antiporters. Recently, non-equilibrium MD methods, such as steered MD (SMD) [96] (see section 2.4), targeted MD (TMD) [97] (see section 2.5), accelerated MD [98] and metadynamics [99], as well as umbrella sampling (US) [100] (see section 2.6) have been used frequently to investigate the conformational transitions in various transporters [95, 101, 102].

In this study, only classical MD simulations (i.e., TMD, SMD and US simulations) are practical, which can handle the system composed of several thousands of atoms, over time scales of nanoseconds or even microseconds.

2.3 **Molecular Dynamics**

2.3.1 Molecular interaction

In classical MD simulations, the trajectories of all atoms are calculated by integrating the equations of motion. In MD simulations, the Newton's equations of motion (see equation 2.1) is used for time evaluation of the interacting atom in the system.

$$\vec{F}_i = m_i \frac{d^2\vec{r}_i(t)}{dt^2} \qquad \textbf{2.1}$$

In this equation, $\vec{r}_i(t)$ and m_i are the position and mass of atom *i* respectively, and F_i is the interaction force on atom *i* at time *t*. In fact, in MD simulations the forces F_i acting on the atoms are usually derived from a potential energy $U(r^N)$ (see equation 2.2), where $r^N = (\vec{r}_1, \vec{r}_2, \dots, \vec{r}_N)$ shows the complete set of 3N atomic coordinates

$$\vec{F}_i = -\nabla_{r_i} U(r^N) \qquad \textbf{2.2}$$

The total potential energy $U(r^N)$ can be defined experimentally or by means of computer simulations[103-105], and can be described as the sum of a bonded potential (U_{Bonded}) (e.g., harmonic bond potential (U_{Bond}), harmonic angle potential (U_{Ang}) and torsion potential, which is defined from the sum of the dihedral potential (U_{Dih}) and improper dihedral potential (U_{Imp})) and a non-bonded interaction ($U_{Non-bonded}$) (e.g., the electrostatic potential ($U_{Coulomb}$) and Lennard-Jones potential (U_{LJ})).

Harmonic bond potential

To model a covalent bond in a molecular structure, many types of interaction potentials can be considered. The most common potential to be used in any MD program is the harmonic bond potential. The harmonic bond potential is defined between two atoms which have a covalence bond. This potential is given by:

$$U_{Bond} = \frac{1}{2} \sum_{bonds} k_{ij}^{bond} (\vec{r}_{ij} - \vec{r}_{eq})^2 \qquad \textbf{2.3}$$

where k_{ij}^{bond} is the force constant between atoms *i* and *j*, and $\vec{r}_{eq}$ and $\vec{r}_{ij}$ represent the equilibrated bond length and the distance between atoms *i* and *j*, hence the current length of the bond, respectively. Figure 2.1 represents the parameters of the bond potential.

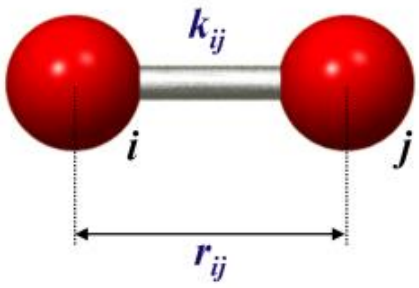

Figure 2.1. Schematic representation of the harmonic bond potential parameters between two atoms i and j. Figure is adopted from [106].

Harmonic Angle potential

Between three atoms bonded to each other, there is one bend angle. As is obvious in Figure 2.2, this angle is indicated by θ_{ijk} and is between three atoms *i*, *j* and *k*. To compute the harmonic angle potential, two vectors must be defined, $\vec{r}_{ij} = \vec{r}_i - \vec{r}_j$ and $\vec{r}_{kj} = \vec{r}_k - \vec{r}_j$, in which $\vec{r}_i$, $\vec{r}_j$ and $\vec{r}_k$ are the position vectors of atoms *i*, *j* and *k*.

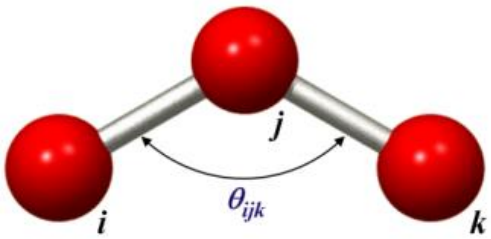

Figure 2.2. Schematic representation of the harmonic angle potential parameters between three atoms i, j and k. Figure is adopted from [106].

By using these two vectors, $cos(\theta_{ijk})$ is expressed by

$$\boldsymbol{cos(\theta_{ijk}) = \frac{\vec{r}_{ij}.\ \vec{r}_{kj}}{|\vec{r}_{ij}||\vec{r}_{kj}|}} \qquad \textbf{2.4}$$

Finally, the harmonic angle potential is defined by equation 2.5.

$$\boldsymbol{U_{Ang} = \frac{1}{2}\sum_{Angles} k^{\theta}_{ijk}\,(\theta_{ijk} - \theta_{eq})^2} \qquad \textbf{2.5}$$

where θ_{eq} is the equilibrated angle and k^{θ}_{ijk} is the force constant for the harmonic version of the angle potential.

Torsion potentials

Among all torsion potentials, the dihedral and improper dihedral potential are the most common ones. These two potentials rely on a quartet of atoms.

Figure 2.3 schematically illustrates the dihedral and improper dihedral torsional angle parameters. A dihedral potential relies on four consecutive bonded atoms (Figure 2.3 (A)), while the improper dihedral potential is relevant to three atoms that are bonded to a common atom (Figure 2.3 (B)).

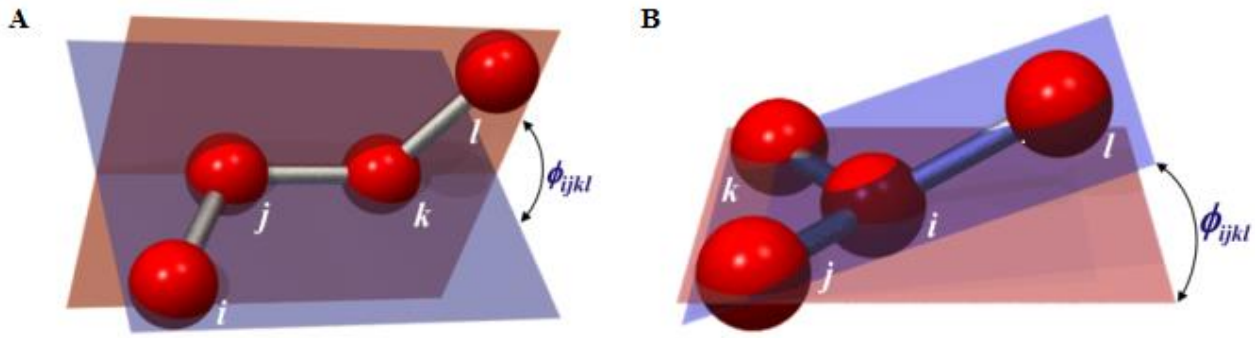

Figure 2.3. Schematic illustration of torsional angle parameters for the dihedral potential (A) and for the improper dihedral potential (B). Figures are adopted from [106].

Dihedral potential

It is clear that in a dihedral potential (see below, Equation 2.9), the torsion angle ϕ_{ijkl} is the angle between two planes going through atoms *i*, *j* and *k*, and atoms *j*, *k* and *l* (see Figure 2.3 (A)). To compute the torsion angle ϕ_{ijkl}, both normal vectors of the two mentioned planes are determined, using four vectors $\vec{r}_{ij} = \vec{r}_i - \vec{r}_j$, $\vec{r}_{kj} = \vec{r}_k - \vec{r}_j$, $\vec{r}_{jk} = \vec{r}_j - \vec{r}_k$ and $\vec{r}_{lk} = \vec{r}_l - \vec{r}_k$ (see below).

$$\vec{m} = \vec{r}_{ij} \times \vec{r}_{kj} \qquad \textbf{2.6}$$

$$\vec{n} = \vec{r}_{jk} \times \vec{r}_{lk} \qquad \textbf{2.7}$$

The cosine of the torsion angle can be determined from equation 2.8.

$$cos(\phi_{ijkl}) = \frac{\vec{m}.\vec{n}}{|\vec{m}||\vec{n}|} \qquad \textbf{2.8}$$

And finally the dihedral potential is expressed by:

$$U_{Dih} = \sum_{Dih} \sum_{n_{ijkl}} k_{ijkl}^{\phi,n} \left(1 + cos\left(n_{ijkl}\phi_{ijkl} - \phi_{eq}\right)\right) \qquad \textbf{2.9}$$

In this equation, $k_{ijkl}^{\phi,n}$ is the force constant related to the cosine type of

potential, ϕ_{eq} is the dihedral angle of these four consecutive atoms at minimum value of their dihedral potential, and n_{ijkl} is the multiplicity, which is a nonzero and positive integer number, indicating the number of minima as the bond is rotated through 360°.

Improper dihedral potential

Like the dihedral torsion angle, the improper torsion angle ϕ_{ijkl} is the angle between two planes going across atoms *i*, *j* and *k* and atoms *j*, *k* and *l* (see Figure 2.3 (B)). The labels of these four atoms in Figure 2.3 (B) have been chosen in the way that all calculations are the same as before (see Equation 2.6-2.8). The improper dihedral potential is expressed by:

$$\boldsymbol{U_{Imp} = \frac{1}{2}\sum_{Imp} k^{\phi}_{ijkl}\,(\phi_{ijkl} - \phi_{eq})^2} \qquad \textbf{2.10}$$

Electrostatic and Lennard-Jones potential

The electrostatic interaction between two atoms *i* and *j*, in the same or a different molecule, is expressed by using Coulomb's law:

$$\boldsymbol{U_{Coulomb} = \frac{q_i q_j}{4\pi\varepsilon_0 r_{ij}}} \qquad \textbf{2.11}$$

where q_i and q_j are the charges of the interacting atoms *i* and *j*, respectively, $r_{ij} = \left|\vec{r}_i - \vec{r}_j\right|$ (see Figure 2.4 (A)) is the distance between them and ε_0 is the permittivity of vacuum.

The van der Waals interaction is a combination of several attractive forces between two atoms, which are not bonded to each other, i.e., dipole-dipole interaction, dipole – induced dipole interaction, and induced dipole – induced dipole interaction. In addition, such atoms also experience repulsive interactions. The Lennard-Jones potential is the most common model to describe the combination of attractive and repulsive forces between non-bonded atoms. It depends only on two parameters and is defined as:

$$\boldsymbol{U_{LJ} = 4\varepsilon_{ij}\left(\left(\frac{\sigma_{ij}}{r_{ij}}\right)^{12} - \left(\frac{\sigma_{ij}}{r_{ij}}\right)^{6}\right)} \qquad \textbf{2.12}$$

where ε_{ij} is the minimum depth of the potential well for the interaction between atoms *i* and *j*, σ_{ij} is the finite distance at which the inter-particle potential is zero and $r_{ij} = \left|\vec{r}_i - \vec{r}_j\right|$ is the distance between atoms *i* and *j* (see Figure 2.4 (B)).

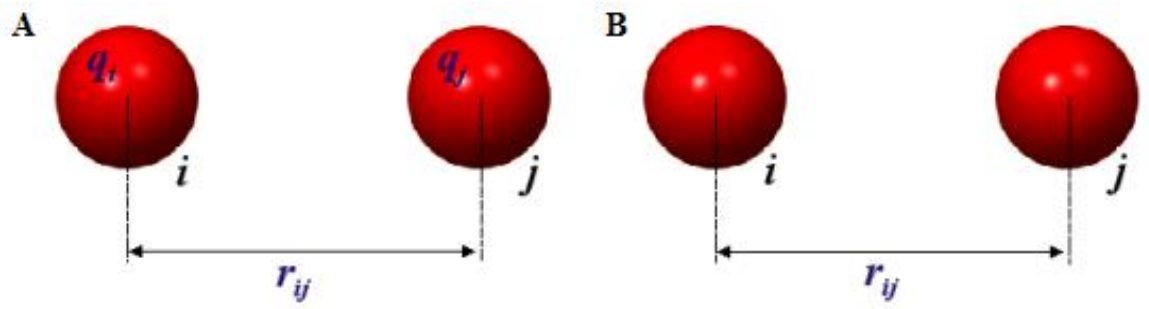

Figure 2.4. Schematic representation of distance and charges of interacting particles i and j for the electrostatic interaction (A) and for the Lennard-Jones potential (B). Figures are adopted from [106].

In Equation 2.12, the part which contains the power 6 is the attractive one, while for the repulsive part, the power 12 is used most often.

Hence, the total potential energy is defined from the sum of all mentioned potentials, and can be described as:

$$\begin{aligned} \boldsymbol{U_{Tot}} &= \boldsymbol{U_{Bonded}} + \boldsymbol{U_{Non-bonded}} \\ &= \left(\boldsymbol{U_{Bond}} + \boldsymbol{U_{Ang}} + \boldsymbol{U_{Dih}} + \boldsymbol{U_{Imp}}\right) + \left(\boldsymbol{U_{Coulomb}} + \boldsymbol{U_{LJ}}\right) \end{aligned} \qquad \textbf{2.13}$$

The equation of motion (2.1) is numerically integrated in MD simulation packages. For determining the position of the atoms after each time step in the system, different integrator algorithms can be used, but the Verlet integrator is the most common one in MD simulations [107]. The integration algorithm of the MD simulation used in this work is described in the next section. The accuracy of the interatomic potentials, also known as force fields, used for complex biosystems, is discussed in section 2.3.3.

2.3.2 Integration algorithms

Among all different algorithms used for solving Newton's equation of motion, the Verlet algorithm is commonly used in MD simulation [107]. This algorithm is one of the simplest and effective ones, and it is stable, accurate and simple. This algorithm is derived from two third–order Taylor expansions for the positions $r(t)$:

$$\vec{\boldsymbol{r}}(\boldsymbol{t}+\Delta\boldsymbol{t}) = \vec{\boldsymbol{r}}(\boldsymbol{t}) + \vec{\boldsymbol{v}}(\boldsymbol{t})\Delta\boldsymbol{t} + \frac{\boldsymbol{1}}{\boldsymbol{2!}}\vec{\boldsymbol{a}}(\boldsymbol{t})\Delta\boldsymbol{t^2} + \frac{\boldsymbol{1}}{\boldsymbol{3!}}\vec{\boldsymbol{b}}(\boldsymbol{t})\Delta\boldsymbol{t^3} + \boldsymbol{O}(\Delta\boldsymbol{t^4}) \qquad \textbf{2.14 a}$$

$$\vec{\boldsymbol{r}}(\boldsymbol{t}-\Delta\boldsymbol{t}) = \vec{\boldsymbol{r}}(\boldsymbol{t}) - \vec{\boldsymbol{v}}(\boldsymbol{t})\Delta\boldsymbol{t} + \frac{\boldsymbol{1}}{\boldsymbol{2!}}\vec{\boldsymbol{a}}(\boldsymbol{t})\Delta\boldsymbol{t^2} - \frac{\boldsymbol{1}}{\boldsymbol{3!}}\vec{\boldsymbol{b}}(\boldsymbol{t})\Delta\boldsymbol{t^3} + \boldsymbol{O}(\Delta\boldsymbol{t^4}) \qquad \textbf{2.14 b}$$

These two equations reveal the forward (Equation 2.14 a) and backward

(Equation 2.14 b) motion in time. In both equations, $\vec{v}(t)$ and $\vec{a}(t)$ represent the velocity and acceleration, respectively, and $\vec{b}(t)$ is the third derivative of $\vec{r}(t)$ related to time. By adding two expansions, the main integrator formula is obtained as follows:

$$\vec{r}(t+\Delta t) = 2\vec{r}(t) - \vec{r}(t-\Delta t) + \vec{a}(t)\Delta t^2 + O(\Delta t^4) \qquad \textbf{2.15}$$

This equation is the basic form of the Verlet algorithm, where Δt is the time-step and $O(\Delta t^4)$ is the truncated error, which can be negligible by applying a small Δt. In this equation $a(t)$ is the force divided by the mass, and is derived from:

$$\vec{a}(t) = \frac{1}{m}\vec{F}(t) = -(\frac{1}{m})\nabla V(\vec{r}(t)) \qquad \textbf{2.16}$$

Here $V(\vec{r}(t))$ denotes the potential energy. The velocity $v(t)$ is needed to compute the kinetic energy K, which is necessary to evaluate the conservation of the total energy ($E = K + V$), but in the Verlet algorithm, it is not directly produced. Hence, the velocities are computed from the positions, by using:

$$\vec{v}(t) = \frac{\vec{r}(t+\Delta t) - \vec{r}(t-\Delta t)}{2\Delta t} \qquad \textbf{2.17}$$

By inserting equations 2.14 a and b into the equation 2.17, and using equation 2.16, the $\vec{v}(t+\Delta t)$ in terms of $\vec{v}(t)$ can be obtained (Equation 2.18).

$$\vec{v}(t+\Delta t) = \vec{v}(t) + \frac{1}{m}\vec{F}(t)\Delta t + O(\Delta t^3) \qquad \textbf{2.18}$$

and the total kinetic energy of the N-particle system is obtained from:

$$K = \frac{1}{2}\sum_{1}^{N} m_i \vec{v}_i \otimes \vec{v}_i \qquad \textbf{2.19}$$

Finally, the positions, velocities and accelerations at time $t + \Delta t$, in the Verlet algorithm, are developed in order to increase the accuracy and keeping the long energy conservation. These quantities are computed in the following way:

$$\vec{r}(t+\Delta t) = \vec{r}(t) + \vec{v}(t)\Delta t + \frac{d^2\vec{r}(t)}{2dt^2} \quad \textbf{2.20}$$

$$\vec{v}(t+\Delta t) = \vec{v}\left(t+\frac{\Delta t}{2}\right) + \vec{a}(t+\Delta t)\Delta t \quad \textbf{2.21}$$

2.3.3 Force fields in MD simulations

Various MD force fields have been developed in order to study biological systems. Three main categories of force fields, i.e., all-atom, united-atom and coarse-grained, can be applied for MD simulations. In the all-atom force fields, such as Amber [108], Charmm [109] and OPLS [110], each atom in the system is included separately. All-atom force fields are more accurate than united-atom and coarse-grained force fields, but they are more time consuming. United-atom and coarse-grained force fields can handle a larger system for the same time scales as all-atom simulations but with lower accuracy. In the united-atom force fields, such as GROMOS [111] , all heavy atoms are included separately, but the carbon atoms and aliphatic hydrogen atoms bonded to these carbon atoms are treated as one group. In this method, by reducing the number of separate particles, larger systems can easily be simulated. In the coarse-grained force fields, such as Martini [112] and Cooke [113], 3-5 heavy atoms with their H atoms are combined as one functional group. Further decreasing the number of particles in the system leads to studying larger systems with high calculation speed.

In this PhD thesis, I applied the Charmm force field (all-atom), to study the translocation of CYC from xC^- antiporter (see Chapter 3: and 4). The parameters of the force field were obtained from [114-117]. Moreover, in order to study the effect of lipid oxidation on xCT conformation, the GROMOS force field was applied.

2.3.4 Periodic boundary conditions (PBCs)

When a small part of a large biological system is simulated, PBCs need to be used. In MD simulations, a combination of 10^2-10^7 atoms is investigated, while the whole system is composed of ~10^{23} atoms (corresponding to 1 mole). Using PBCs make it possible to compute the macroscopic parameters, avoiding the edge effects in MD simulations. By using PBCs, a small finite box is defined, including all atoms under investigation. This computational box is surrounded by replica boxes with identical content. When the atoms leave the main box, they enter the box with the same velocity as before, from the opposite side of the box. Figure 2.5 clearly shows how atoms leave and enter the simulation box. Each atom can

interact with other atoms in the box or with images of them, entering the box from the other side. This condition has no effects on the forces or the behavior of the system and makes an infinite space for system treatment.

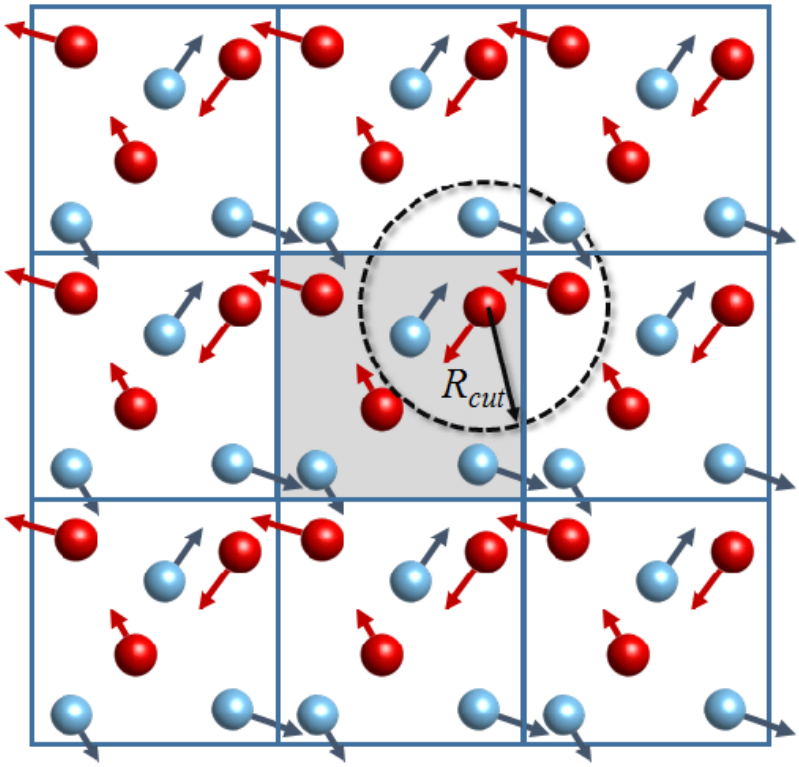

Figure 2.5. Schematic representation of PBCs applied to a principal box with gray color. The velocity of each atom is illustrated by a small vector. Atoms leaving the principal box enter by their image from the opposite side of the box. R_{cut} is the cutoff distance for the interaction potential (short range interaction). Figure is adopted from [118]

In the computational box, if the position of atom i is r_i, the position of the mirror image of this atom can be defined from:

$$\vec{r}_i^{image} = \vec{r}_i + l\vec{a} + m\vec{b} + n\vec{c} \qquad \textbf{2.22}$$

where $\vec{a}$, $\vec{b}$ and $\vec{c}$ are box vectors and l, m and n are integer numbers from $-\infty$ to $+\infty$. Although most simulations are done in a triclinic (cubic) box, there are six different types of boxes, which can fill the simulation space. Figure 2.6 illustrates the types of simulation boxes, namely the triclinic box, the hexagonal prism, the rhombic dodecahedron, the elongated rhombic dodecahedron, the truncated and general truncated octahedron [119].

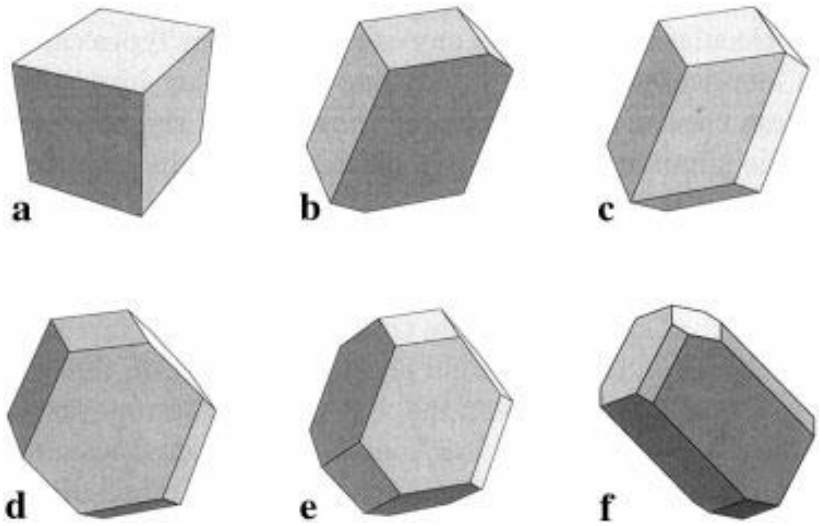

Figure 2.6. Six different types of boxes that can fill the simulation space with PBCs: (a) the triclinic box, (b) the hexagonal prism, (c) the rhombic dodecahedron, (d) the elongated rhombic dodecahedron, (e) the truncated octahedron and (f) general truncated octahedron. Figure is adopted from [119].

When defining the box for MD simulations with PBCs, some limitations should be considered:

The size of the simulation box should be larger than $2R_{cut}$, where $R_{cut}$is the cutoff distance for the interaction potential (see Figure 2.5). To avoid the interaction of each atom with its own image or to guarantee the interaction of any atom i with only one image of the atom j, it is important to define a large enough box (i.e., larger than $2R_{cut}$). Note that for macromolecular simulations, to avoid the interaction of each atom of a macromolecule with its own image or multiple images, this limitation for the cutoff is not enough and each box vector should be larger than the maximum size of the macromolecule plus $2R_{cut}$ distance [120].

In this study, I used PBCs with a cubic (i.e., triclinic) box. The system under investigation in this study (i.e., the xC^- antiporter located into the membrane) is a small part of a much larger system (i.e., the cell membrane).

2.3.5 Thermodynamic ensembles

In MD simulations, using a suitable ensemble is very important. In statistical physics, an ensemble is defined as a large number of microstates of the system having the same thermodynamic quantities in a macroscopic scale. These macroscopic quantities are obtained by averaging over all microstates of the system. Preparation of a large number of systems with different microstates is not possible in MD simulation. Therefore, if we have long enough simulation time, all possible microstates of the system can take place. In these kinds of systems,

which are called ergodic systems, time averaging and ensemble averaging lead to the same thermodynamic quantities in macroscopic scale.

There are four applicable ensembles in MD simulations: microcanonical ensemble (NVE) [121], canonical ensemble (NVT) [122], isobaric-isothermal ensemble (NPT) [123] and grand canonical ensemble (μVT) [124, 125].

The microcanonical ensemble refers to the system in which the number of particles in the simulation box (N), the volume (V) and the total energy (E) are kept constant. This system is not able to control the pressure (P) and the temperature (T) of the system, which are important when investigating biological processes. In the canonical ensemble, the thermodynamic system is kept in the condition with a constant number of particles (N), volume of simulation box (V) and temperature (T). In the isobaric-isothermal ensemble, in addition to particle and temperature conservation (N and T), by changing the box size, the pressure (P) is kept constant. This ensemble is one of the important and realistic ensembles for investigating biological functions using MD simulations. The result of MD simulations by using the isobaric-isothermal ensemble can be easily compared with experimental data. Finally, in the grand canonical ensemble, the system can exchange energy and particles in a simulation box in a way that the chemical potential (μ) is kept constant. In this ensemble, three thermodynamic quantities, i.e., chemical potential (μ), volume of simulation box (V) and temperature, are kept constant.

In this work, the canonical (NVT) and isobaric-isothermal (NPT) ensembles are applied, using a suitable thermostat and barostat to control the temperature and pressure, respectively (see next section).

2.3.6 Thermostat and barostat

To control the temperature and pressure of the system, various algorithms exist. The Andersen thermostat [123] based on a stochastic coupling method, the Nose-Hoover [122, 126] and the weak-coupling scheme of the Berendsen thermostat [127] are some examples of these algorithms in order to keep the temperature constant. Details of thermostat algorithms are given in [125].

Andersen thermostat

The algorithm of the Andersen thermostat is based on random collision of particles with an imaginary heat bath, having the desire temperature. This

thermostat doesn't keep energy of the system constant, so it is useful to initially stabilize the temperature in the microcanonical ensemble and simulate the system in the canonical ensemble. For the given temperature, the velocities of random particles are reallocated according to Maxwell-Boltzmann distribution, at every integration time step. Eventually, the random particles are chosen according to the Poisson distribution. The Maxwell-Boltzmann distribution for a single particle at the desired temperature is given by:

$$f(\vec{v}_i) = 4\pi v \left(\frac{m_i}{2\pi k_B T}\right)^{\frac{3}{2}} exp(-\frac{m_i \vec{v}^2}{2k_B T}) \qquad \textbf{2.23}$$

In this thermostat, the collision frequency or collision time is adapted frequently and the collision time is chosen based on the time scale of molecular motions. Therefore, in this method, long time MD simulations are needed to have enough heat bath collisions. Although the Andersen thermostat is an accurate method to generate the canonical ensemble probabilities, the calculation of certain parameters, as a result of not keeping true molecular kinetics, leads to incorrect values.

Berendsen thermostat

To preserve the temperature of the system, which is connected to a heat bath with temperature T_0, the velocities of particles should be rescaled at each time step. In this method, the rate of temperature variation is given by:

$$\frac{dT(t)}{dt} = \frac{1}{\tau}(T_0 - T(t)) \qquad \textbf{2.24}$$

where τ determines the tight coupling between the heat bath and the system. Generally, an exponential decay of temperature of the system toward the intended temperature is given by this method. The temperature difference between consecutive time steps is obtained from:

$$\Delta T = \frac{\delta t}{\tau}(T_0 - T(t)) \qquad \textbf{2.25}$$

The scaling factor for velocities is defined from:

$$\lambda^2 = 1 + \frac{\delta t}{\tau}\left\{\frac{T_0}{T(t)} - 1\right\} \qquad \textbf{2.26}$$

The updated velocities $\vec{v}_i'$ are determined from $\vec{v}_i' = \lambda\vec{v}_i$. In the Berendsen thermostat, the velocities of the atoms are rescaled in every step to converge to the target temperature, while still allowing for temperature fluctuations. This thermostat does not capture proper energy fluctuations and is suitable for my MD simulations at NVT ensemble, when no barostat is applied to control the pressure.

Nose-Hoover thermostat

The high accuracy of the Nose-Hoover method gives it the highest performance in MD simulations at constant temperature. In comparison with the Berendsen thermostat, which is very efficient for relaxing a system to the desired temperature, the Nose-Hoover method is very accurate to probe a correct canonical ensemble [128].

The Nose-Hoover algorithm was introduced by Nose and subsequently modified by Hoover. In this thermostat, the heat bath as an integral part of the system contains imaginary particles with the friction coefficient ξ and extra degree of freedom *s*. The Hamiltonian for this system is defined from:

$$\mathcal{H} = \frac{1}{2}\sum \boldsymbol{m}|\vec{\boldsymbol{p}}_{\boldsymbol{i}}| + \boldsymbol{U}(\vec{\boldsymbol{r}}_{\boldsymbol{N}}) + \frac{\boldsymbol{\xi}^{\boldsymbol{2}}\boldsymbol{Q}}{\boldsymbol{2}} + \boldsymbol{3Nk_BTlns} \qquad \textbf{2.27}$$

Here Q is an imaginary mass which determines the coupling between the reservoir and the real system. Also, $\vec{r}$ and $\vec{p}$ represent the coordinate and momentum, respectively. The time evolution of particle positions and momentum is followed from:

$$\frac{d\vec{\boldsymbol{r}}_{\boldsymbol{i}}}{\boldsymbol{dt}} = \vec{\boldsymbol{v}}_{\boldsymbol{i}} \qquad \textbf{2.28 a}$$

$$\frac{d\vec{\boldsymbol{v}}_{\boldsymbol{i}}}{\boldsymbol{dt}} = -\frac{\boldsymbol{1}}{\boldsymbol{m_i}}\frac{\boldsymbol{\partial U}(\vec{\boldsymbol{r}}_{\boldsymbol{N}})}{\boldsymbol{\partial}\vec{\boldsymbol{r}}_{\boldsymbol{i}}} - \boldsymbol{\xi}\vec{\boldsymbol{v}}_{\boldsymbol{i}} \qquad \textbf{2.28 b}$$

$$\frac{d\boldsymbol{\xi}}{\boldsymbol{dt}} = \frac{\sum \boldsymbol{m}|\vec{\boldsymbol{v}}_{\boldsymbol{i}}|^{\boldsymbol{2}} - \boldsymbol{3Nk_BT}}{\boldsymbol{Q}} \qquad \textbf{2.28 c}$$

$$\frac{\boldsymbol{dlns}}{\boldsymbol{dt}} = \boldsymbol{\xi} \qquad \textbf{2.28 d}$$

Due to the accuracy of the Nose-Hoover thermostat, it is used frequently in MD simulations. Particularly, in this study, the Nose-Hoover thermostat is applied for all MD simulations at the NPT ensemble, using GROMACS software.

Langevin thermostat

By considering the large particles motion through a continuum of smaller particles, the Langevin equation is taken into account [129]. In many solute-solvent systems, the solvent affects the dynamics of the solute by random collisions. In fact, the smaller particles (e.g. solvent) move with kinetic energy and randomly "kick" the large particles and create a damping force. This imposing frictional drag force influences the motion of large particles. Accordingly, in Langevin dynamics the temperature is kept constant by modifying the Newton's equation of motion as follows:

$$\frac{d\vec{r}_i}{dt} = \frac{\vec{p}_i}{m_i}; \qquad \frac{d\vec{p}_i}{dt} = \vec{F}_i - \gamma_i \vec{p}_i + \vec{f}_i \tag{2.29}$$

where $\vec{F}_i$ is the interaction force on atom *i*, due to the interaction potential ($\vec{F}_i = -\frac{\partial U(\vec{r})}{\partial \vec{r}_i}$), $\vec{f}_i$ is a random force with dispersion σ and γ_i is a friction coefficient that is related to σ by a fluctuation-dissipation relation, recovering the canonical ensemble distribution. The relation between σ and γ_i is represented by:

$$\sigma^2 = 2m_i\gamma_i k_B T \tag{2.30}$$

In MD simulation, at each time step Δt the Langevin thermostat changes the momenta via:

$$\Delta\vec{p}_i = (\vec{F}_i - \gamma_i \vec{p}_i + \delta p)\Delta t \tag{2.31}$$

Here $-\gamma_i \vec{p}_i$ is a damping force and δp represents the random fluctuation force by the thermal kicks of the small particles. The probability of δp is obtained by a Gaussian distribution via:

$$\rho(\delta p) = \frac{1}{\sqrt{2\pi\sigma}} exp\left(-\frac{|\delta p|^2}{2\sigma^2}\right) \tag{2.32}$$

By combination of the damping factor and the random force, the correct

canonical ensemble is given. As a result of elimination of many atoms and including them implicitly by a stochastic term, fewer computations are needed to have the desired temperature. Moreover, the damping term has an important role to stabilize the equation of motion in a relatively large time step of Δt.

Eventually, in this study, the Langevin thermostat is applied for all MD simulations using NAMD software.

Berendsen barostat

In addition to keeping the temperature constant by applying a suitable thermostat, the system needs to be coupled to a pressure bath for pressure conservation. A number of algorithms have been developed in order to keep the pressure constant. One of these algorithms is the Berendsen barostat [127]. This method is based on the weak coupling of the system and an external bath with pressure P_0, using the principle of minimum perturbation. In this algorithm the volume is rescaled by a factor λ to keep the pressure at constant value. This factor is represented by:

$$\boldsymbol{\lambda = 1 - \kappa \frac{\Delta t}{\tau_p}(P(t) - P_0)} \qquad \textbf{2.33}$$

Here κ is the isothermal compressibility, τ_p is a time constant for the coupling. The volume dependency of κ is represented by:

$$\boldsymbol{\kappa = \frac{1}{k_B T}\frac{\langle V^2\rangle - \langle V\rangle^2}{\langle V\rangle^2}} \qquad \textbf{2.34}$$

The position of each atom is renewed by $\vec{r}_i' = \lambda^{1/3}\vec{r}_i$ and pressure is obtained as follows:

$$\boldsymbol{P(t) = \frac{1}{V(t)}\left(Nk_B T(t) + \frac{1}{D}\langle \sum_{i=1}^{N} \overrightarrow{r_i}(t).\overrightarrow{F_i}(t)\rangle\right)} \qquad \textbf{2.35}$$

In this equation, D represents the dimensionality of the system.

Parrinello-Rahman barostat

Among all algorithms, the Parrinello-Rahman method is the best pressure coupling method for anisotropic systems. Parrinello and Rahman developed this method by extending the method represented by Andersen. This method is based on the change of the simulation box shape. The mentioned thermostats except Andersen can easily be combined with Parrinello-Rahman coupling in MD simulations.

In this method an arbitrary simulation box can easily be described by three vectors $\vec{a}$, $\vec{b}$ and $\vec{c}$ with different length and mutual orientations. By describing a 3×3 matrix $\boldsymbol{h}$ whose columns are the $\vec{a}$, $\vec{b}$ and $\vec{c}$ vectors, the volume is given by:

$$\boldsymbol{V = det\, h = \vec{a}.(\vec{b} \times \vec{c})} \qquad \textbf{2.36}$$

The position of each particle $\vec{r}_i$ can be written in terms of $\boldsymbol{h}$ and a column vector $\vec{s}_i$ as follows:

$$\boldsymbol{\vec{r}_i = h\vec{s}_i = \xi_i \vec{a} + \eta_i \vec{b} + \zeta_i \vec{a}} \qquad \textbf{2.37}$$

with $0 \leq \xi_i, \eta_i, \zeta_i \leq 1$. The distance between atoms *i* and *j* is obtained by:

$$\boldsymbol{r_{ij}^2 = (\vec{s}_i - \vec{s}_j)^T G\, (\vec{s}_i - \vec{s}_j)} \qquad \textbf{2.38}$$

Here $\boldsymbol{G}$ is a metric tensor and given by:

$$\boldsymbol{G = h^T h} \qquad \textbf{2.39}$$

In the simulation box containing the N particles, 3N dynamical variables describe the positions of all particles and by adding nine components of $\boldsymbol{h}$, there are 3N + 9 variables. The time evolution of the 3N+9 variables is obtained from Lagrangian as follows:

$$\boldsymbol{\mathcal{L} = \frac{1}{2}\sum_{i=1}^{N} m_i \dot{s}_i^T G\, \dot{s}_i - \sum_{i=1}^{N}\sum_{j>i}^{N} U(\vec{r}_{ij}) + \frac{1}{2} MTr(\dot{h}^T \dot{h}) - PV} \qquad \textbf{2.40}$$

where $\boldsymbol{P}$ is the hydrostatic pressure imposed to the system and $\boldsymbol{M}$ is the matrix parameters that define the strength of the coupling (with dimension of mass). Using equation 2.40 the equation of motion is given by:

$$\boldsymbol{\ddot{h} = VM^{-1}(h^T)^{-1}(P - P_{ref})} \qquad \textbf{2.41}$$

Here $\boldsymbol{V}$ is the volume of the box and $\boldsymbol{P}$ is the current pressure matrix. The corresponding Hamiltonian from Lagrangian equation is given by:

$$\boldsymbol{\mathcal{H} = \frac{1}{2}\sum_{i=1}^{N} \frac{1}{2} m_i \vec{v}_i^2 - \sum_{i=1}^{N}\sum_{j>i}^{N} U(\vec{r}_{ij}) + \frac{1}{2} MTr(\dot{h}^T \dot{h}) + PV} \qquad \textbf{2.42}$$

From the Hamiltonian the equation of motion is obtained as follows:

$$\boldsymbol{\ddot{s}_\iota = -\frac{1}{m_i}\sum_{i \neq j}^{N} \frac{\nabla U(\vec{r}_{ij})}{\vec{r}_{ij}} (\vec{s}_i - \vec{s}_j) - \mathcal{M}\dot{s}_i; \quad \mathcal{M} = G^{-1}\dot{G}} \qquad \textbf{2.43}$$

where $\mathcal{M}$ characterizes the artificial friction and the motion of particles is expressed relative to the vector box. In this study, the Parrinello-Rahman barostat is applied in the NPT ensemble, using GROMACS software.

2.3.7 Steps of MD simulations

In MD simulations a number of steps should be performed to generate and then analyze the final trajectories in order to obtain macroscopic parameters. These are outlined in Figure 2.7.

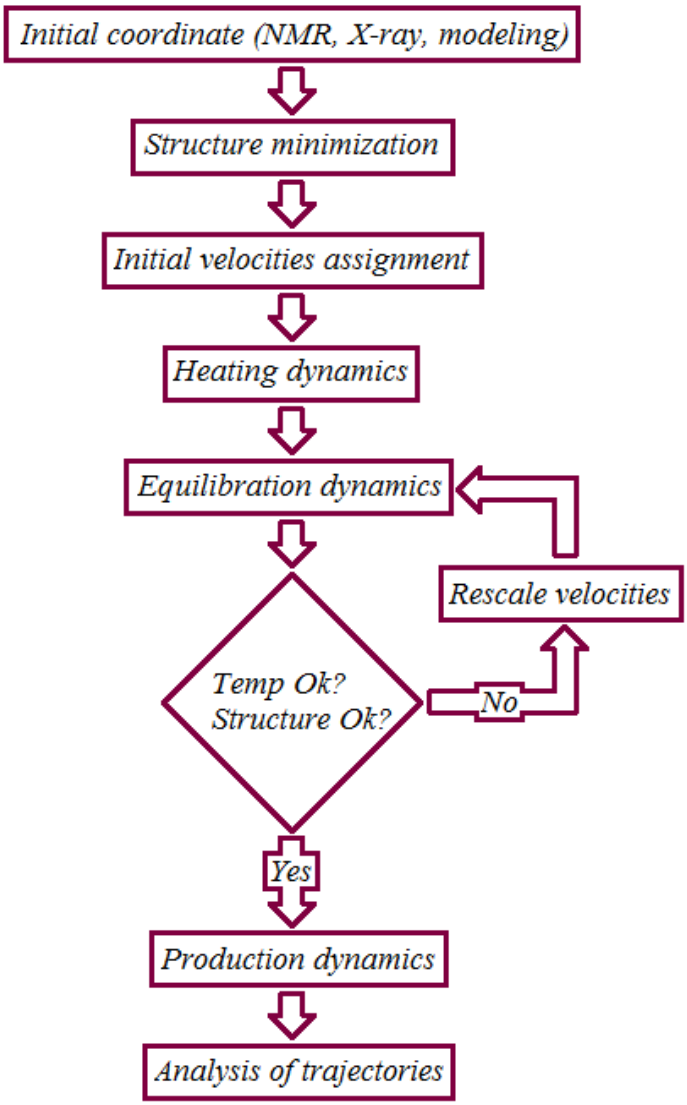

Figure 2.7. Flowchart illustration of the MD simulations steps.

2.4 **Steered MD (SMD)**

In order to predict binding pathways, the mechanism underlying the selectivity of enzymes and to find the ligand position (see Chapter 3:), investigation of the ligand-receptor interactions is very important. Steered MD is applicable for achieving biological information related to non-covalent bonding

and the present time evaluation of binding affinities and potential of mean force [130]. Experimental techniques based on the application of mechanical forces to single molecule, such as atomic force microscopy (AFM) [131, 132], optical tweezers [133-135] and bio membrane force probe techniques [136], have been used to study the properties of protein-ligand binding and their responses to external mechanical manipulations. Steered MD is a similar approach with the mentioned experimental techniques in order to study biomolecules by means of computer simulations.

In this method, by applying a time-dependent external force, the ligand can be dissociated from a protein (see Figure 2.8) or it can be directed towards its binding pocket.

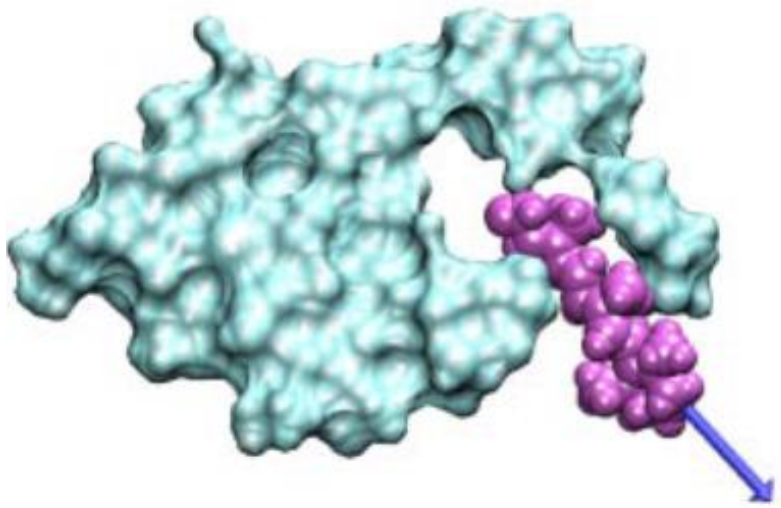

Figure 2.8. Extraction of a ligand (in purple color) from the binding pocket of a protein (in cyan color). The lilac color arrow represents the applied force to the ligand, leading to dissociation of the ligand from the binding pocket of the protein. Figure is adopted from [130].

2.4.1 Constant velocity pulling

In this method, the position of the center of mass of the ligand (SMD atom) is restrained or attached to a point in space (dummy atom) by an external harmonic potential (see Figure 2.9). In fact, the SMD atom is attached to a dummy atom via a virtual spring. As a result of shifting the dummy atom in a given direction $\vec{n}$, the ligand is moved from its initial position. The ligand is allowed to explore new contacts along its movement. By moving the restraint point with a constant velocity $\vec{v}$ and assuming an external potential $U = k\frac{(\vec{v}t-(\vec{r}-\vec{r}_0).\vec{n})^2}{2}$ the external force on the system is expressed by:

$$\vec{F} = -\nabla U = k(\vec{v}t - (\vec{r} - \vec{r}_0)) \qquad \textbf{2.44}$$

Here k is the stiffness of the restraint, $\vec{r}$ and $\vec{r}_0$ are the actual position and initial position of the SMD atom, respectively, and $\vec{n}$ is the direction of pulling. As is clear in Figure 2.9, the dummy atom moves at a constant velocity $\vec{v}$, while the SMD atom experiences the force that depends linearly on the distance between two atoms [137]. NAMD software provides built-in facilities for applying a variety of external forces, including the automated application of moving constraints.

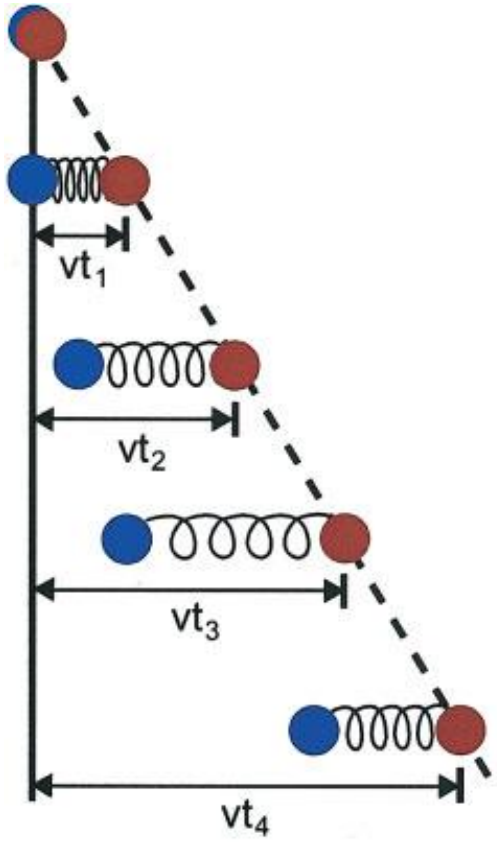

Figure 2.9. Illustration of pulling in a one-dimensional case in an SMD simulation. The SMD atom and dummy atom are colored in blue and red, respectively. Figure is adopted from [137].

In this thesis, to find the binding pocket of xCT, the SMD method was applied to pull the *CYC* into the OF state of the xCT subunit and find the place where the *CYC* was trapped (see Chapter 3:, section 3.3.1 and 3.4.2 for more details).

2.4.2 Constant force pulling

To study the unfolding pathway of proteins or DNA, an SMD simulation with a constant force is a very suitable method. In the case of protein unfolding, the C_α atom of the first residue is kept fixed, and the C_α atom of the last residue, which is called SMD atom, experiences a constant force in the direction defined by the

vector that links both atoms. In this method there is no harmonic potential or dummy atom. The analysis of distance versus time steps can vividly show the structural changes of the protein in each step.

2.5 Targeted MD (TMD)

To study the dynamic behavior of macromolecules, such as conformational changes of antiporters at finite temperature, the TMD method can be employed. This method induces conformational changes to a known structure by applying a time-dependent geometrical constraint [138]. The TMD method simulates the transition of a molecule between two different states. During conformational transition from the initial (*I*) to the target (*F*) structure, each conformation of the molecule is shown by a vector $\vec{\boldsymbol{x}} = (x_1, x_2, \ldots\ x_{3N})^T$, including the 3N coordinates of N atoms. As is clear from Figure 2.10, $\vec{\boldsymbol{x}}_{\boldsymbol{I}}$ and $\vec{\boldsymbol{x}}_{\boldsymbol{F}}$ represent the conformations *I* and *F*, respectively, and the distance $\rho(t)$ is defined as follows:

$$\rho(\boldsymbol{t}) = |\vec{\boldsymbol{x}}(\boldsymbol{t}) - \vec{\boldsymbol{x}}_{\boldsymbol{F}}| = \left(\sum\nolimits_{\boldsymbol{i=1}}^{\boldsymbol{3N}} (\vec{\boldsymbol{x}}_{\boldsymbol{i}}(\boldsymbol{t}) - \vec{\boldsymbol{x}}_{\boldsymbol{Fi}})^{\boldsymbol{2}}\right)^{\frac{\boldsymbol{1}}{\boldsymbol{2}}} \qquad \textbf{2.45}$$

where $\rho(t)$ as a control parameter is used in order to guide the system to go through the desired transition. By defining the constraint via:

$$\phi(\boldsymbol{x}) \equiv |\vec{\boldsymbol{x}}(\boldsymbol{t}) - \vec{\boldsymbol{x}}_{\boldsymbol{F}}|^{\boldsymbol{2}} - \boldsymbol{\rho}(\boldsymbol{t})^{\boldsymbol{2}} = \boldsymbol{0} \qquad \textbf{2.46}$$

and additional force based on:

$$\boldsymbol{F^c} \equiv \boldsymbol{\lambda}\frac{\boldsymbol{d\phi}}{\boldsymbol{dt}} = \boldsymbol{2\lambda}(\vec{\boldsymbol{x}}(\boldsymbol{t}) - \vec{\boldsymbol{x}}_{\boldsymbol{F}}) \qquad \textbf{2.47}$$

the goal of undergoing the system to the given transition is achieved. Here λ is an adjustable Lagrange parameter.

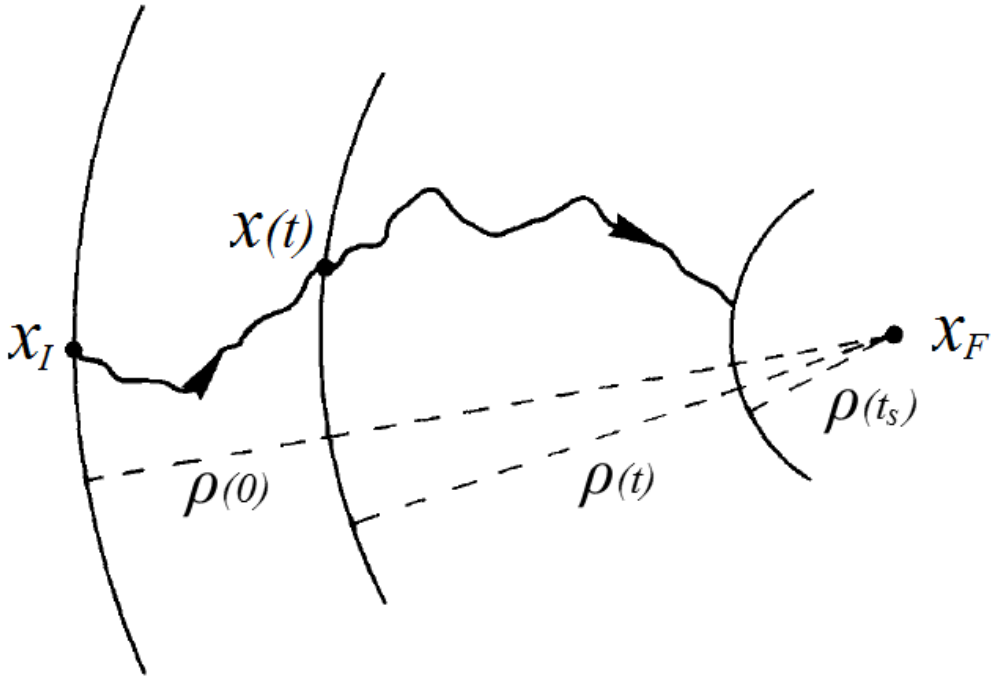

Figure 2.10. Two-dimensional scheme of the conformational transition from the initial (I) to target (F) configurations. Figure is adopted from [139].

The steps of conformational transitions performed by TMD simulations are as follows:

- Distance $\rho(t=0) = \rho(0) = |\vec{\boldsymbol{x}}_I - \vec{\boldsymbol{x}}_F|$ is set.
- Appropriate velocities are chosen.
- The equation of motion with the additional force $F^c$is solved.
- After each time step Δt and obtaining the new position vector $\vec{\boldsymbol{x}}(t+\Delta t)$, ρ is decreased by $\Delta\rho = (\rho(0) - \rho(t_s))\frac{\Delta t}{t_s}$, where t_s is the total simulation time and $\rho(t_s)$ is the final distance for TMD simulation.

The uniform decrease of ρ lets the system to find the pathway from $\vec{\boldsymbol{x}}_I$ to some final conformation having a small distance ρ_f from the target structure $\vec{\boldsymbol{x}}_F$. In each step, the system has maximum freedom to explore different conformations in accordance with the force field, pressure and temperature [138].

In this study, the TMD method was applied for simulating the transition of the xCT subunit of the xC^- antiporter from OF to OCC state, as well as OCC to IF state. Subsequently, TMD simulations were carried out to transport *CYC* across the xCT system (see Chapter 3:, section 3.3.1 for more details).

2.6 **Umbrella sampling (US)**

The important challenge in the field of biophysics and biochemistry is the computation of the binding free energy or dissociation free energy. One of the useful methods that can be applied in this field is the umbrella sampling (US) method [100] which calculates the free energy differences along the reaction coordinate. This powerful technique is developed by considering thermodynamic integration, slow growth, SMD and Jarzynski-based fast grow technique. In the US method by applying an external harmonic bias potential, the system transfers from one thermodynamic state to another one with a given direction and fixed speed along the reaction coordinate (see Figure 2.11). In chemistry, the reaction coordinate is the progress of a reaction from reactants to products with various intermediates and transition states in between. The free energies of transition states cannot be directly measured. These states are transient and cannot be directly observed in experiments. In MD simulations, a reaction coordinate is also called collective variable. During transfer from the initial to final state, a series of intermediate steps (i.e., windows) are formed. In US simulation, along the reaction coordinate (ξ) a number of individual systems is extracted by separating the series of windows, applying a certain distance between the considered molecules. Some geometric parameters, such as the distance between two atoms, dihedral angle, bond length or angle or n/c terminal ends of protein, as well as the distance between membrane and number of reactive species in complicated systems, can be supposed as a reaction coordinate.

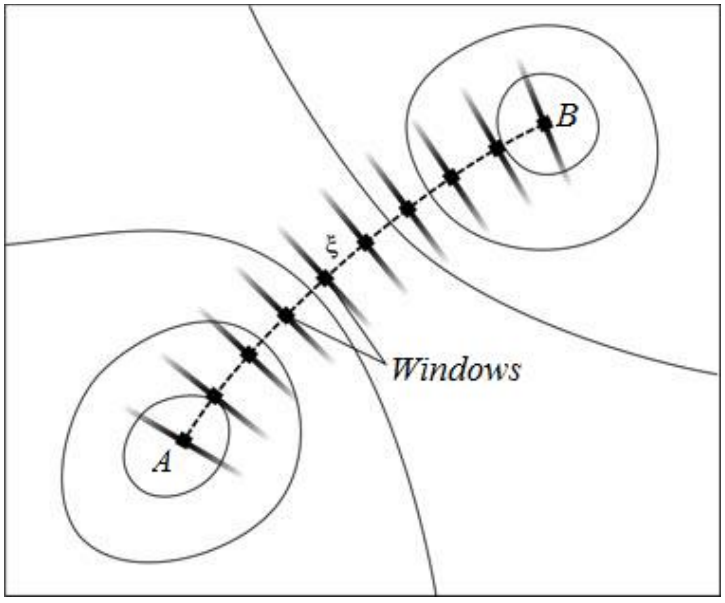

Figure 2.11. Separation of the windows along the reaction coordinate (ξ) between two points A and B during transferring the system between two thermodynamic states. Figure is adopted from [100].

In MD simulations, a reaction coordinate (ξ) can be defined as a continuous parameter that make a distinction between two considered thermodynamic states. The probability distribution of the system along ξ can be computed by integrating over all degrees of freedom as follows:

$$\boldsymbol{Q(\xi) = \frac{\int \delta[\xi(\vec{r}) - \xi] exp\left[-\frac{1}{k_B T} U\right] d^N \vec{r}}{\int exp\left[-\frac{1}{k_B T} U\right] d^N \vec{r}}} \quad \textbf{2.48}$$

Here N is the number of degrees of freedom. Accordingly, the free energy $\boldsymbol{A(\xi)}$, which is also called potential of mean force (PMF), along the reaction coordinate can be defined via:

$$\boldsymbol{A(\xi) = -k_B T ln Q(\xi)} \quad \textbf{2.49}$$

By considering the system as an ergodic system (see section 2.3.5) every point in phase space is visited during the simulation. Therefore, the ensemble average $Q(\xi)$ is equal to the time average $P(\xi)$ for infinite sampling as follows:

$$\boldsymbol{P(\xi) = \lim_{t \to \infty} \frac{1}{t} \int_0^t \rho\,[\xi(t')] dt'} \quad \textbf{2.50}$$

where ρ expresses the occurrence of ξ in a given interval. This interval has infinitesimal width in the exact equation but finite width during histogram calculation. Therefore, by monitoring $P(\xi)$ along the reaction coordinate, $A(\xi)$(i.e. the potential mean force (PMF)) can be directly obtained. By adding a harmonic bias potential w_i to the energy of the system, the potential in US simulation is changed as follows:

$$\boldsymbol{U^b(\vec{r}) = U^u(\vec{r}) + w_i(\xi(\vec{r}))} \quad \textbf{2.51}$$

Here the superscripts ‘u’ and ‘b’ denote unbiased and biased quantities, respectively. The unbiased and biased distributions, which are according to equation 2.48 in order to obtain the unbiased free energy$A_i(\xi)$, can be written as:

$$\boldsymbol{P_i^{u,b}(\xi) = \frac{\int exp\left[-\frac{1}{k_B T} U^{u,b}\right] \delta[\xi'(\vec{r}) - \xi'] d^N \vec{r}}{\int exp\left[-\frac{1}{k_B T} U^{u,b}\right] d^N \vec{r}}} \quad \textbf{2.52}$$

By using equation 2.52, the biased distribution $P_i^b(\xi)$ is substituted into $P_i^u(\xi)$ as follows:

$$P_i^u(\xi) = P_i^b(\xi) exp\left[-\frac{1}{k_B T} w_i(\xi)\right] \times \frac{\int exp\left\{-\frac{1}{k_B T}\left[U(\vec{r}) + w_i(\xi(\vec{r}))\right]\right\} \delta[\xi'(\vec{r}) - \xi'] d^N\vec{r}}{\int exp\left[-\frac{1}{k_B T} U(\vec{r})\right] d^N\vec{r}} = P_i^b(\xi) exp\left[-\frac{1}{k_B T} w_i(\xi)\right] \langle exp\left[-\frac{1}{k_B T} w_i(\xi)\right]\rangle \quad \textbf{2.53}$$

The free energy $A_i(\xi)$ or PMF can be obtained from equation 2.52:

$$A_i(\xi) = -k_B T ln P_i^b(\xi) - w_i(\xi) - k_B T ln \langle exp\left[-\frac{1}{k_B T} w_i(\xi)\right]\rangle \quad \textbf{2.54}$$

In an US simulation, the weighted histogram analysis method (WHAM) [140] is applied to compute the free energy profile (FEP), or potential of mean force (PMF). This method is helpful to estimate the mechanical properties of macromolecules [141, 142] as well as to compute the interaction between protein-protein [143], protein-drug [144], protein-lipid [145], membrane-drug [146] and plasma species-membrane [147].

In this PhD study, US simulations were performed in order to compute the FEPs for transport of *CYC* through the OF, OCC and IF structures of the xCT subunit (see Chapter 3:, section 3.5). Moreover, this method was applied to investigate the effect of a mutation and oxidation of Cys_{327} to Ala_{327} and CYO_{327} in the xCT subunit, respectively, on the permeation of CYC (see more details in Chapter 3:, sections 3.3.2 and 3.5, as well as Chapter 4:, sections 4.2.5 and 4.3.4).

2.7 Conclusion

All the above mentioned calculation methods are able to describe bonded and non-bonded interactions between important atoms, such as H/C/O/N/S/P atoms, which are the basic elements of lipids, amino acids, and nucleic acids. Therefore, I have used MD, SMD, TMD and US simulations in this thesis for specific model systems.

The specific details of these simulations, as well as the results for the various model systems studied in this PhD thesis, will be described in Chapter 3: and 4.

Chapter 3: Investigation of the structure of the xCT subunit[1]

[1] This chapter was published as “M Ghasemitarei, M. Yusupov, J. Razzokov, B. Shokri, A. Bogaerts, Transport of cystine across xC− antiporter, Archives of biochemistry and biophysics 664 (2019) 117-126.”

3.1 Introduction

Studying the three-dimensional (3D) structure of antiporters is important for conformational analysis, ion free energy calculation, substrate binding and the evaluation of the light and heavy subunit functions in the amino acid transport cycle. One of the most powerful tools for identification of the atomic 3D structure of membrane transporter proteins is x-ray crystallography [148]. Unfortunately, the structural investigation of HATs at the atomic scale is limited to the study of prokaryotic homologues of the light subunit [51] and of the ectodomain (i.e., the domain that extends into the extracellular space) of the heavy subunit. The lack of crystal structures of the LAT family, including that of xCT, makes it difficult to determine the exact amino acid residues [149] which play an essential role in the translocation mechanism of these transporters. Homology modeling [150] and simulation techniques, such as molecular dynamics (MD) [151], could contribute to a better understanding of this mechanism.

Three different conformations, i.e., OF, OCC and IF have been reported for e.g., AdiC [90], GadC [91] and xCT, based on the crystal structure of these proteins. First, *CYC* binds to an OF conformation (see Figure 3.1). Subsequently, during the closure of the outer side and the transition to an IF state, the opposite side of the membrane becomes available to release *CYC* to the cell interior. During the transport of *CYC* and the transition from the OF to the IF state, the binding site of xCT becomes partially or completely occluded, i.e., OCC.

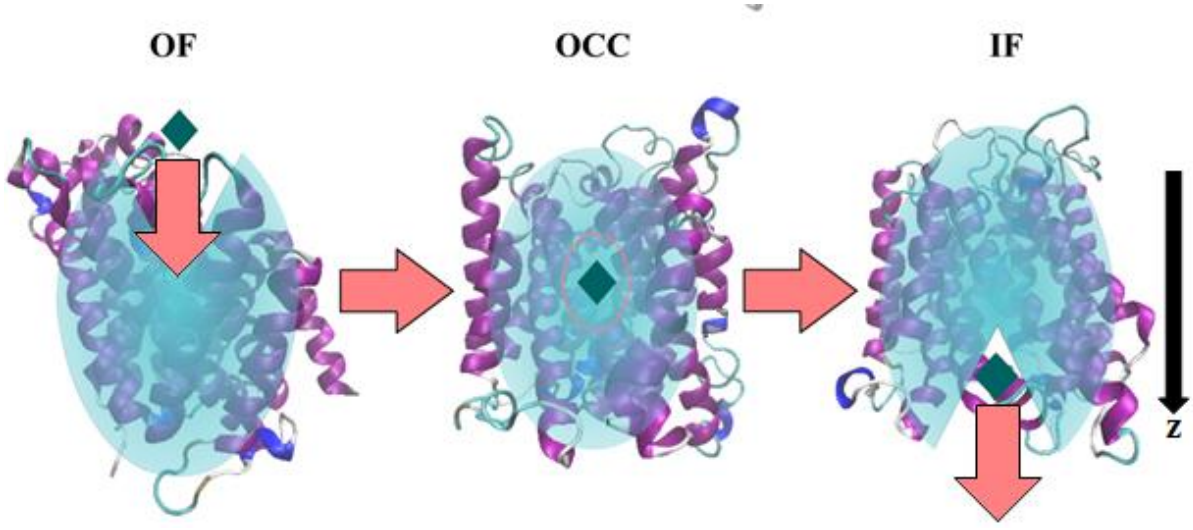

Figure 3.1. Schematic representation of the three different states of the xCT subunit of the xC^- antiporter, i.e., OF, OCC and IF. CYC is presented as green diamond. A thin arrow indicates the transition of CYC from the extracellular to the intracellular part of the membrane.

The structure and transport mechanism of so-called ApcT [90] transporter (which is another transporter of the same family as xCT) was first investigated by Shaffer *et al.* in 2009 [90]. They reported that tyrosine at position 97 (Tyr_{97}) of TM3 is part of the possible substrate binding site. The authors also suggested that the hypothetical substrate binding site of xCT should be arginine at position 135 (Arg_{135}), which is equivalent to Tyr_{97} (i.e., at the same position as Tyr_{97} in the amino acid sequence (see Figure 3.2)) of the ApcT transporter. To verify this claim, the alignment between the amino acid sequences of ApcT (PDB ID: 3GIA) [61] and xCT was performed, by applying the SWISS-MODEL server [152].The results clearly showed that the Arg_{135} of xCT and Tyr_{97} of ApcT are perfectly aligned to each other, having the same position in transmembrane domains. The crimson rectangular (see Figure 3.2) shows the position of these two amino acids in the sequence alignment. The first homology model for xCT was constructed by Janaschii, using the crystal structure of ApcT (PDB ID: 3GIA) [61].

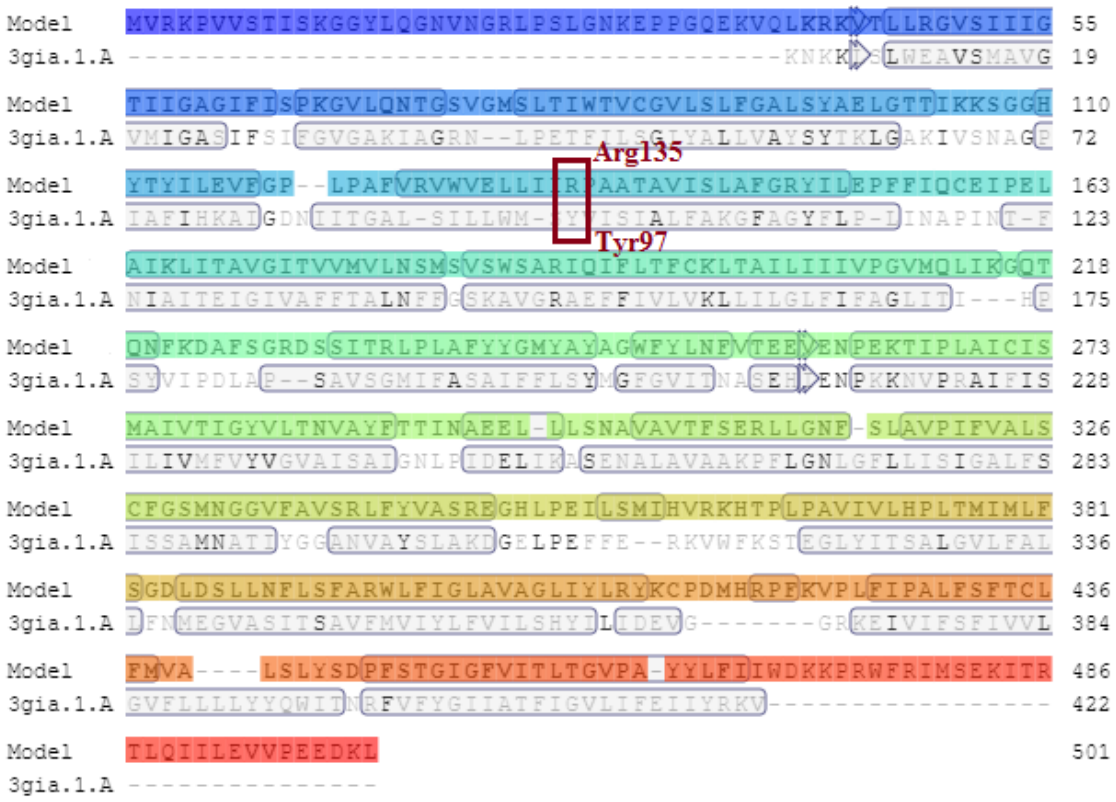

Figure 3.2. The model-template alignment of xCT sequences with structure of 3GIA. The crimson rectangular shows the position of Arg_{135} of xCT and Tyr_{97} of ApcT in the sequence alignment.

In 2010 Gao *et al.* determined the crystal structure of *Arg*/Agmatine transporter (AdiC) (PDB ID: 3L1L) [153]. However, the lack of details on the structural changes, such as transitions from OF to IF state, as well as the substrate

binding/release site, explains the need for powerful computational tools to investigate these important processes.

In this Chapter, I present the results of one study. After preparation of the structure of the xCT subunit by using the homology modeling method and checking its validation (in section 3.2), and the computational details (in section 3.3), the substrate binding site was determined (in section 3.4). I used SMD to pull CYC into the OF state of the xCT, in order to find the xCT's most probable binding position. Furthermore, I used TMD to change the conformation of xCT from OF to OCC, as well as from OCC to IF structure. Prior to each TMD simulation, I performed classical MD simulations to relax the systems. I also found out the amino acids of xCT which play an important role in *CYC* binding, such as Arg_{135} and Arg_{396}. Moreover, I performed US simulations to validate my model predictions, through qualitative comparison of the computational results with experimental observations [77] (in section 3.5). Conclusions will be given in section 3.6.

3.2 Preparation of the xCT subunit structure

3.2.1 Choosing the model systems

In my simulations I focused on the OF, OCC and IF conformations of xCT, i.e., the light subunit of the xC^- antiporter, since xCT is responsible for transporting amino acids. Specifically, I studied the extracellular to intracellular translocation of *CYC* across these model systems, which might be important in cancer therapy (see section 1.6).

The 3D structure of xCT is not available in the protein data bank [154]. To study its structure and to find out its substrate binding site, I modeled this structure by using its protein sequence. Hence, to make the best model, I applied homology modeling using similar structures (or templates) to xCT from the protein data bank. Based on the Sander and Schneider alignment algorithm [155], for proteins with residue numbers in the range of 10 to 80, the threshold for similarity of target and template can be represented by the formula:

$$t_{(L)} = 290.\mathbf{15}\boldsymbol{L}^{\mathbf{-0.562}} \qquad \mathbf{3.1}$$

where L is the number of aligned residues. For proteins with more than 80 residues ($L > 80$), as in this case, the similarity threshold should be around 25%. The templates that were selected for OF and OCC conformations have enough similarities with the xCT subunit. Specifically, the OF open face of AdiC (PDB ID: 3OB6 [156]) with similarity 24.83% was chosen as a template for the OF

conformation of xCT. For the OCC conformation of xCT, the occluded face of AdiC (PDB ID: 3L1L [153]) with similarity 24.50% was applied as a template. Unfortunately, there is no template structure available with a high (i.e., ~25%) similarity to the IF conformation of xCT. Therefore, I used the IF open conformation of GadC (PDB ID: 4DJI [157]) as a template, which has the highest available similarity to the xCT subunit, i.e., 17.41% (see also the alignment between the amino acid residues of xCT (i.e., its three conformations OF, OCC and IF) and template structures in Figure 3.10, section 3.7. Appendix).

3.2.2 Preparation of the model systems

The protein sequence (FASTA) of the human xCT [74, 158] subunit was extracted from the NCBI website (https://www.ncbi.nlm.nih.gov/). The SWISS-MODEL server [152] was used to find the best templates and to make the model structures. The orientation of the model proteins into the lipid bilayer surrounding them was determined by the OPM [159] database (http://opm.phar.umich.edu/). 1-palmitoyl-2-oleoyl-sn-glycero-3-phosphocholine (POPC) molecules were used to build the lipid bilayer and ions and water molecules were added by applying the CHARMM GUI [160, 161] web server (http://www.charmm-gui.org). As mentioned in section 1.5.1, *CYC*-II is the one that can pass through xC^- antiporters [84]. The force field parameters for bonded and non-bonded interactions of *CYC*-II are not available in force field databases. Hence, similar to the procedure used by Spoel *et al.* [162], I employed Gaussian16 [163] and the CHARMM general force field (CGenFF) [109] (see https://cgenff.parachem.org), to obtain the force field parameters needed for *CYC*-II. Specifically, applying the Gaussian16 program, I used the DFT method with the standard 6-311G* basis set to optimize *CYC*-II and generate its partial charges. Afterwards, using the output from Gaussian16, I applied the CGenFF program to obtain the topology files that contain the force field parameters of *CYC*-II. These parameters are compatible with the charmm36 force field used for the rest of the system (see the parameters and topology files of *CYC* in section 3.7. Appendix).

3.2.3 Validation of the model system

The ERRAT, Verify3D and Procheck programs were used to analyze the quality of the OF, OCC and IF models (see below), applying the web server http://servicesn.mbi.ucla.edu/SAVES/ [164]. Moreover, the protein structure quality score (PSQS) was used to measure the quality of the model structures, by describing the interactions between residue pairs as well as between single

residues and solvent (see http://www1.jcsg.org/psqs/). The Verify3D program was used to determine the compatibility between the 3D structure of the model and its sequence of amino acids (1D). The ERRAT program was applied to analyze the statistics of non-bonded interactions between side chains, lipids and solvents. The Procheck program compares residues using the geometry of both residues and structure (i.e., the standard Ramachandran plot). It checks the dihedral angles ψ against φ of the residue backbone of the protein structures. Table 3.1 shows the quality scores of the OF, OCC and IF model systems. The PSQS of the models and templates had the same values, whereas the Verify3D score of the models was less than that for the templates. On the other hand, the ERRAT and ProCheck analyses showed good compatibility between the models and templates (see Table 3.1).

Table 3.1. Quality scores of the OF, OCC and IF model systems.

Structure	Verify3D (%)	PSQS	ERRAT (%)	ProCheck (%)
OF (model)	57.44	-0.3	91.57	97.3
3OB6 (template)	80.23	-0.3	98.81	92.8
OCC (model)	58.51	-0.3	80.66	96.8
3L1L (template)	81.56	-0.3	97.56	92.4
IF (model)	50.63	-0.3	77.07	94.3
4DJI (template)	86.21	-0.3	80.33	77.8

The results of the Ramachandran plot of the conformations of the three model systems are given in Table 3.2. None of the amino acids in the OCC conformation was in the outlier region. For the OF and IF configurations, the percentage of the outlier region was less than 2%, which means that less than 6 amino acids were in this region.

Table 3.2. Ramachandran plot results of the OF, OCC and IF conformations.

Structures	Favored region (%)	Allowed regions (%)	Outlier region (%)
OF model	97.3	1.7	1.0
OCC model	96.8	3.2	0.0
IF model	94.3	4.0	1.7

The topology model of the 12 TM domains of the xCT subunit was obtained experimentally by Gasol et al. [158]. Based on this model, I determined the amino acid residues that form the 12 TM domains (see Figure 3.3 (A)). Figure 3.3 (B) represents these residues in purple, while the other residues, which are not in the TM domains, are shown in black.

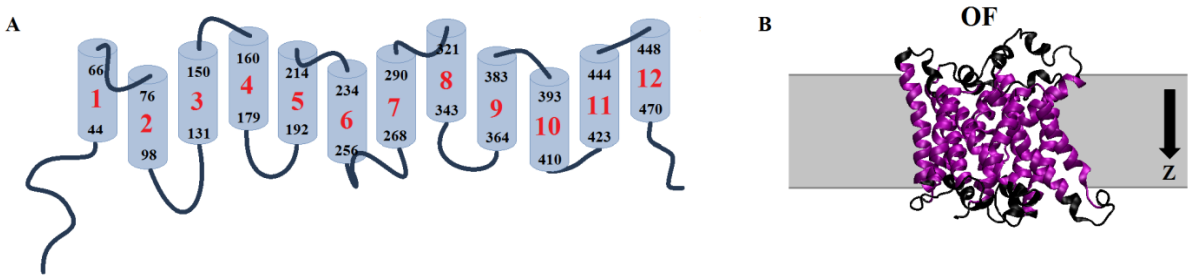

Figure 3.3. (A) Schematic representation of the 12 TM domains of the xCT subunit, with the residue numbers in each of them. (B) The residues that form the 12 TM domains are shown in purple color, while the rest are in black color, for the OF structure. The same applies to the IF and OCC structures. The membrane (region) is simply represented by the gray box. The direction of the z-axis is shown with black arrow.

These analyses of the quality of the model systems, using different programs, showed that the chosen model structures were adequate. To support this conclusion I further calculated the funnel radii of the model structures in the following section.

3.3 **Computational details**

3.3.1 MD simulation protocol

Applying the NAMD 2.12 program [137], the MD simulations were carried out in the isothermal-isobaric (NPT) ensemble at 310 K and 1 atmosphere. The CHARMM36 [114, 165] force field was used to describe the model systems, including the proteins (i.e., OF, OCC, IF), phospholipids, ions, water and CYC. Prior to the MD simulations, the systems were energy minimized using the steepest descent algorithm. The Verlet list scheme was applied with a 12 Å cutoff for both the electrostatic and van der Waals interactions. The Particle-mesh Ewald method was applied to calculate long-range electrostatic interactions. I applied the Nose-Hoover thermostat [166] in combination with a coupling constant of 1 ps and the semi-isotropic Parrinello-Rahman barostat [167] with a compressibility of $4.5 \times 10^{-5}\ bar^{-1}$ and a coupling constant of 5 ps. In all systems, the net positive charge was neutralized by adding chlorine ions to the water layer. Each system was composed of 202 phospholipids, the protein (either OF, OCC, or IF) and 15000 water molecules. All simulations were carried out

with periodic boundary conditions in a box with dimensions of $\approx 105 \times 105 \times 95$ Å^3 and a time step of 2 fs was used in all simulations.

After equilibration of all three systems (which I call simply OF, OCC and IF structures) for 500 ns (see Figure 3.11 in section 3.7. Appendix), the HOLE program [168] was used to compute the radius of the model systems' cavity along the z direction, i.e., the direction passing through the pore channel. In other words, the HOLE program was used to analyze and visualize the pore dimension through the molecular structure of the protein channels for OF, OCC and IF structure. This program proceeds along the plane perpendicular to the channel vector and finds the largest sphere without overlapping with the van der Waals surface of any atom. Subsequently, a small displacement is taken in the direction of the channel vector and this process is repeated for the next plane as well. In this study, the funnel radius was computed using more than 50 configurations, extracted from the last 50 ns of the MD trajectories of the equilibration process.

SMD was used to pull *CYC* towards the OF structure along the z direction. This procedure was repeated 5 times, employing different initial configurations extracted with a 10 ns interval from the last 50 ns of the MD trajectories. Each SMD simulation lasted for 10 ns. This is done in order to define the precise position of *CYC* at the substrate binding site, as the positions of the side chains at the substrate binding site in these configurations might differ due to the fluctuations during the MD simulation and this might affect the accuracy of the results. Using the results of the SMD simulations, the more precise position of *CYC* at the substrate binding site was defined. After pulling was completed, the system was relaxed for 6 ns, using conventional MD simulations.

Subsequently, TMD simulations were carried out to transport *CYC* across the xCT system, i.e., for permeation of *CYC* into the OF configuration, staying in the OCC structure and moving out from the IF conformation (see Figure 3.4). Initially, 10 ns TMD was performed to guide *CYC* into the OF structure (step 1 in Figure 3.4), applying an elastic constant of $2500\ kcal.mol^{-1}.\text{Å}^{-2}$. This transportation was continued up to the target position of *CYC*, which was determined by the results of the SMD simulations. After that, the transition of the structure from the OF to the OCC state was performed, applying TMD for again 10 ns (step 2 in Figure 3.4). In this simulation, the backbone of the equilibrated OCC conformation was used as the target structure. In other words, all atoms of the OF structure were guided towards a final (i.e., the OCC) structure by means of steering forces. Subsequently, the transition from the OCC to the IF state was

carried out again by using TMD for 10 ns (step 3 in Figure 3.4). Finally, *CYC* was moved out from the IF structure using another 10 ns TMD (step 4 in Figure 3.4). This entire procedure was repeated using the last conformations of the 5 relaxed systems. As in the case of SMD, all TMD simulations were followed by 6 ns conventional MD simulations to relax the system.

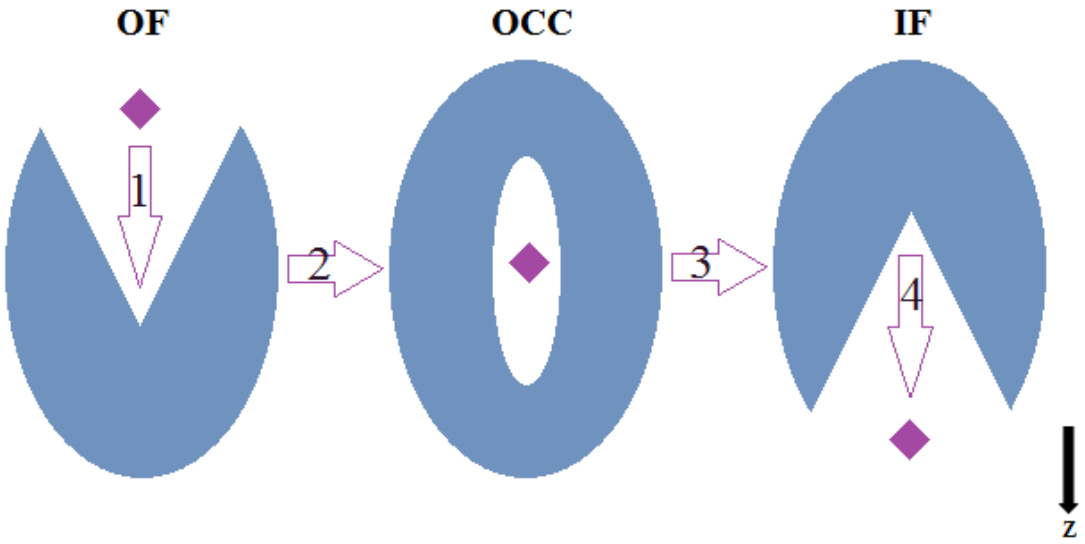

Figure 3.4. The steps of the CYC transportation across xCT. Step 1: Using TMD, CYC from the top of the OF structure was guided into the protein till its substrate binding site (or target position). Step 2: Conventional MD was performed to relax the system, followed by TMD to transform the system from the OF to the OCC state. Step 3: Again conventional MD was carried out, followed by TMD to change the system from the OCC into the IF state. Finally, in step 4, CYC was moved out from the IF state using again TMD, followed by the relaxation of the system performed by conventional MD

I used the NAMD Energy plugin of the VMD software [169] to compute the non-bonded energy between *CYC* and each amino acid of the OF, OCC and IF structures, located at a distance less than 12 Å from *CYC*. Note that the NAMD Energy plugin calculates the energy of either one or two selected structures (or molecules); if only one structure is selected, the internal and interaction energies of that structure are calculated, whereas if two different structures are selected, only the interaction energies between these structures are calculated.

3.3.2 US simulations protocol

It was found experimentally [77] that the mutation of Cys_{327} to *Ala* within xCT makes the *CYC* uptake into cells more difficult. To check this, as well as to validate my simulation results, I performed US simulations applying the GROMACS 5.0.4 package [170, 171]. As model systems in my US simulations, I used the native and modified (i.e., Cys_{327} to *Ala*) structures of the OF

configuration, as well as the native structures of the OCC and IF structures. For the mutation of Cys_{327} to *Ala*, I used the free PYMOL version 1.4.1-3 [172].

Prior to the US simulations, the HOLE program was used to find the starting and end positions of *CYC* for pulling into the systems. The points presented in Figure 3.5 (i.e., a, b, c, d, e and f) indicate these positions of *CYC* in the OF, OCC and IF structures, which were used in the US simulations. For instance, in the OF structure, the initial position of *CYC* (see point a in Figure 3.5) was in the extracellular milieu, i.e., at -3.9 nm distance from the center of mass (COM) of the protein (i.e., close to the aperture of the OF channel). The harmonic biasing force was applied to pull *CYC* against the OF's COM with a force constant of $1000\ \mathrm{kJ.mol^{-1}.nm^{-2}}$ and a pulling rate of $0.01\ nm.ps^{-1}$. The pulling was performed in the periodic direction geometry along the z direction for 1100 ps in the OF and IF system and 600 ps in the OCC system. For each energy profile, 98 windows were extracted for both native and modified form of the OF structure. The same procedure was applied for the US simulation of the OCC and IF structures, but the number of umbrella windows was somewhat different, i.e., 46 windows were extracted for the OCC and 75 for the IF structures. The windows in these simulations were all separated by $\leq 0.1\ nm$. Note that in this manner, the sampling windows spanned the entire system ranging from –3.9 till +3.9 along the z direction, where both minimum and maximum positions corresponded to intracellular and extracellular water phases, respectively. Each US simulation lasted for 20 ns, where the last 15 ns was used for construction of the free energy profiles. Each free energy profile was calculated using a periodic version of the weighted histogram analysis method (WHAM) [173]. The final free energy profile was obtained over four free energy profiles for each system. In total, $98 \times 4 + 46 \times 4 + 75 \times 4 = 876$ US simulations were performed to obtain the free energy profiles.

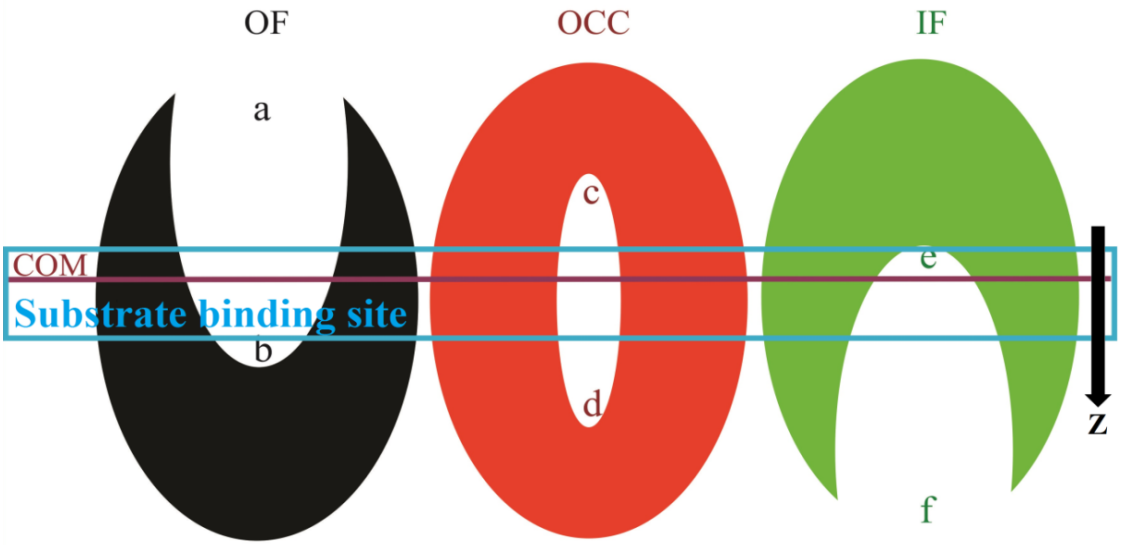

Figure 3.5. Initial and final positions of CYC used in the US simulations for the OF (a and b), OCC (c and d) and IF (e and f) states of xCT. The approximate position of the COM and the substrate binding site of all structures are indicated by the red line and blue rectangle, respectively.

3.4 Determination of substrate binding site

As mentioned in section 3.3.1, I used SMD, TMD and subsequent conventional MD simulations to study the transport of *CYC* through xCT, more specifically through the OF, OCC and IF structures. SMD was used to pull *CYC* towards the OF state along the z direction, in order to find its most probable position in the substrate binding site of the OF structure. Subsequently, I performed TMD to clarify whether this position is energetically favorable. Further, I again applied TMD to transform the OF to the OCC structure, as well as from the OCC to the IF structure, and I analyzed the substrate binding site through examining the residues surrounding *CYC* and calculating their interaction energies with *CYC*. Conventional MD was used between each process to relax the systems.

3.4.1 Funnel radii of the OF, OCC and IF structures

I calculated the funnel radii of the OF, OCC and IF structures, in order to examine whether the chosen model systems are sufficient to describe their channels.

Figure 3.6 shows the profiles of the average funnel radii as a function of position along the transporter axis (i.e., z direction), calculated for the OF, OCC and IF structures. The OF state of the xCT subunit was open to the extracellular

milieu and access to the substrate binding site was only available from the outside of the cell (see black curve in Figure 3.6). Moreover, the structure was completely closed at around $z = 5$ Å, and water molecules were unable to pass through the protein, showing no access from the intracellular fluid. On the other hand, the OCC state was partially closed (cf. the initial and final funnel radii of the OCC structure, red curve in Figure 3.6), having a cavity in the middle of the structure, which let *CYC* move freely. It was still closed to the intracellular milieu and water molecules could not enter from this site due to the small size of the channel (see funnel radius at $z = 5–11$ Å). Finally, the IF structure was completely closed for the extracellular milieu, but it was open to the intracellular fluid. Hence, the substrate binding site was accessible to the intracellular fluid, which allowed *CYC* to move towards the inside of the cell (see green curve in Figure 3.6). These results on the funnel radii showed again that the chosen model systems were adequate and that they appropriately described their channels.

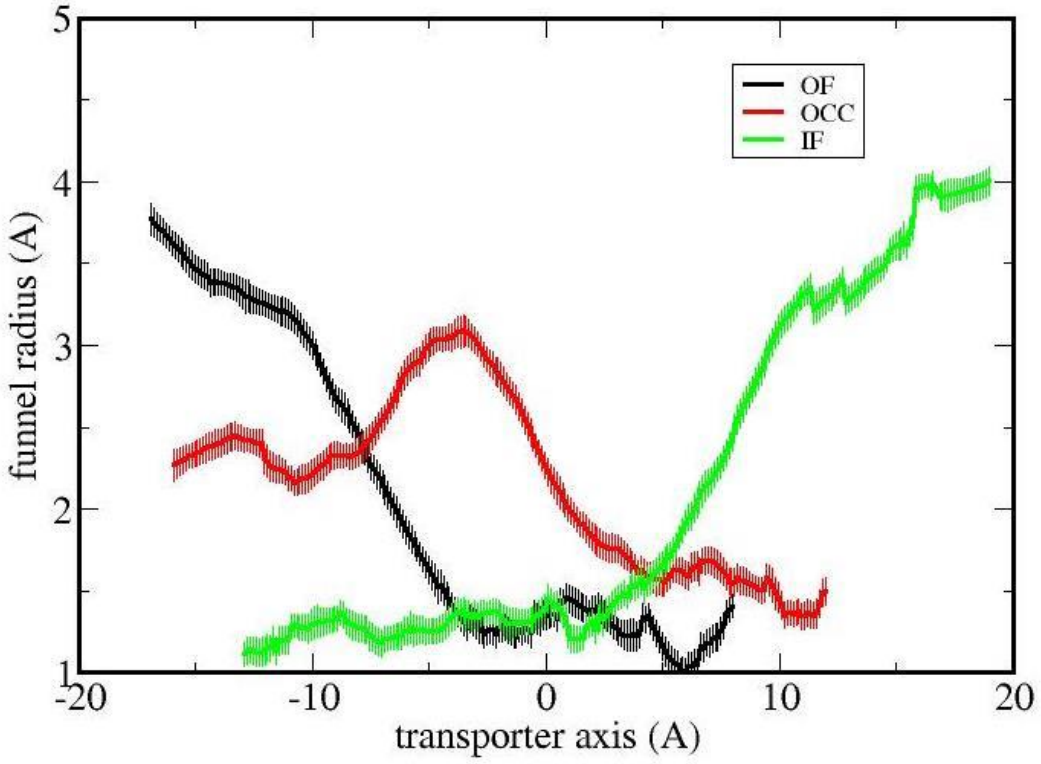

Figure 3.6. Funnel radii versus position along the transporter axis, calculated for the OF (black), OCC (red) and IF (green) structures. The radii are averaged over the last 50 ns of the equilibration runs.

3.4.2 Determination of the substrate binding site in the OF conformation

The results of SMD are summarized in Figure 3.7. As is clear from Figure 3.7

(B), *CYC* was trapped between two *Arg* residues with positive charges (i.e., Arg_{135} and Arg_{396}), which form strong electrostatic interactions with the negatively charged *CYC* substrate. Figure 3.7 (A) shows the time evolution of the average distance between the C_α of *CYC* and these two *Arg* residues. *CYC* could not escape from the attraction of these residues and the distance between them remained constant (i.e., less than 5 Å) after 5 ns, even if the pulling was still continued. Thus, these *Arg* residues play an important role as *CYC* binding sites

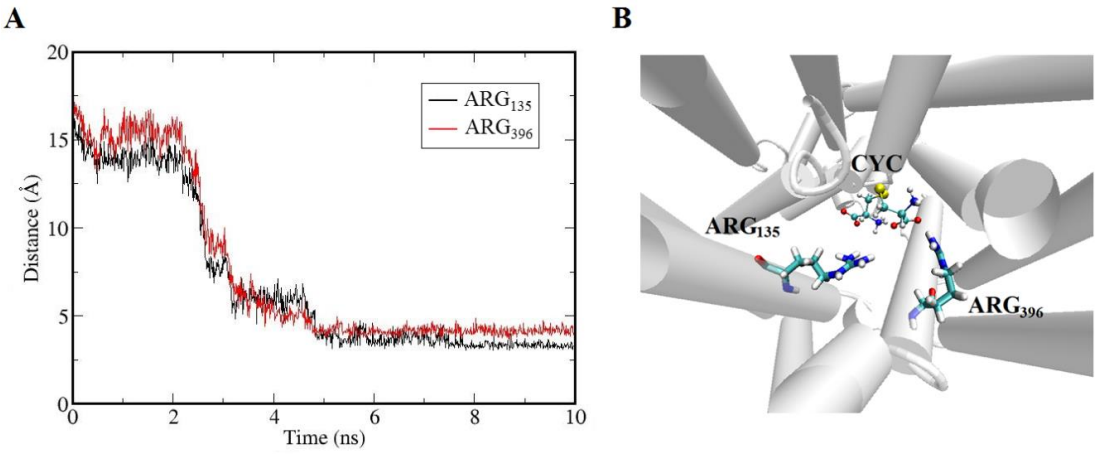

Figure 3.7. (A) Average distances between CYC and two Arg residues (i.e., Arg_{135} and Arg_{396}) positioned at the substrate binding site. (B) Position of CYC in the vicinity of the positively charged Arg_{135} and Arg_{396}. These residues strongly interact with the negatively charged CYC and do not let it move into the protein.

To verify this, I subsequently performed TMD (and conventional MD) simulations. Specifically, I calculated the non-bonded energy between *CYC* and all amino acids of the OF structure, located at a distance less than 12 Å from *CYC*, applying the NAMD Energy plugin. Table 3.3 illustrates the average non-bonded energies between *CYC* and the seven mostly interacting amino acids, i.e., with the highest absolute non-bonded energies with *CYC*. This table also presents the non-bonded energy of *CYC* with all aromatic residues (i.e., *Phe*, *Tyr* and *Trp*, if any), located within 12 Å around *CYC*. I included the aromatic residues, as they could form a cation-π interaction, i.e., interaction between the benzene groups of the aromatic residues and the protonated amino group of *CYC*. Note that there were also other residues which might interact with *CYC*, but their relative non-bonded energies were lower than those shown in Table 3.3. However, the energies of these residues were considered when calculating the total non-bonded energy of *CYC* (see below). As is clear in Table 3.3, Arg_{135} of TM3, Arg_{396} of TM10 and Arg_{126} between TM2 and TM3 had strong attractive interactions with *CYC*. Indeed, the positively charged guanidino groups of these amino acids formed a

strong electrostatic attraction with the carboxylate groups of *CYC* (see e.g., Figure 3.7 (B)). On the other hand, Glu_{130} exhibited a strong repulsive interaction, since it also had a negatively charged carboxylate group, like *CYC*. Other amino acids (i.e., Lys_{198}, Arg_{340} and Glu_{257}) and the aromatic residues did not form strong interactions. In general, the total non-bonded energy between *CYC* and all residues found within 12 Å from *CYC*, was equal to $-53.68 \pm 0.67\ kJ.mol^{-1}$, which indicated that *CYC* had overall a strong attractive interaction with the substrate binding site. Note that a lot of other amino acid residues contributed to this total energy, which explains why this value is not the same as the sum of the values defined in Table 3.3.

Table 3.3 Non-bonded energies of CYC with the seven mostly interacting amino acids, as well as with the aromatic residues of the OF structure, located within 12 Å *from CYC, i.e., in the substrate binding site.*

Mostly interacting amino acids	Non-bonded energy (kJ/mol)
Arg_{135}	-193.142±1.924
Arg_{396}	-138.792±0.648
Arg_{126}	-130.160±0.740
Lys_{198}	-38.493±0.414
Glu_{130}	237.977±0.887
Arg_{340}	-48.237±0.246
Glu_{257}	24.974±0.207
Aromatic	-29.468±0.828

3.4.3 Occlusion of the OF structure

The transition from the OF to the OCC structure led to a change in positions of the amino acid residues, including those located in the substrate binding site. Table 3.4 shows the average non-bonded energies of *CYC* with the seven mostly interacting amino acids and with the aromatic residues (see Table 3.3 in previous section), for the OCC structure. The attractive energy between *CYC* and Arg_{396} reduced significantly, due to an increasing distance between them. Moreover, the energy increased between *CYC* and Lys_{198} of TM5 (cf. Table 3.3 and Table 3.4). Furthermore, Arg_{135} of TM3 was still the most attractively interacting amino acid with *CYC* (see Table 3.4 and Figure 3.12 A in section 3.7. Appendix for more details).

Table 3.4 Non-bonded energies of CYC with the seven mostly interacting amino acids, as well as with the aromatic residues of the OCC structure, located within 12 Å from CYC, i.e., in the substrate binding site.

Mostly interacting amino acids	Non-bonded energy (kJ/mol)
Arg_{135}	-138.791±0.647
Arg_{396}	-24.491±0.138
Arg_{126}	-14.288±0.159
Lys_{198}	-62.291±0.899
Glu_{130}	49.580±0.401
Arg_{340}	-50.170±0.494
Asp_{384}	71.914±0.477
Aromatic	-60.141±0.837

Interestingly, the repulsive energy between *CYC* and Glu_{130} also reduced (cf. Table 3.3 and Table 3.4) due to an increasing distance between them. In addition, Asp_{384} now interacted with *CYC* instead of Glu_{257} found in the OF structure (cf. Table 3.3 and Table 3.4).

Overall, the total non-bonded energy between *CYC* and all residues located within a distance of 12 Å was found to be $-55.23 \pm 0.12\ kJ.mol^{-1}$, which was slightly more negative than in the case of the OF structure. This means that *CYC* still experienced an attractive interaction at the substrate binding site of the OCC structure, with even a slightly higher energy.

3.4.4 Transition from the OCC to the IF structure

Study of the transition of the OCC to the IF structure is essential, as it allows to define the residues at the substrate binding site before release of *CYC*, and their interaction energy with *CYC* explains whether *CYC* was able to be released into the intracellular fluid. Analysis of the RMSD of each amino acid residue over time showed that the residues of TM5 and TM8 had the largest displacements during this transition (see Figure 3.12 B in section 3.7. Appendix). Moreover, the slight movements of the amino acid residues of TM1, TM4, TM9, TM10, TM11 and TM12 were enough to affect the conformational changes. These movements resulted in the release of *CYC* into the intracellular fluid. Table 3.5 summarizes the results of these movements. It was clear that in the IF conformation, Lys_{198} played an important role in the substrate binding site; its strong interaction with *CYC* was a result of the TM5 movements. I clearly saw a further decrease of the attractive energy of Arg_{135} compared to OF and OCC structures (cf. Table 3.3,

Table 3.4 and Table 3.5).

This was due to a strong interaction of *CYC* with Lys_{198} positioned closer to the aperture, which brought *CYC* closer to the intracellular fluid, and thus further away from Arg_{135}. The total non-bonded energy between *CYC* and all amino acid residues within a distance of 12 Å was equal to $-42.72 \pm 0.50\ kJ.mol^{-1}$. This energy was less negative than for the OF and OCC structures, which indicated that *CYC* could more easily be released into the intracellular fluid.

Table 3.5 *Non-bonded energies of CYC with the seven mostly interacting amino acids, as well as with the aromatic residues of the IF structure, located within 12* Å *from CYC, i.e., in the substrate binding site.*

Mostly interacting amino acids	Non-bonded energy (kJ/mol)
Arg_{135}	-85.680±0.627
Arg_{396}	-56.643±0.514
Arg_{148}	-34.986±0.221
Lys_{198}	-337.681±2.464
Glu_{130}	44.170±0.899
Arg_{340}	-45.827±0.214
Lys_{67}	-28.296±0.157
Aromatic	-79.245±0.973

3.5 US simulations

To support the results obtained in section 3.4, I performed US simulations in order to calculate the free energy profiles for transport of *CYC* through the OF, OCC and IF structures. Figure 3.8 illustrates the free energy profiles of *CYC* across the native OF, OCC and IF structures. Note that these free energy profiles were calculated with respect to the water phase in the cases of OF and IF (see Figure 3.8 A), whereas in the OCC case the minimum energy of *CYC* was chosen as a reference state (Figure 3.8 B). The latter was done, since the water phase cannot be used as a reference state. Thus, the energy values obtained for OCC cannot be compared with the energy values of OF and IF (cf. Figure 3.8 A and B). The obtained free energy minima of *CYC* indicated the substrate binding site, which is shown within the blue rectangle. These free energy minima were $-33.09 \pm 4.16\ kJ\ mol^{-1}$ and $-17.14 \pm 2.38\ kJ\ mol^{-1}$, for the OF and IF structures, respectively. The free energy minima were located at –0.22 nm, 0.09 nm and 0.52 nm from the COMs of the OF, OCC and IF structures, respectively.

This indicated that the position of the substrate binding site changed during the transport and it moved towards the intracellular fluid. These alterations in the position of the substrate binding site, as well as in the amino acid residues surrounding *CYC* at the binding site (see previous sections), guided *CYC* towards the intracellular fluid. This was also obvious from the free energy minimum of *CYC*, which increased in the case of the IF conformation, indicating that a lower energy was required to release *CYC* from the antiporter.

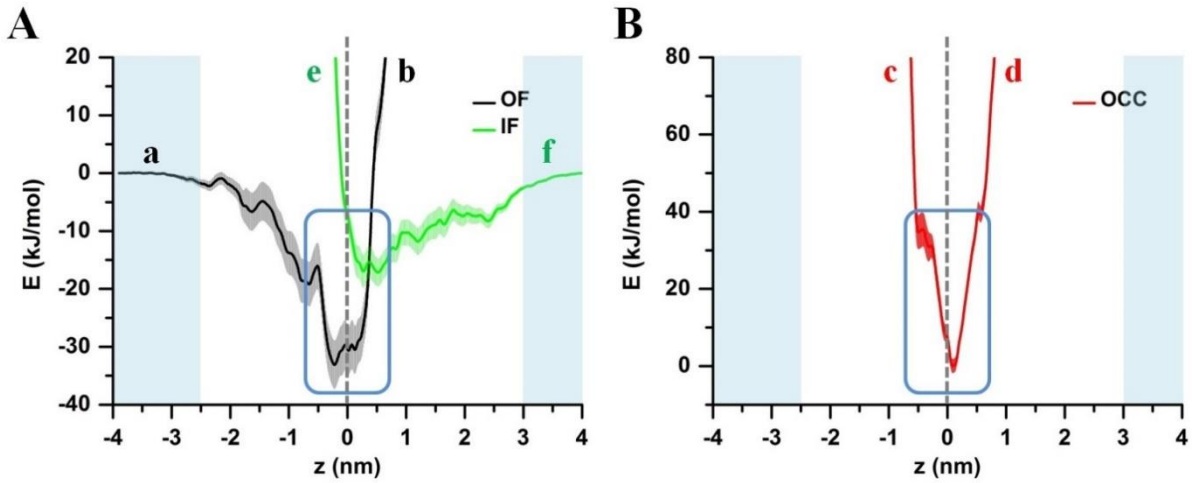

Figure 3.8. Free energy profiles for the translocation of CYC across the (A) OF and IF and (B) OCC states of xCT. The positions of the COM and the substrate binding site are indicated by the gray dashed line and blue rectangle, respectively. The letters a-f refer to the positions in Figure 3.5.

Finally, I studied the effect of a mutation in the xCT antiporter on the permeation of *CYC*, and more specifically the mutation of Cys_{327} to *Ala*, which was reported in literature to make the *CYC* uptake into cells more difficult [77]. This study allowed us to qualitatively check the validity of my simulations, and to elucidate the reason for this effect at the molecular level. The result is shown in Figure 3.9, where the free energy profiles of *CYC* for the native and mutated OF structures are compared.

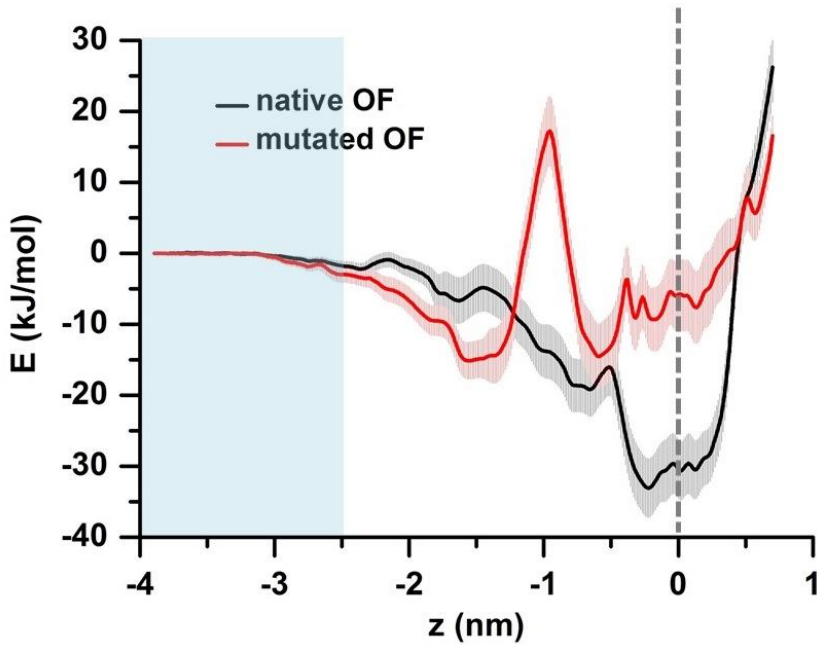

Figure 3.9. Free energy profiles for the translocation of CYC across the native and mutated OF structures (mutation of Cys_{327} to Ala).

The mutation of Cys_{327} to *Ala* in the OF structure created an extra barrier of 32.4 $kJmol^{-1}$, in the free energy profile (see red curve in Figure 3.9), making the *CYC* penetration to the substrate binding site more difficult. Furthermore, due to conformational changes in the mutated OF structure, the free energy profiles of *CYC* translocation had its minimum energy at around –1.5 nm, i.e., close to the extracellular region, making its motion more difficult towards the inside of the OF structure. This was in qualitative agreement with literature, as it was found that the mutation of Cys_{327} of TM8 to *Ala* decreased the *CYC* uptake by the xC^- antiporter [77]. Thus, my computation results support the experimental observations, which could serve as a qualitative validation of my simulations.

Based on literature, Cys_{327} of TM8 plays a critical role in *CYC* transporting [77]. The mutation of this residue to Ala could lead to depletion of *CYC* transport through the xC^- antiporter. Indeed, Ala, a nonpolar and aliphatic amino acid, contains a methyl group as a side chain [42]. Hence, it was hardly involved in the transport function of xC^-, explaining why *CYC* translocation became indeed more difficult.

3.6 Conclusion

I studied the transport of *CYC* across the xCT subunit of the xC^- antiporter. This might be important as future cancer therapy target. Indeed, in cancer cells

an enhanced transport of *CYC* across the xC^- antiporter is observed, and this protects the cancer cells from intracellular oxidative stress. If the *CYC* uptake can be inhibited, this would reduce the cellular protection from oxidative stress, as well as cancer cell drug resistance, eventually leading to cancer cell death. However, before the *CYC* uptake can be inhibited, I need to better understand the mechanism of *CYC* transport across the xC^- antiporter at the molecular level. For this purpose, I constructed three model systems (i.e., the OF, OCC and IF structures) and I simulated the permeation of *CYC* across these systems, applying different simulation techniques. The accuracy of these model systems was verified using different programs and the structures of their channels were determined by calculation of their funnel radii. To find the *CYC* binding site in the OF, OCC and IF structures, I used SMD, TMD and conventional MD simulations. Analysis of the local (i.e., around the *CYC* binding site) and global conformational changes in these structures reveals the precise locations of the binding site, as well as the amino acid residues involved in this region, through calculation of the non-bonded energies between *CYC* and these residues. One of the important residues in the substrate binding site was found to be Arg_{135} of the TM3 domain, which exhibits different binding energies with *CYC*, depending on the conformations of the xCT antiporter, having the strongest interaction in the case of the OF conformation. The free energy profiles of *CYC* across the OF, OCC and IF structures, calculated with US simulations, showed that the energy minimum of *CYC* is higher in the IF conformation. This indicates that a lower energy is required to release *CYC* from the antiporter. Finally, the effect of the mutation of Cys_{327} to *Ala* in the OF structure was studied, by calculating the free energy profiles of the native and mutated OF structures, again with US simulations. I found that this mutation makes the *CYC* transportation across the xCT antiporter more difficult, leading to a decrease of the *CYC* permeation rate. This is in qualitative agreement with experiments [77], where a drop of the *CYC* uptake by the xC^- antiporter was observed upon this mutation. My findings indicate that the chosen model systems are adequate and the obtained results support the experiments.

This study is important, since it elucidates the molecular level mechanisms of the *CYC* uptake by the xCT subunit of the xC^- antiporter, which affects the intracellular oxidative stress. Hence, this insight might be highly relevant for new cancer therapy studies. This will be investigated in next Chapter.

3.7 **Appendix**

Figure 3.10 shows the sequence alignment and superimposition between templates and chosen structures, for the outward facing (OF), occluded (OCC) and inward facing (IF) forms of xCT.

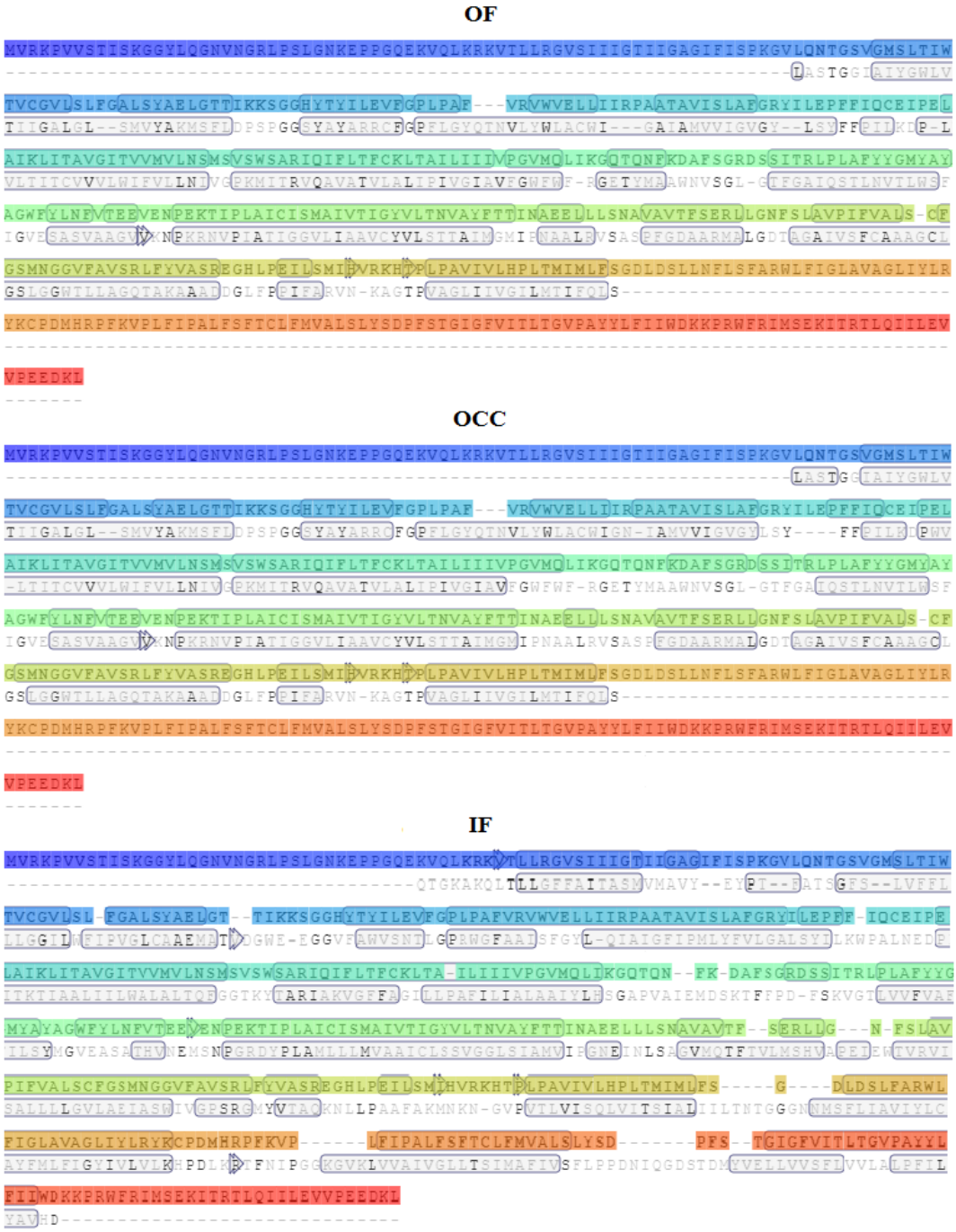

Figure 3.10. The model-template alignment of xCT sequences with three different structures: 3OB6, 3L1L and 4DJI for OF, OCC and IF conformation, subsequently.

Force field parameters for CYC

Parameters file (CYC.prm file)

```
* Parameters generated by analogy by
* CHARMM General Force Field (CGenFF) program version 1.0.0
*

! Penalties lower than 10 indicate the analogy is fair; penalties
between 10
! and 50 mean some basic validation is recommended; penalties higher
than
! 50 indicate poor analogy and mandate extensive
validation/optimization.

BONDS
CG311  NG321   263.00     1.4740 ! C:\Users , from CG321 NG321,
penalty= 4

ANGLES
CG2O3  CG311  NG321    43.70    110.00 ! C:\Users , from CG2O2 CG321
NG321, penalty= 10.5
CG321  CG311  NG321    43.70    112.20 ! C:\Users , from CG331 CG321
NG311, penalty= 6.1
NG321  CG311  HGA1     32.40    109.50   50.00   2.14000 ! C:\Users ,
from NG321 CG321 HGA2, penalty= 4
CG311  CG321  SG301    58.00    112.50 ! C:\Users , from CG311 CG321
SG311, penalty= 1
CG314  CG321  SG301    58.00    112.50 ! C:\Users , from CG314 CG321
SG311, penalty= 1
CG311  NG321  HGPAM2   41.00    112.10 ! C:\Users , from CG321 NG321
HGPAM2, penalty= 0.6

DIHEDRALS
OG2D2  CG2O3  CG311  NG321      0.5500  2   180.00 ! C:\Users , from
OG2D2 CG2O3 CG311 OG301, penalty= 33
NG321  CG311  CG321  SG301      0.2000  3     0.00 ! C:\Users , from
NG3P3 CG314 CG321 SG311, penalty= 38.9
NG321  CG311  CG321  HGA2       0.1600  3     0.00 ! C:\Users , from
NG311 CG321 CG331 HGA3, penalty= 11.2
HGA1   CG311  CG321  SG301      0.1950  3     0.00 ! C:\Users , from
HGA1 CG311 CG321 SG311, penalty= 1
CG2O3  CG311  NG321  HGPAM2     0.1600  3     0.00 ! C:\Users , from
CG2O2 CG321 NG321 HGPAM2, penalty= 10.5
CG321  CG311  NG321  HGPAM2     0.1000  3     0.00 ! C:\Users , from
CG331 CG321 NG311 HGP1, penalty= 16.4
HGA1   CG311  NG321  HGPAM2     0.0100  3     0.00 ! C:\Users , from
HGA2 CG321 NG321 HGPAM2, penalty= 4
CG2O3  CG314  CG321  SG301      0.2000  3     0.00 ! C:\Users , from
CG2O3 CG314 CG321 SG311, penalty= 1
NG3P3  CG314  CG321  SG301      0.2000  3     0.00 ! C:\Users , from
NG3P3 CG314 CG321 SG311, penalty= 1
HGA1   CG314  CG321  SG301      0.1950  3     0.00 ! C:\Users , from
HGA1 CG314 CG321 SG311, penalty= 1
CG311  CG321  SG301  SG301      0.3100  3     0.00 ! C:\Users , from
CG331 CG321 SG301 SG301, penalty= 1.5
```

```
CG314  CG321  SG301  SG301      0.3100  3     0.00 ! C:\Users , from
CG331 CG321 SG301 SG301, penalty= 17.9

IMPROPERS

END
```

Topology file (CYC.rtf file)

```
* Topologies generated by
* CHARMM General Force Field (CGenFF) program version 1.0.0
*
36 1

! "penalty" is the highest penalty score of the associated parameters.
! Penalties lower than 10 indicate the analogy is fair; penalties
between 10
! and 50 mean some basic validation is recommended; penalties higher
than
! 50 indicate poor analogy and mandate extensive
validation/optimization.

RESI CYC           -1.000
GROUP            ! CHARGE   CH_PENALTY
ATOM SG1    SG301  -0.117 !   21.548
ATOM CB1    CG321  -0.060 !   23.022
ATOM HB1    HGA2    0.090 !    0.810
ATOM HB2    HGA2    0.090 !    0.810
ATOM CA1    CG311  -0.002 !   16.801
ATOM C1     CG2O3   0.614 !   10.156
ATOM HA1    HGA1    0.090 !    0.522
ATOM OXT1   OG2D2  -0.760 !    1.650
ATOM O1     OG2D2  -0.760 !    1.650
ATOM N1     NG321  -0.777 !   21.061
ATOM H2     HGPAM2  0.296 !   12.047
ATOM H1     HGPAM2  0.296 !   12.047
ATOM SG2    SG301  -0.052 !    3.980
ATOM CB2    CG321  -0.164 !   31.138
ATOM HB3    HGA2    0.090 !    2.500
ATOM HB4    HGA2    0.090 !    2.500
ATOM CA2    CG314   0.386 !  102.891
ATOM C2     CG2O3   0.445 !   99.918
ATOM HA2    HGA1    0.090 !    3.995
ATOM O2     OG2D2  -0.760 !    8.256
ATOM OXT2   OG2D2  -0.760 !    8.256
ATOM N2     NG3P3  -0.355 !   37.595
ATOM H5     HGP2    0.330 !    2.536
ATOM H4     HGP2    0.330 !    2.536
ATOM H3     HGP2    0.330 !    2.536

BOND H1   N1
BOND HB2  CB1
BOND N1   H2
BOND N1   CA1
BOND HB3  CB2
BOND HB4  CB2
BOND OXT1 C1
BOND CB2  SG2
BOND CB2  CA2
```

```
BOND HB1   CB1
BOND CB1   CA1
BOND CB1   SG1
BOND OXT2  C2
BOND H4    N2
BOND CA1   C1
BOND CA1   HA1
BOND C1    O1
BOND SG2   SG1
BOND C2    O2
BOND C2    CA2
BOND CA2   N2
BOND CA2   HA2
BOND N2    H3
BOND N2    H5
IMPR C1      O1      OXT1    CA1
IMPR C2      OXT2    O2      CA2

END
```

MD simulations

Figure 3.11 illustrates the time evolution of the root mean square deviation (RMSD) of the backbone for the OF, OCC and IF configurations of xCT.

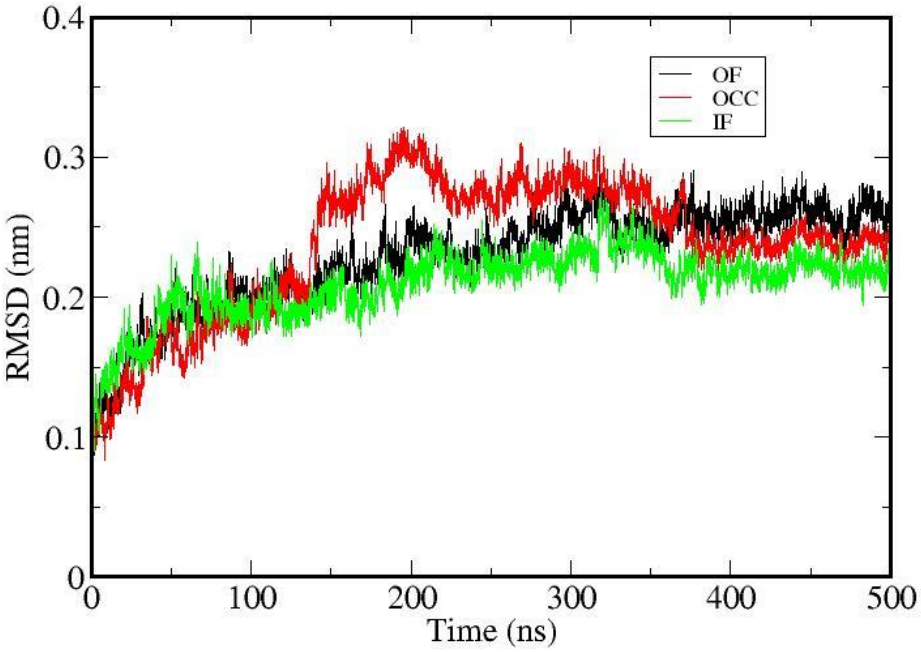

Figure 3.11. RMSD of the backbone of the OF (black), OCC (red) and IF (green) forms of xCT, obtained from 500 ns equilibration runs.

As is clear, all structures reach their equilibration after 400 ns and stay stable in the rest of the simulation time, yielding an RMSD fluctuating between 0.2–0.28 nm. These results indicate that all three structures are well equilibrated.

Transition from the OF to the OCC structure, as well as from the OCC to the IF structure

Figure 3.12 shows the average RMSD of each amino acid residue over time, calculated during the transition from the OF to the OCC (Figure 3.12 A) as well as from the OCC to the IF (Figure 3.12 B, see next section), respectively. The graphs are obtained by averaging the RMSDs of five different TMD simulations for each structure.

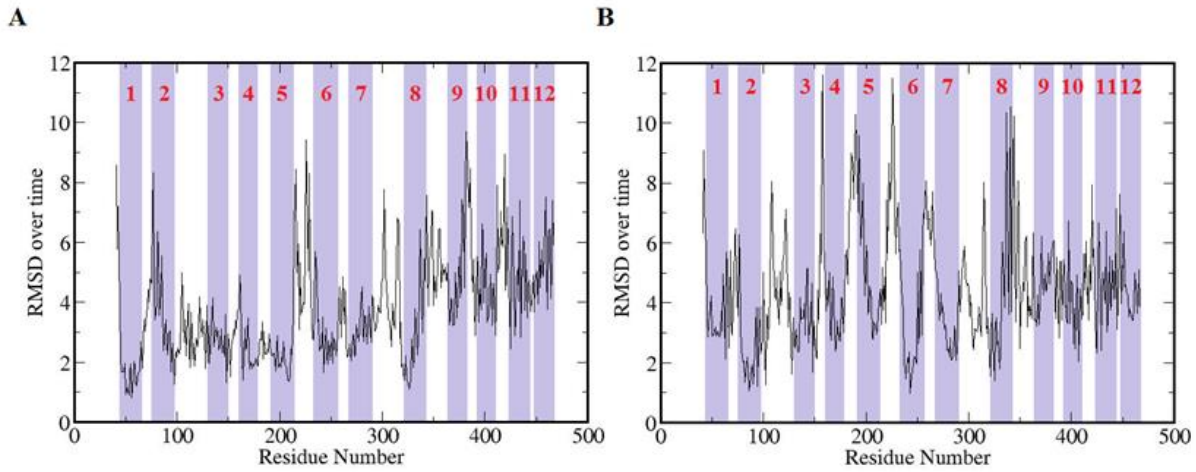

Figure 3.12. RMSD of each residue over time, obtained during the transformation from the OF to the OCC structure (A) and from the OCC to the IF structure (B), respectively. The numbers of the TM domains are given in red color.

Analysis of the calculated average root mean square deviation (RMSD) of each residue over time showed that the residues of TM2, TM9, TM10, TM11 and TM12 have the largest fluctuations during the transition from the OF to the OCC structure (see Figure 3.12 A), showing slight movements of the residues in TM4 and TM6, but this is enough to affect the conformational changes. During the transition from the OCC to the IF structure, the residues of TM5 and TM8 have the largest displacements (Figure 3.12 B), exhibiting slight movements of the residues in TM1, TM4, TM9, TM10, TM11 and TM12, which are enough to affect the local and total conformational changes (see section 3.4.4).

Chapter 4:
Oxidative stress on CYC transportation[2]

[2] Part of this chapter is published as "M. Ghasemitarei, M. Yusupov, J. Razzokov, B. Shokri, A. Bogaerts, Effect of oxidative stress on cystine transportation by xC^- antiporter, Archives of biochemistry and biophysics (2019) 108114."

4.1 Introduction

In Chapter 3:, I used homology modeling to build the three different conformations of the xCT subunit (i.e., OF, OCC and IF state), in order to investigate the *CYC* translocation from the xCT subunit. As mentioned before, *CYC* is essential for general protein biosynthesis, specifically GSH. Since intracellular GSH has a short half-life, *CYC* uptake is of high value for the cell viability. As some cancer cells do not have any endogenous *Cys*-synthetic ability, *CYC* uptake from the extracellular milieu by xC^- antiporters is important for their viability. Thus, inhibition of this antiporter in cancer cells may lead to *Cys* starvation, and thus depletion of the intracellular GSH concentration, thereby inducing apoptosis and reducing cancer cell drug resistance [38].

As mentioned in Chapter 1: and 3, Cys_{327} is one of the important amino acids of the xCT subunit. Experiments and simulations demonstrated that the mutation of this amino acid to *Ala* reduces the *CYC* uptake by the xC^- antiporter [77]. This amino acid is highly reactive and located in the vicinity of extracellular (which means that, in cancer cells, it is in contact with extracellular acidic pH), protein channel and substrate binding site [77]. Thus, it is conceivable that during the plasma treatment, this residue can most probably be oxidized by plasma-generated species. The oxidative modification of Cys_{327}, on the other hand, can influence and alter the channel conformation and hence the *CYC* uptake. In addition, *Cys* can be oxidized in different pathways at different pH situations (as mentioned in section 1.4.3). Generally, the thiol group of *Cys* is easily oxidized by ROS and RNS [86] . In fact, because of intracellular ROS, especially H_2O_2, 5% of *Cys* residues of cellular proteins are oxidized to sulfunic or cysteic acid [174]. Based on all, in this study, I investigated the effects of Cys_{327} oxidation to cysteic acid on closure of protein channel and *CYC* translocation.

In the present Chapter, I present the results of one study. By applying US simulation, I investigated the effect of Cys_{327} oxidation on the transport of *CYC* across native and oxidized OF conformation of xCT subunit.

Moreover, at section 4.4, I studied whether if CAP oxidizes membrane lipids, this lipid peroxidation will affect the xCT subunit conformation or not.

4.2 Computational details

4.2.1 Model system

The model system of the native OF conformation is composed of the OF protein embedded in a fully-hydrated palmitoyl-oleoyl-phosphatidylcholine (POPC) bilayer. This system was used in previous Chapter and a detailed explanation of its preparation is given there [175]. To construct the OF conformation of xCT, the OF open face of AdiC (PDB ID: 3OB6 [156]) antiporter was chosen as a template, applying the SWISS-MODEL server [152], since the 3D structure of this system was not available in the protein data bank. Subsequently, the OF protein was incorporated into the fully-hydrated POPC lipid bilayer, applying the CHARMM GUI web server [160, 176]. To build the oxidized OF system, I modified Cys_{327} of the native OF protein to cysteic acid (CYO_{327}), applying the GaussView software version 5.0.8 [177].

To prepare the parameters of CYO_{327}, three consecutive amino acids of the xCT subunit containing the Cys_{327} residue (i.e., Ser_{326}-Cys_{327}-Phe_{328}) were extracted from the main pdb file of OF state. After changing the Cys_{327} to cysteic acid by using GaussView software, all structures were optimized by using Gaussian software and the parameters were extracted (see next section). Based on the bond length as well as bonded and dihedral angles of optimized cysteic acid, the pdb file of CYO_{327} was prepared.

4.2.2 Molecular dynamics simulation protocols for investigation of Cys_{327} oxidation

MD simulations were carried out using the GROMACS 5.0.4 package [170, 171]. Both the native and oxidized OF systems were prepared as follows. The systems were initially energy minimized, applying the steepest descent algorithm. Subsequently, they were equilibrated for 500 ns in the isothermal-isobaric (NPT) ensemble at $310\ K$ and 1 atmosphere. These simulations were repeated three times by changing the values of the initial velocities of the atoms in the system in order to ensure that all three structures of each system are consistent. The Nose-Hoover thermostat [166] in combination with a coupling constant of 1 ps and the semi-isotropic Parrinello-Rahman barostat [167] with a compressibility of $4.5 \times 10^{-5}\ bar^{-1}$ and a coupling constant of 5 ps were applied to equilibrate the systems. The cut-off distance of both the electrostatic and van der Waals interactions was chosen as 12 Å by applying the Verlet list scheme. Electrostatic interactions were treated by the particle mesh Ewald method [178, 179] and Long-range dispersion corrections were applied for both energy and pressure. The

net positive charges of both systems were neutralized by adding chloride ions. Overall, both systems were composed of 202 POPC lipids, the native or oxidized OF protein and 15000 water molecules covering them from top (extracellular part) and bottom (intracellular part), see Figure 4.1. Both systems were simulated under periodic boundary conditions and the dimension of these systems was $\approx 105 \times 105 \times 95$ Å^3. A time step of 2 fs was used in all simulations, and the CHARMM36m force field was applied to describe the interatomic interactions in the systems in combination with the TIP3P water model [115]. The CHARMM-type force field parameters for *CYC* and cysteic acid (i.e., CYO_{327} residue, see above) of the oxidized OF system were derived as follows. Similar to the methods applied by Spoel et al. [162], to obtain the force field parameters of *CYC* and CYO_{327}, the Gaussian16 software [180] and the CHARMM general force field (CGenFF) program [109] were implemented. Specifically, to optimize the structures and compute the partial charges, the Gaussian software was used by applying DFT calculations, including the B3LYP functional with standard 6-311G* basis set. It should be noted that according to literature, cysteic acids are formed in proteins as a result of ROS or RNS interactions, and they mostly contain negative charges [174]. Therefore, I also used the negatively charged CYO_{327} in my simulations. The CGenFF program was applied to obtain the parameters for bonds, angles and dihedrals. Finally, the parameters were again renewed by adding the Gaussian-made partial charges to CGenFF-made parameters (see the parameters and topology file related to *CYO* in section 4.6. Appendix). As mentioned in Chapter 1:, section 1.3.2, the pH value of the extracellular milieu of cancer cells is mostly between 5 and 7. In this situation, the *His* residue is the only amino acid of which the charge can be changed in acidic pH environment (see Table 1.2). Study of the OF conformation of the xCT subunit shows that all *His* residues are in the vicinity of the intracellular fluid (Figure 4.1). Therefore, at the *pH* under study here, the partial charges of the amino acids do not change.

We also applied the H++ server (http://biophysics.cs.vt.edu/) to check the protonation states of amino acids in acidic pH (i.e. at pH 5). We found that except for His, the protonation states of all amino acids were the same as at their standard protonation states (i.e., pH 7). However, in this study we did not change the protonation states of the His residues, since their positions were not accessible from the extracellular milieu at pH 5 (see above).

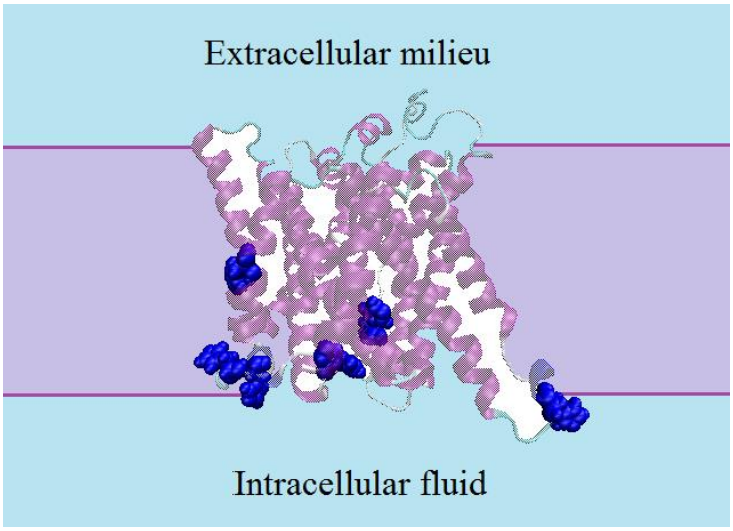

Figure 4.1. OF state of the xCT subunit: all His residues (colored in blue) are located close to the intracellular fluid. Therefore, the extracellular pH is not able to affect the charges of the His amino acid side chains. The light blue and purple colors correspond to the extracellular/intracellular water phase and lipid bilayer, respectively.

The funnel radius analysis and the US simulations (see next section) were applied after equilibration of both systems for 500 ns. Note that this equilibration time was sufficient, as the calculated root mean squared deviations (RMSDs) of both the native and oxidized OF systems showed a convergence after 400 ns (see Figure 4.11, in section 4.6. Appendix). The non-bonded (i.e., Coulomb + van der Waals) interaction energies between some amino acid residues of both systems were computed using the *gmx energy* tool of GROMACS.

4.2.3 Molecular dynamics simulation protocols for investigation of lipid peroxidation effects

I performed MD simulations based on GROMOS54a7 united atom force field for native phospholipids, to study the effect of lipid peroxidation on the protein conformation. In this simulation the OF, OCC and IF state of the xCT subunit were located into the membrane by using Packmol package [181]. The top and bottom layers of the membrane had totally 200 POPC and oxidized POPC (POPX) molecules (the parameters of the aldehyde groups of the oxidized POPC were derived from [182]. All systems with 0%, 25%, 50% and 75% POPX were equilibrated by using the GROMACS 5.0.4 package [170, 171]. The schematic figures of POPC and POPX are depicted in Figure 4.2. The POPC peroxidation has different products. The product with two aldehydes is the most stable one [2] (see Figure 4.2 (B)), which I used in this study. The simulation conditions were the same as before (see section 4.2.2), and the system size was $\approx 100 \times 100 \times 130 Å^3$.

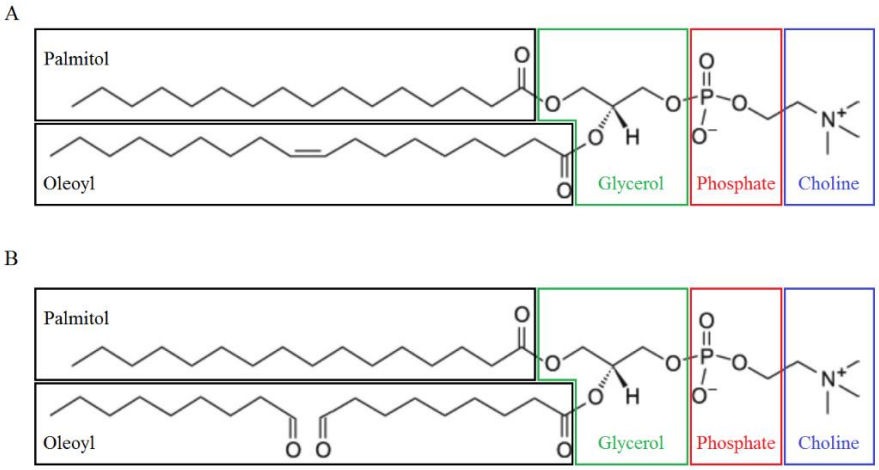

Figure 4.2 The schematic picture of POPC (A) and its oxidized structure (POPX) which is considered in this study (B).

4.2.4 Calculation of the funnel radii

I applied the HOLE program [183] to calculate the profiles of the funnel radii across the channels of both the native and oxidized OF systems (see section 4.3.1), as well as the channels of OF, OCC and IF systems located in the membrane with different combination of POPC and POPX (see section 4.4.1). This program computes the largest radius of protein channels along the channel vector (i.e., z direction in my case), without overlapping with the van der Waals surface of any atoms. Around 60 configurations were extracted from the last 50 ns of the equilibration simulations to obtain the average funnel radii along the z direction (i.e., transporter axis) for both native and oxidized OF systems as well as for all OF, OCC and IF systems located in the membrane with different combinations of POPC and POPX.

4.2.5 Umbrella sampling (US) simulations

To compute the potentials of mean force (i.e., free energy profiles (FEPs)) of *CYC* translocation across both the native and oxidized OF systems, the US method was employed. In both structures, the initial position of *CYC* was chosen in the extracellular milieu, i.e., at -3.9 nm distance from the center of mass (COM) of the protein (i.e., in the z position close to the aperture of the protein channel). *CYC* was then pulled against the COM of both systems along the z direction with a harmonic biasing force constant of $1000\ kJ.mol^{-1}.nm^{-2}$ and pulling rate of $0.01\ nm.ps^{-1}$. After pulling *CYC* for 1100 ps, 98 windows (i.e., 49 for the native and 49 for the oxidized system), separated by a distance of $\leq 0.1\ nm$, were

extracted for the US simulations for both the native and oxidized structures. In this manner, the sampling windows spanned the whole protein channel, starting from the extracellular milieu and ending at the end of the protein channel, where the channel is closed from the intracellular milieu. Subsequently, the US simulations were run for 20 ns and the last 15 ns of the trajectory was used to obtain the FEPs. To construct the FEPs the periodic version of the weighted histogram analysis method (WHAM) [173] was applied. Errors associated with the sampling were computed by the bootstrapping method. At last, the final FEP of each system was obtained by averaging over four independently calculated FEPs. These FEPs were calculated using four configurations (for each system) derived from the last 50 ns (i.e., taken at 470, 480, 490 and 500 ns) of the equilibration simulations. In total, 98×4=392 US simulations were performed to obtain the FEPs for each system.

4.3 Investigation of CYC translocation from native and oxidized OF structure

4.3.1 Funnel radii analysis

Figure 4.3 A compares the profiles of the averaged funnel radii, i.e., the largest radii of the pore channels without overlapping with the van der Waals surface of any atom, of the native and oxidized OF systems along the z direction (i.e., across their channels). It is clear that the channel of the native OF system is fully open for *CYC* passage to the substrate binding site ($z \approx -0.5\ nm$), while it is completely closed in the oxidized OF structure, preventing the *CYC* access to the substrate binding site. The latter can be seen by looking at the funnel radius for the negative values on the transporter axis, which drops to 0.1 nm around -0.8 nm of the protein channel, which is too small for *CYC* to pass, while the funnel radius of the native OF system is large enough (i.e. ~0.37 nm) in this region. The closure of the pore in the oxidized OF system blocks the access of *CYC* to the substrate binding site. Therefore, the extracellular *CYC* is not able to translocate towards the xCT substrate binding site (see also the US results below).

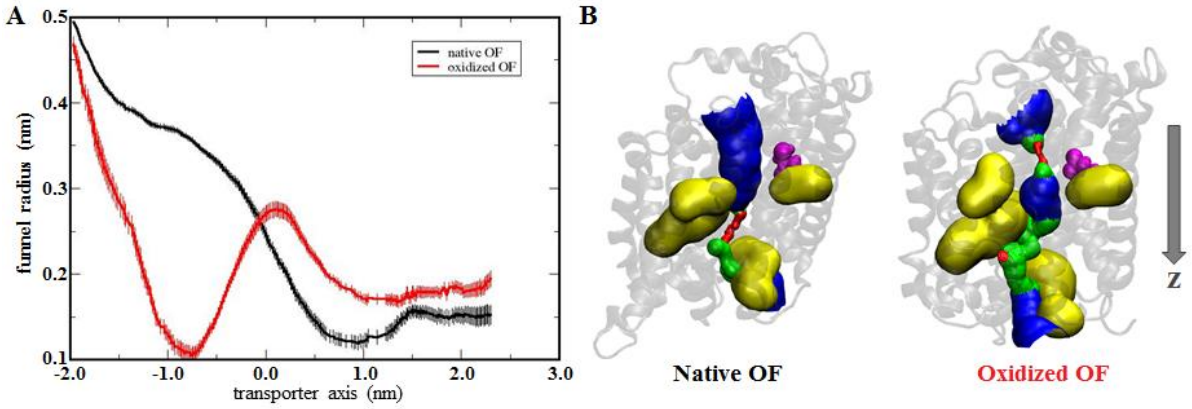

Figure 4.3 (A) Profiles of the funnel radii of the native (black) and oxidized (red) OF structures along the main axis (z direction), averaged over the 60 different profiles for each system. (B) Illustration of the changing size (pore radius) of the channels for native (left) and oxidized (right) OF structures, as well as the position of Cys_{327} (left) and CYO_{327} (right) relative to the protein channel (magenta color). Red color means pore radius smaller than 0.115 nm, green is between 0.115 and 0.230 nm, while blue indicates pore radius larger than 0.230 nm. The residues involved in the substrate binding site are illustrated in yellow color. The rest of the protein is shown in light gray Newcartoon view.

Figure 4.3 B illustrates the protein channel of the native and oxidized OF systems, and how its size varies along the z direction, which is shown in different colors (i.e., red, green and blue). The red color corresponds to very tight parts of the channels (i.e., channel radius below 0.115 nm), where even a single water molecule cannot permeate (i.e., the passage of CYC is totally blocked)). The parts with green color indicate that the channels have enough space for passage of a single water molecule, but CYC still cannot translocate (i.e., channel radius between 0.115 and 0.230 nm). Hence, only in the blue parts of the channels (i.e., radius above 0.230 nm) the passage of CYC is possible. It is obvious from Figure 4.3 B that the substrate binding site is not accessible from the extracellular milieu in the oxidized OF system, whereas it is fully accessible in the native OF system. The substrate binding site consists of residues that form temporary bonds with the substrate (i.e., *CYC*) and play an important role in guiding the substrate into the protein channel. The binding sites on proteins are critical parts of signal transduction pathways [184]. In section 3.4.2, I found that Arg_{135}, Arg_{396}, Arg_{126}, Lys_{198} and Arg_{340} are the most important residues in the substrate binding site of the OF state of the xCT subunit, as they strongly bind to *CYC*. These amino acids are illustrated in Figure 4.3 B by the yellow color, and they are accessible to *CYC* only from the protein channel. Therefore, if the channel becomes closed, they will not be accessible for *CYC* from the extracellular milieu. This is due to oxidation of Cys_{327} to CYO_{327} that leads to conformational changes in the channel, thereby affecting the *CYC* permeation (see next section).

4.3.2 Conformations of the native and oxidized OF structures

I found from previous section that the channel of the oxidized OF system is completely closed from the extracellular milieu, which is the result of Cys_{327} oxidation to CYO_{327}. Monitoring of the amino acids around the closed part showed that the rearrangements in the side chains of Tyr_{244} and CYO_{327} residues have a critical role in closure of the OF channel. Figure 4.4 shows the positions of Tyr_{244} and Cys_{327} (Figure 4.4 A), as well as Tyr_{244} and CYO_{327} (Figure 4.4 B) of the native and oxidized OF channels, respectively. The comparison of Figure 4.4 A and B clearly shows that the rotation of the Tyr_{244} side chain and the change in orientation of the CYO_{327} side chain towards Tyr_{244} leads to a closure of the channel. Indeed, the calculated distance between the alcohol group of Tyr_{244} and the sulfur atom of CYO_{327}, (i.e., ~8.2 Å, see Table 4.1) was found to be shorter than that between the alcohol group of Tyr_{244} and the sulfur atom of Cys_{327} (i.e., ~15.5 Å, see Table 4.1), resulting in a narrowing of the channel after oxidation took place.

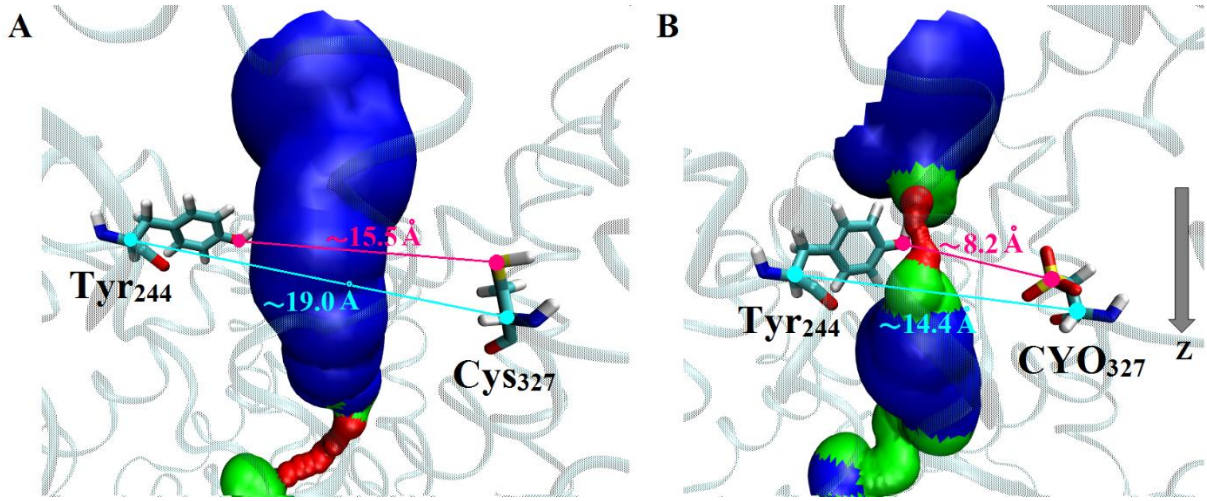

Figure 4.4 Orientations of Tyr_{244} and Cys_{327} (A) and Tyr_{244} and CYO_{327} (B) in the channels of the native (A) and oxidized (B) OF proteins, indicating the distance between the alcohol group of Tyr_{244} and the sulfur atom of Cys_{327} (~15.5 Å) (A), and between the alcohol group of Tyr_{244} and the sulfur atom of CYO_{327} (~8.2 Å) (B), and hence the narrowing of the channel upon oxidation.

Krammer et al. [185] determined that the rotameric state of Trp_{202} in the AdiC transporter structure was crucial for occlusion of the OF to OCC state. Their study stressed that the OF state of the AdiC conformation without proper rotation of the Trp_{202} side chain cannot occlude completely. This amino acid is equivalent to Tyr_{244} in the xCT subunit (i.e., at the same position as Tyr_{244} in the amino acid sequence). Thus, I believe that Tyr_{244} plays an important role in channel closure, which was the case in my study.

Table 4.1 illustrates the averaged distance between the backbones (i.e., alpha carbons) and side chains of Tyr_{244} and Cys_{327} for the native OF state and of Tyr_{244} and CYO_{327} for the oxidized OF state of the xCT subunit.

Table 4.1 Averaged distance between the backbones (i.e., C_α-C_α) and sidechains (i.e., S-OH) of Cys_{327} and Tyr_{244} in the native OF state and of CYO_{327} and Tyr_{244} in the oxidized OF proteins.

residues	C_α-C_α (Å)	S-OH (Å)
Cys_{327}-Tyr_{244} (native OF)	19.04 ± 0.03	15.47 ± 0.04
CYO_{327}-Tyr_{244} (oxidized OF)	14.44 ± 0.02	8.15 ± 0.02

It is obvious that after oxidation of Cys_{327} to CYO_{327} the overall distance between these residues and Tyr_{244} decreases, which is most clear for S-OH (i.e., drop by about a factor two). This again indicates that Cys_{327} oxidation in the OF structure leads to conformational changes in the channel, resulting in closure of this channel and hence blockage of the *CYC* uptake.

4.3.3 Analysis of the interaction energies

Table 4.2 illustrates the non-bonded (i.e., Coulomb + van der Waals) interaction energies between Cys_{327}-Tyr_{244}, Cys_{327}-rest of the system and Tyr_{244}-rest of the system in the native OF system, as well as between CYO_{327}-Tyr_{244}, CYO_{327}-rest of the system and Tyr_{244}-rest of the system in the oxidized OF system.

Table 4.2 Non-bonded (i.e., Coulomb + van der Waals) interaction energies calculated for Cys_{327}, CYO_{327} and Tyr_{244} of the native and oxidized OF systems, with each other and with the rest of the system. Note that the interaction energies between Cys_{327}-Tyr_{244} and CYO_{327}-Tyr_{244} correspond to the native and oxidized OF structures, respectively. The same applies to Cys_{327}-rest of the system and CYO_{327}-rest of the system.

protein	Cys_{327}/CYO_{327}-Tyr_{244} (kJ/mol)	Cys_{327}/CYO_{327}-rest (kJ/mol)	Tyr_{244}-rest (kJ/mol)
native OF	≈ 0	-5.1 ± 0.7	-82.2 ± 2.0
oxidized OF	≈ 0	-160.0 ± 6.2	-100.6 ± 1.3

It is obvious that after oxidation of Cys_{327} to cysteic acid (CYO_{327}), the interaction energy becomes more negative (i.e., stronger interaction) in all cases,

although the change in energy for CYO_{327}-Tyr_{244} (second column in Table 4.2) was not significant. The latter is probably because the distance between CYO_{327} and Tyr_{244} is still relatively long (~ 8.2 Å; see Figure 4.4 B and Table 4.1), which is not enough to make a H-bond, although this H-bond interaction for the S-H system is inherently weaker [186]. On the other hand, the interaction energy between CYO_{327} and the rest of the system, attributed to the attractive (namely, Coulomb) interaction of three oxygen atoms in the side chain of CYO_{327} with the surrounding amino acids, was much stronger than the energy between Cys_{327} and the rest of system (third column). In general, the movement and rotation of the side chain of Tyr_{244} and a change in the orientation of the side chain of CYO_{327} results in a rearrangement of the surrounding amino acids, bringing Tyr_{244} and CYO_{327} in the vicinity of some new amino acids, allowing to make H-bonds with some of them. These mediator amino acids are Ala_{60}, Gly_{61}, Ala_{145}, Phe_{146} and Lys_{198}, resulting in H-bonds with all of them, while they did not have any H-bonds with Cys_{327} and Tyr_{244} prior to Cys_{327} oxidation. Moreover, some other amino acids, such as Phe_{63}, Ile_{64}, Thr_{139}, Arg_{148}, Tyr_{149}, Ser_{330} and Met_{331}, make H-bonds with both CYO_{327} and Tyr_{244}, while they had H-bonds with only the backbone of Cys_{327} before oxidation. Specifically, among all mentioned amino acids, Ala_{60} and Gly_{61} are found to be the most important ones because of two reasons. Firstly, they are in the vicinity of the closed parts of the protein channel (cf. red color part in Figure 4.4 B). Secondly, they did not have any H-bonds with Cys_{327} and Tyr_{244} before oxidation. The positions of Ala_{60} and Gly_{61} relative to the channels of both the native and oxidized OF proteins are illustrated in Figure 4.5.

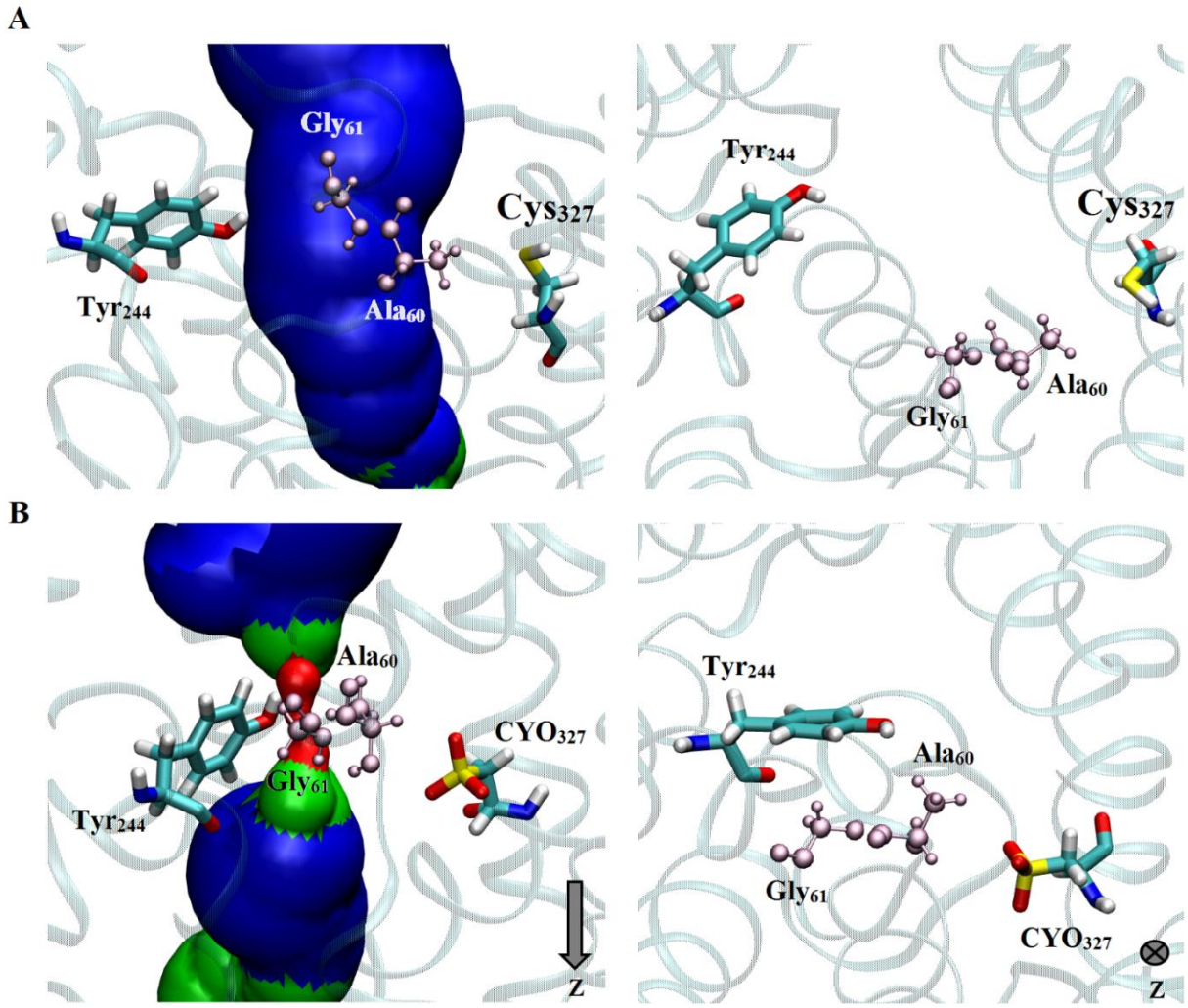

Figure 4.5 Positions of Ala_{60} and Gly_{61} (pink color) relative to CYO_{327} (or Cys_{327}), Tyr_{244} and the rest of the protein channel in the native (A) and oxidized (B) OF structure: side view (left) and top view (right). For clarity, the profile of the channel is not shown in top view.

Although in the native OF state, Ala_{60} and Gly_{61} are in the vicinity of the protein channel (Figure 4.5 A), they are far from Tyr_{244}, and their distance with Tyr_{244} is not enough to make H bonds. Thus, the radius of the protein channel is large enough for *CYC* translocation (blue color part of the protein channel), which can permeate from the extracellular milieu. The averaged distance between the C_α's of these amino acids in native and oxidized OF state are presented in

Table 4.3.

Table 4.3 Average distance of the backbones of Cys_{327}/CYO_{327} and Tyr_{244} with Ala_{60} and Gly_{61} in the native and oxidized OF state.

	Cys_{327}/CYO_{327} -Ala_{60} (Å)	Tyr_{244}-Ala_{60} (Å)	Cys_{327}/CYO_{327} -Gly_{61} (Å)	Tyr_{244}-Gly_{61} (Å)
Native OF	5.93 ± 0.02	14.45 ± 0.02	9.07 ± 0.03	11.83 ± 0.02
Oxidized OF	7.23 ± 0.02	8.40 ± 0.02	10.92 ± 0.02	5.51 ± 0.01

It is important to mention that the distance of Ala_{60} and Gly_{61} with CYO_{327} partially increased, whereas their distances with Tyr_{244} decreased noticeably. In general, in the oxidized OF system, these four amino acids (Ala_{60}, Gly_{61}, CYO_{327} and Tyr_{244}) moved toward each other, making the channel more narrow, eventually blocking the protein channel in this area.

We further analyzed the conformational changes by aligning the native and oxidized structures of OF state. Figure 4.6 and 4.7 illustrate the superimposed structures of the native and oxidized OF with details of shift of some transmembrane (TM) domains, i.e., TM3 and TM8 (Figure 4.6) and TM1, TM4, TM5 and TM6 (Figure 4.7). By using VMD software [169], we superimposed the oxidized and native structures, where the Cα's of Cys_{327} and CYO_{327} covered each other (see black circle in Figure 4.6A). It is obvious from Figure 4.6B that TM8 (which contains Cys_{327}/CYO_{327}) slightly moved in the oxidized structure, whereas it was not the case for the TM3 (see Figure 4.6 C). From the latter, we can speculate that the amino acids of the TM3 domain did not affect the closure of the protein channel, as the position of TM3 was not changed.

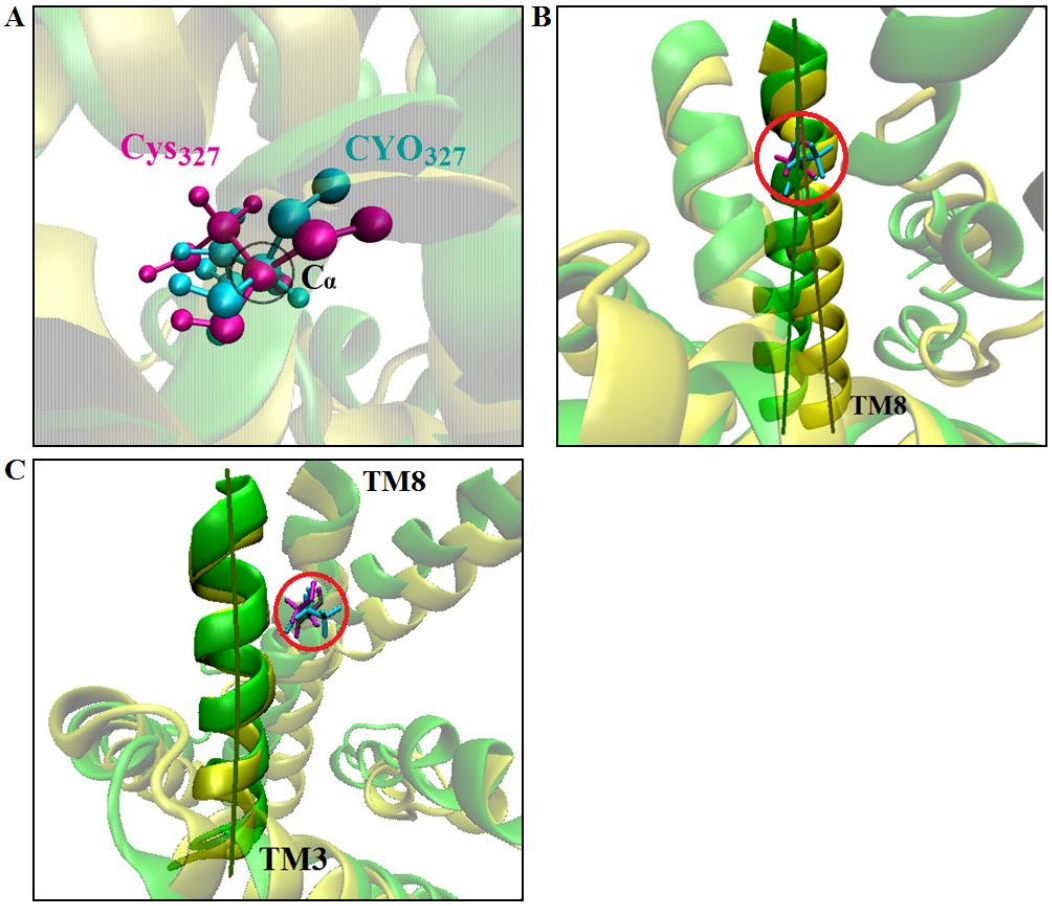

Figure 4.6 Superimposed structures of the native (yellow) and oxidized (green) OF, representing the change of TM8 and TM3 positions. (A) Locations of Cys_{327} (magenta) and CYO_{327} (cyan), having the same Cα positions (see black circle). Comparison of the orientation of TM8 (B) and TM3 (C) in side view. The red circles in (B) and (C) indicate the positions of Cys_{327} and CYO_{327}.

It is clear from Figure 4.7A that the TM6 domain moved towards TM8, after oxidation of Cys_{327}. Moreover, the orientation of Tyr_{244} in TM6 changed and this led Tyr_{244} to become closer to CYO_{327}, compared to the native structure (see Figure 4.7A). We also observed that Lys_{198} of TM5 came closer to CYO_{327} in oxidized structure (see Figure 4.7B and C), which increased the interaction energy between these two residues, forming a salt bridge. This in turn led TM5 to be closer to TM8 (see Figure 4.7C). Furthermore, TM1 also moved towards TM8, which resulted in Ala_{60} and Gly_{61} of TM1 to interact stronger with CYO_{327} of TM8 and Tyr_{244} of TM6 (see Figure 4.7D and E).

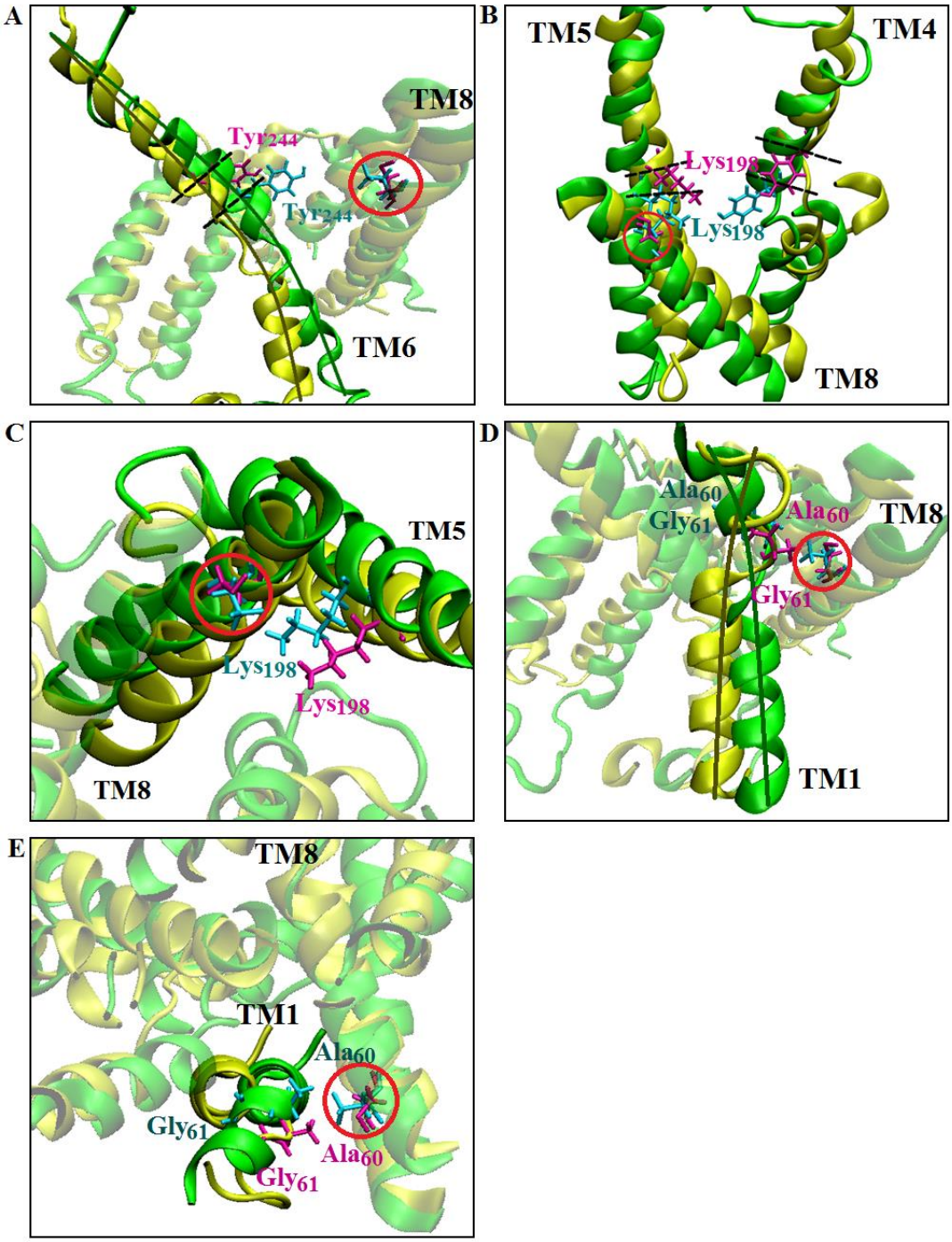

Figure 4.7 Superimposed structures of the native (yellow) and oxidized (green) OF, representing the movements of TM6 (A), TM5 (B and C) and TM1 (D and E) towards TM8. Some important amino acids (i.e., Tyr_{244}, Lys_{198}, Ala_{60} and Gly_{61}) of the native and oxidized OF are depicted in magenta and cyan colors, respectively. Cys327 and CYO_{327} of TM8 are indicated in red circles.

In general, I found that among the TM domains, TM1, TM5 and TM6 moved towards TM8, which resulted in a change of the channel size. This subsequently led to a dramatic increase of the interaction energy between CYO_{327} and other

amino acids (including *Ala*$_{60}$, *Gly*$_{61}$ and *Tyr*$_{244}$) surrounding this residue. This is summarized in Figure 4.8, illustrating the positions of four important amino acids (i.e., *Cys*$_{327}$/*CYO*$_{327}$, *Tyr*$_{244}$, *Ala*$_{60}$ and *Gly*$_{61}$) by superimposing the structures of the native and oxidized OF systems. Hence, we can conclude that the reorientation of these amino acids, and thereby the movement of the TM domains to which they belong, led to a narrowing of the channel after oxidation (cf. also Figure 4.3 and 4.4), resulting in a blocking of the access of CYC to the substrate binding site of the OF system.

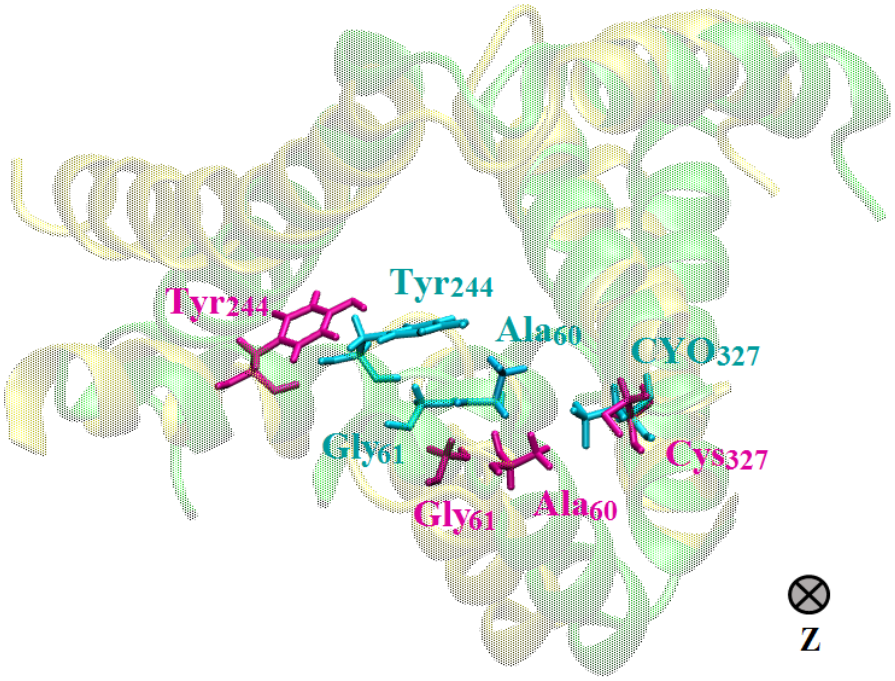

Figure 4.8 Superimposed structures of the native (yellow) and oxidized (green) OF from top view, together with some important amino acids (i.e., Cys$_{327}$*/CYO*$_{327}$*, Tyr*$_{244}$*, Ala*$_{60}$ *and Gly*$_{61}$*) depicted in magenta (native system) and cyan (oxidized system) colors.*

4.3.4 Free energy profiles (FEPs)

The FEPs of *CYC* translocation across the channels of both the native and oxidized OF systems are compared in Figure 4.9.

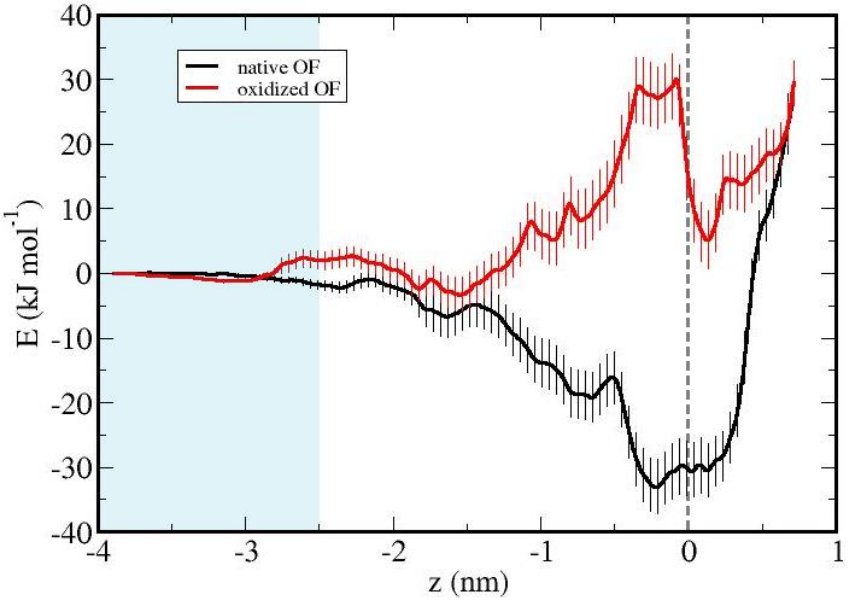

Figure 4.9 Free energy profiles for the translocation of CYC across the native and oxidized OF structures. The position of the center of mass (COM) is indicated by the gray dashed line. The light blue color corresponds to the extracellular water phase.

It is clear that oxidation of Cys_{327} to CYO_{327} and thus the reorientation of this and other residues around the substrate binding site, including Tyr_{244}, creates a free energy barrier of $33.9\ kJ\ mol^{-1}$ for *CYC* translocation, making the *CYC* penetration to the substrate binding site more difficult than in the native OF state. In section 3.5, I found that the free energy barrier of *CYC* translocation through the modified OF state (i.e., Cys_{327} modification to Ala_{327}) was $32.4\ kJ\ mol^{-1}$. Hence, the barrier becomes even higher in the oxidized OF system. My results thus indicate that oxidation of Cys_{327} to CYO_{327}, which can be caused by cold atmospheric plasma (CAP), is more effective than mutation of this amino acid to Ala in inhibition of the xC^- antiporter.

4.4 Investigation of CYC translocation from OF structure located in the native and oxidized POPC

4.4.1 Funnel radii analysis

To investigate the effect of lipid peroxidation on the protein channel, I calculated the funnel radii of the OF, OCC and IF structures located in the membrane with different combinations of POPC and POPX (i.e. 0%, 25%, 50% and 75% POPX). Figure 4.10 shows the profiles of the average funnel radii as a function of position along the transporter axis (i.e., z direction), calculated for the OF, OCC and IF structures.

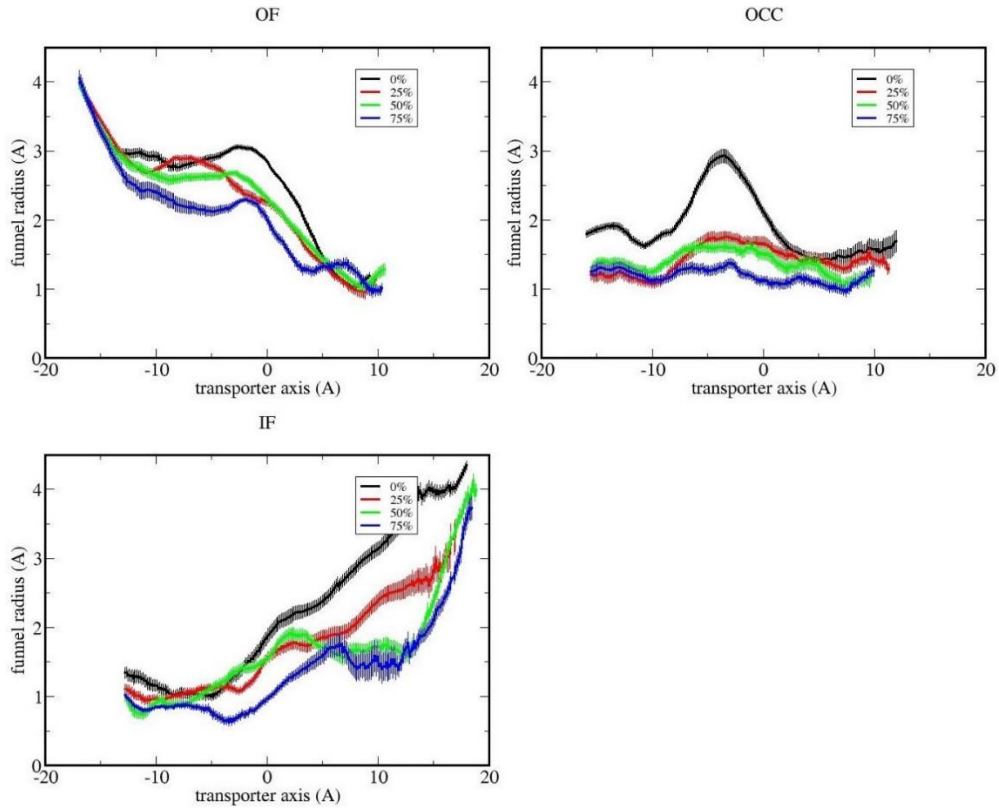

Figure 4.10 Funnel radii versus position along the transporter axis, calculated for the OF, OCC and IF state located into the membrane with 0% (black curve), 25% (red curve), 50% (green curve) and 75% (blue curve) POPX. The radii are averaged over the last 50 ns of the equilibration runs.

The black curves in Figure 4.10 show the average funnel radii of the OF, OCC and IF state placed into the membrane without any oxidation. It is clear that by increasing the percent of oxidation, the OF, OCC and IF channels were more closed. The closure of the channel and reduction of the space in the protein channel can make the *CYC* uptake harder. In fact, based on the study by van der Paal et al [2], if the percentage of POPX increases, the surface area per lipid increases. I did not observe any meaningful change in the total surface area (i.e., total surface area of protein, all POPC and POPX molecules) of the four different systems (i.e. with 0%, 25%, 50% and 75% POPX), so the hydrodynamic pressure on the protein could be increased. This pressure compressed the protein, leading to closure of the protein channel.

4.4.2 Investigation of structures stability

As mentioned in Chapter 1:, the xCT subunit has 12 transmembrane (TM) domains, which are made by an α-helix. These α-helices (TM's) play a critical role in the *CYC* translocation [52, 76]. Reduction of the hydrophobicity of the phospholipid tails, as a result of lipid peroxidation, affected the protein structure

and decreased their stability. By using *gmx DSSP* tool of Gromacs software, I investigated the stability of the protein structures. I analyzed and compared the secondary structure, especially the α-helices of the OF, OCC and IF state placed into the membrane with different combinations of POPC and POPX. The results of this comparison are presented in Table 4.4.

Table 4.4 Secondary structure analysis of the OF, OCC and IF conformations

	α-helix (%)		
	OF	**OCC**	**IF**
0% POPX	64.00±1.16	64.00±1.00	64.00±1.02
25% POPX	63.00±1.38	62.00±1.30	57.00±1.18
50% POPX	63.00±1.21	61.00±1.00	56.00±1.45
75% POPX	63.00±1.17	60.00±1.16	56.00±1.00

The secondary structure analysis of the OF, OCC and IF state located in native POPC (i.e. without any lipid peroxidation) shows that ≈64% of the protein structures are made by α-helices. This percentage, and thus the stability of the OCC and IF conformations, was decreased by increasing the lipid peroxidation of membrane, While in the OF conformation, I did not see any significant changes. In general, the results illustrate that membrane oxidation makes the xCT subunit instable. This instability could disturb the *CYC* translocation.

4.5 **Conclusion**

I investigated the effects of Cys_{327} oxidation in acidic pH on *CYC* translocation across the OF conformation of the xCT subunit of the xC^- antiporter, which might be important as a future cancer therapy target by using CAP. Indeed, in cancer cells an enhanced transport of *CYC* across the xC^- antiporter is observed, and this protects the cancer cells from intracellular oxidative stress. If the *CYC* uptake is inhibited by oxidation of some amino acid residues of the xCT subunit via CAP, this can reduce the cellular protection from oxidative stress, as well as reduce cancer cell drug resistance, eventually leading to cancer cell death.

I applied US simulations to study the permeation of *CYC* across the native and oxidized OF systems, based on Cys_{327} oxidation to cysteic acid (CYO_{327}). The free energy profiles of *CYC* translocation across the native and oxidized OF structures showed that oxidation of Cys_{327} to CYO_{327} makes the *CYC* transportation more difficult, creating a barrier of 33.9 kJ mol^{-1}, thereby leading to a decrease in the *CYC* permeation rate. Comparison of the funnel radii profiles of both the native and oxidized OF states showed that oxidation leads to closure

of the protein channel from the extracellular milieu, so that the substrate binding site is not accessible anymore from outside of the cell. By monitoring the amino acids around the closed part of the oxidized OF state, I found that oxidation results in a rearrangement of the amino acids around the oxidized Cys_{327} in the protein channel. Among these amino acids, Tyr_{244} is the most effective one on closure of the protein channel. This amino acid becomes closer to CYO_{327} by rotating its side chain, whereas CYO_{327} also changes its orientation towards Tyr_{244}, together making the channel narrower. These rearrangements of the amino acid residues form H-bonds with some neighboring amino acids, such as Ala_{60} and Gly_{61}.

Finally, I investigated the effect of lipid peroxidation as a result of CAP interactions, on the funnel radii of the protein channel for OF, OCC and IF state of the xCT subunit. The results showed that, if the percentage of POPX increases, the protein channel of the xCT subunit closes more. Furthermore, oxidation of the membrane decreased the stability of the protein, especially in OCC and IF structures.

This study is important, since it elucidates the effect of oxidation of Cys_{327} on closure of the protein channel, thereby making *CYC* uptake by the xCT subunit of the xC^- antiporter more difficult. This oxidation can happen as a result of e.g., CAP application to cancer cells at acidic *pH*. Hence, this study might explain the possible mechanism of *CYC* starvation in cancer cells, through inhibition of the xC^- antiporter, which results in a depletion of the intracellular level of glutathione, and consequently, in inhibition of cell growth, inducing apoptosis and reducing the cancer cell drug resistance.

4.6 Appendix

Force field parameters for CYO

Parameter file (CYO.prm file)

```
BONDS
SG3O2 OG2P1   642.338     1.42457 ! lig , from OG303 SG3O2, penalty=
140
CT2  SG3O2   206.051     1.76031 ! lig , from OG303 SG3O2, penalty= 140
CT2  HA2     309.000     1.1110  ! lig , from OG303 SG3O2, penalty= 140
CT2  CT1     222.500     1.5380 ! ALLOW   ALI
NH1  CT1   320.000     1.4300 ! ALLOW   ALI PEP POL ARO
HB1  CT1   330.000     1.0800 ! ALLOW   PEP
CT1  C     250.000     1.4900 ! ALLOW   ALI PEP POL ARO
NH1  H     440.000     0.9970 ! ALLOW   PEP POL ARO
O    C     620.000     1.2300 ! ALLOW   PEP POL ARO
NH1  C     370.000     1.3450 ! ALLOW   PEP POL ARO

ANGLES
```

```
OG2P1  SG3O2 OG2P1    137.638     119.301
CT2  SG3O2 OG2P1    146.712     110.240
HA2  CT2   SG3O2     71.248     108.283
CT2  SG3O2 OG2P1    146.712     110.240
CT1  CT2   SG3O2     50.0       114.70    ! From CT-CT-S
NH1  CT1  CT2    70.000   113.5000 ! ALLOW   ALI PEP POL ARO
HB1  CT1  CT2    35.000   111.0000 ! ALLOW  PEP
CT2  CT1  C      52.000   108.0000 ! ALLOW   ALI PEP POL ARO
HA2  CT2  HA2   35.500    109.00    5.40   1.80200 ! ALLOW   ALI
HA2  CT2  CT1   26.500    110.10   22.53   2.17900 ! ALLOW   ALI
H    NH1  CT1    35.000   117.0000 ! ALLOW   PEP POL ARO ALI
O    C    CT1    80.000   121.0000 ! ALLOW   ALI PEP POL ARO
NH1  CT1  HB1    48.000   108.0000 ! ALLOW PEP
NH1  CT1  C      50.000   107.0000 ! ALLOW   PEP POL ARO ALI
HB1  CT1  C      50.000   109.5000 ! ALLOW  PEP
O    C    NH1    80.000   122.5000 ! ALLOW   PEP POL ARO

DIHEDRALS
HA2 CT2 SG3O2 OG2P1               1.318  1    0.000    3.   !    53.40
3 3
CT1    CT2    SG3O2  OG2P1        1.00   3    0.0      3.   ! From X-
CT-S-X
C      CT1    CT2    SG3O2        0.200  3    0.00 ! lig , from C
CT1   CT2   SG311, penalty= 21
NH1    CT1    CT2    SG3O2        0.200  3    0.00 ! lig , from NG3P3
CT1   CT2   SG311, penalty= 21
HB1  CT1  CT2  SG3O2        0.2000  3     0.00 ! From X    CT1  CT2  X
C    CT1  CT2  SG3O2        0.2400  1   180.00
O    C    CT1  CT2       1.4000  1     0.00 ! from O    C    CT1  CT2
or O    C    CT1  CT2 , kevo
HB1  CT1  CT2  HA2          0.2000  3     0.00 ! From X    CT1  CT2  X
C    CT1  CT2  HA2          0.2000  3     0.00 ! From X    CT1  CT2  X
O    C    CT1  NH1      0.0000  1     0.00 !   ALLOW PEP
HB1  CT1  NH1  H         0.0000  1     0.00 ! ALLOW PEP
H    NH1  CT1  C       0.0000  1     0.00 ! from H    NH1  CT1  CT2
O    C    CT1  HB1      0.0000  1     0.00 !   ALLOW PEP
O    C    NH1  H        2.5000  2   180.00 !  ALLOW PEP
END
```

Topology file (CYO.rtf file)

```
* Topologies generated by
* CHARMM General Force Field (CGenFF) program version 1.0.0
*
36 1

! "penalty" is the highest penalty score of the associated parameters.
! Penalties lower than 10 indicate the analogy is fair; penalties
between 10
! and 50 mean some basic validation is recommended; penalties higher
than
! 50 indicate poor analogy and mandate extensive
validation/optimization.
DECL -CA
DECL -C
DECL -O
DECL +N
DECL +HN
DECL +CA
```

```
RESI CYO          -1.00
GROUP
ATOM N    NH1    -0.700112
ATOM HN   H       0.369406
ATOM CA   CT1     0.475074
ATOM HA   HB1    -0.071229
GROUP
ATOM CB   CT2    -0.446008
ATOM HB1  HA2     0.123684
ATOM HB2  HA2     0.133442
GROUP
ATOM S1   SG3O2   1.298653
ATOM O1   OG2P1      -0.718056
ATOM O2   OG2P1      -0.719429
ATOM O3   OG2P1    -0.711852
GROUP
ATOM C    C         0.079459
ATOM O    O       -0.113032
BOND CB CA   S1 CB   N HN  N  CA
BOND C  CA  C +N      CA HA  CB HB1
BOND CB HB2  S1 O1   S1 O2   S1 O3
DOUBLE O  C
IMPR N -C CA HN  C CA +N O
CMAP -C  N  CA  C   N  CA  C  +N
END
```

MD simulations

Figure 4.11 illustrates the root mean squared deviation (RMSD) of the backbones of the native and oxidized OF proteins. It is clear that both structures reach their equilibrated state after 400 ns simulation. The final RMSD values were obtained to be fluctuating around 0.25 and 0.3 nm for the native and oxidized OF structure, respectively.

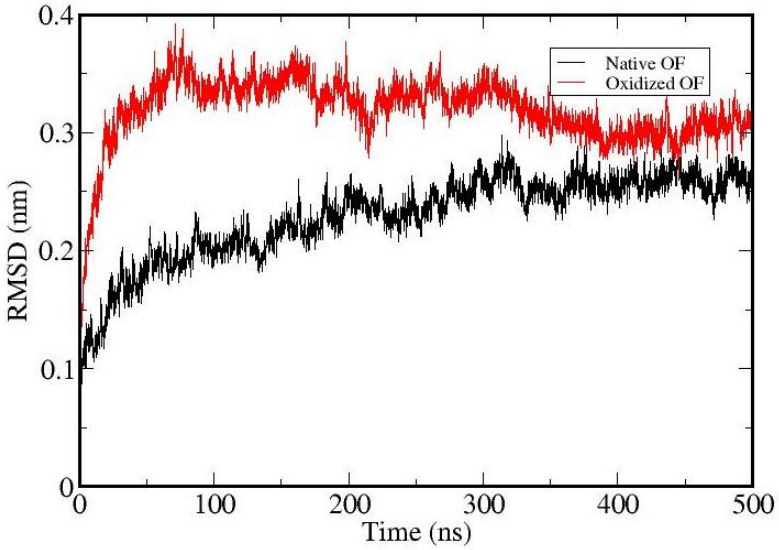

Figure 4.11 Root mean squared deviation (RMSD) of the backbones of the native and oxidized OF conformations of the xCT subunit. Both structures reach their equilibration after 400 ns simulation.

Summary

The application of cold atmospheric plasma (CAP) in medicine and biology, especially in cancer treatment, requires control over the processes occurring in the plasma and of the interaction mechanism of plasma species with biochemical structures. CAP can selectively treat cancer cells, without or with minimal damage to normal cells. Despite many experimental studies that have been performed on CAP-based cancer treatment, there is still limited fundamental knowledge regarding the relevant interaction mechanisms of plasma species with cancer cells. Complementary to experimental studies, computer simulations may provide fundamental information about the occurring processes, both in the plasma and in interaction with cells, which is difficult or even impossible to obtain through experiments.

The membranes of normal and cancer cells contain proteins and lipids. Among the important proteins, transporters, such as xC^- antiporter, have a critical role in the cell viability. This antiporter is responsible for extracellular to intracellular translocation of cysteine or its oxidized dimer form, i.e. cystine (*CYC*), which is essential for general protein biosynthesis, specifically glutathione. Hence, inhibition of *CYC* uptake in cancer cells as a result of alteration of some residues in its structure, and consequently, reduction of glutathione, not only inhibits cancer cell growth, but also reduces drug resistance.

Based on these consideration, I applied several different simulation techniques, to investigate the transport of *CYC* through xCT, the light subunit of the xC^- antiporter, which is responsible for the translocation of *CYC* and *Glu*. Specifically, I studied the permeation of *CYC* across three model systems, i.e., outward facing (OF), occluded (OCC) and inward facing (IF) configurations of xCT. I also investigated the effect of mutation of Cys_{327} residue, located in the vicinity of the extracellular milieu to *Ala* within xCT, which was also studied experimentally in literature. This allowed me to qualitatively compare my computation results with experimental observations, and thus, to validate my simulations. My simulations provide a molecular level mechanism of the transport of *CYC* across the xC^- antiporter, more specifically, which amino acid residues in the xC^- antiporter play a key role in the uptake, transport and release of *CYC*.

Besides, I performed MD simulations to investigate the effect of oxidation (as can be induced by CAP) on the extracellular *CYC* uptake by xCT. I considered the

OF configuration of xCT, and to study the effect of oxidation, I modified *Cys327* to cysteic acid (*CYO327*), which is the product of *Cys* oxidation in acidic *pH* and in vicinity of H_2O_2, OH° and O_2^-, which are all found in CAP.

Transport of cystine across xC⁻ antiporter

A better understanding of the mechanism of *CYC* translocation across the xC⁻ antiporter at the molecular level can lead to finding more effective methods for inhibiting *CYC* uptake. After construction of three model systems (i.e., the OF, OCC and IF structures), I simulated the permeation of *CYC* across these systems, applying different simulation techniques. The accuracy of these model systems was verified using ERRAT, Verify3D, Procheck and PSQS and the structures of their channels were determined by calculation of their funnel radii.

By applying SMD simulation to pull *CYC* through its substrate binding site in the OF structure, *CYC* was trapped between *Arg135* and *Arg396*, which causes a strong electrostatic attraction with *CYC* substrate. In this thesis, I investigated the non-bonded energy between *CYC* and all amino acids of the OF, OCC and IF structure, located at a distance less than 12 Å from *CYC*, and I determined the seven mostly interacting amino acids. *Arg135*, *Arg396* and *Arg126* had strong attractive interaction with *CYC* in the OF structure. On the other hand, *Glu130* exhibited a strong repulsive interaction. Transition from OF to OCC as well as OCC to IF structure, using TMD simulations, led to a change in the position of the amino acid residues, including those located in the substrate binding site. Although the attractive energy between *CYC* and *Arg396* reduced, due to an increasing distance between them, the energy increased between *CYC* and *Lys198*. Moreover, *Arg135* was still the most attractively interacting amino acid with *CYC* in OCC conformation. In the IF structure, *Lys198* played an important role in the substrate binding site. Furthermore, the attractive energy of *Arg135* was decreased in IF conformation compared to OF and OCC structures. In general, the total non-bonded energy between *CYC* and all residues found within 12 Å from *CYC*, was equal to $-53.68 \pm 0.67\ kJ.mol^{-1}$, $-55.23 \pm 0.12\ kJ.mol^{-1}$ and $-42.72 \pm 0.50\ kJ.mol^{-1}$ for the OF, OCC and IF structures, respectively.

The free energy profiles of *CYC* across the OF, OCC and IF structures, calculated with US simulations, showed that the minimum energy of *CYC* is higher in the IF conformation. This indicates that a lower energy is required to release *CYC* from the antiporter. These free energy minima were -33.09 ± 4.16 kJ mol^{-1} and -17.14 ± 2.38 kJ mol^{-1}, for the OF and IF structures, respectively. Finally, I studied the effect of the mutation of *Cys327* to *Ala* in the OF structure, by calculating

the free energy profiles of the native and mutated OF structures, again with US simulations. The mutation of Cys_{327} to *Ala* in the OF structure created an extra barrier of $32.4\ \mathrm{kJmol^{-1}}$, in the free energy profile, making the *CYC* transportation across the xCT antiporter more difficult, and eventually leading to a decrease of the *CYC* permeation rate. This is in qualitative agreement with experiments.

This study is important, since it elucidates the molecular level mechanisms of the CYC uptake by the xCT subunit of the xC^- antiporter, which affects the intracellular oxidative stress. Hence, this insight might be highly relevant for new cancer therapy studies.

Effect of oxidative stress on cystine transportation by xC^- antiporter

My computational results show that oxidation of Cys_{327} results in a free energy barrier for *CYC* translocation, thereby blocking the access of *CYC* to the substrate binding site of the OF system. The formation of the energy barrier was found to be due to the conformational changes in the channel. Analysis of the MD trajectories revealed that the reorganization of the side chains of the Tyr_{244} and CYO_{327} residues play a critical role in the OF channel blocking. Indeed, the calculated distance between Tyr_{244} and either Cys_{327} or CYO_{327} showed a narrowing of the channel after oxidation. The obtained free energy barrier for *CYC* translocation was found to be $33.9\ \mathrm{kJmol^{-1}}$, indicating that oxidation of Cys_{327}, by e.g., CAP, is more effective in inhibiting the xC^- antiporter than the mutation of this amino acid to *Ala* (yielding a barrier of $32.4\ \mathrm{kJmol^{-1}}$). The inhibition of the xC^- antiporter may lead to *Cys* starvation in some cancer cells, eventually resulting in cancer cell death.

Finally, I investigated the effect of lipid oxidation as a result of CAP interaction, on the funnel radii of the protein channel for the OF, OCC and IF state of the xCT subunit and stability of the xCT structure. The results showed that, by increasing the percentage of POPC (i.e. 1-palmitoyl-2-oleoyl-sn-glycero-3-phosphocholine) oxidation, the protein channel of the xCT subunit will be more compact. Furthermore, due to the oxidation of the membrane, the stability of the xCT structure, especially in the OCC and IF configuration, decreased.

Outlook for future work

In subsequent studies, it would be interesting to simulate the interaction of plasma species with other amino acids of the xCT subunit or other transporters. Based on literature, phosphorylation of Ser_{26} of the xCT subunit also inhibits *CYC*

uptake [187]. Hence, studying the oxidation of other amino acid residues of the xCT subunit, which are in the vicinity of the extracellular milieu, can be helpful to find the best methods for inhibiting the *CYC* uptake, using CAP treatment. Moreover, quantum mechanical MD simulations would make it possible to investigate the dynamics of the reactions of CAP species with Cys_{327}, or to gain understanding on the possible mechanisms of the interaction. Finally, by using US simulation, we can find whether the closure of the xCT subunit channel as a result of lipid oxidation, will be effective on decreasing the *CYC* uptake or not.

Samenvatting

De toepassing van koud atmosferisch plasma (cold atmospheric plasma; CAP) in de geneeskunde en biologie, met name bij de behandeling van kanker, vereist controle over de processen die in het plasma plaatsvinden en van het interactiemechanisme van plasmadeeltjes met biochemische structuren. CAP kan selectief kankercellen behandelen, zonder of met minimale schade aan de normale cellen. Ondanks vele experimentele onderzoeken die reeds werden uitgevoerd voor de CAP-behandeling van kanker, is er nog steeds een beperkte kennis van de relevante interactiemechanismen van de plasmadeeltjes met kankercellen. Naast experimentele studies kunnen computersimulaties fundamentele informatie verschaffen over de onderliggende processen, zowel in het plasma als in interactie met cellen, die vaak moeilijk of zelfs onmogelijk te verkrijgen zijn door experimenten.

De membranen van normale cellen en kankercellen bevatten eiwitten en lipiden. Transporters, zoals xC^- antiporter, zijn belangrijke eiwitten die een cruciale rol spelen in de overlevingskansen van cellen. Deze antiporter is verantwoordelijk voor extracellulaire naar intracellulaire translocatie van cysteïne of de geoxideerde dimeervorm ervan, d.w.z. cystine (CYC), die essentieel is voor algemene eiwitbiosynthese, met name glutathion. Daarom remt de opname van CYC in kankercellen als gevolg van wijziging van sommige residuen in de structuur ervan en bijgevolg vermindering van glutathion niet alleen de groei van kankercellen, maar vermindert ook de resistentie tegen geneesmiddelen.

Op basis van deze argumenten heb ik verschillende simulatietechnieken toegepast om het transport van CYC door xCT, de lichte subeenheid van de xC^- antiporter, die verantwoordelijk is voor de translocatie van CYC en Glu, te onderzoeken. Specifiek bestudeerde ik de permeatie van CYC in drie modelsystemen, d.w.z. naar buiten gerichte (outward facing; OF), “occluded” (OCC) en naar binnen gerichte (inward facing; IF) configuraties van xCT. Ik onderzocht ook het effect van mutatie van Cys_{327}-residu, gelokaliseerd in de nabijheid van het extracellulaire milieu, naar Ala binnen xCT, dat ook experimenteel in de literatuur werd bestudeerd. Dit stelde me in staat om mijn berekeningsresultaten kwalitatief te vergelijken met experimentele waarnemingen en zo mijn simulaties te valideren. Mijn simulaties verschaffen inzicht in het mechanisme op moleculair niveau van het transport van CYC door de xC^- antiporter, meer specifiek, welke aminozuurresiduen in de xC^- antiporter een sleutelrol spelen bij de opname, transport en afgifte van CYC.

Daarnaast heb ik MD simulaties uitgevoerd om het effect van oxidatie (zoals kan worden geïnduceerd door CAP) op de extracellulaire CYC-opname door xCT te

onderzoeken. Ik heb de OF-configuratie van xCT beschouwd en om het effect van oxidatie te bestuderen, heb ik Cys_{327} gewijzigd in cysteïnezuur (CYO_{327}), wat het product is van Cys-oxidatie in zure pH en onder invloed van buurt van H_2O_2, OH° en O_2^-, die allemaal te vinden zijn in CAP.

Transport van cystine door xC⁻ antiporter

Een beter begrip van het mechanisme van CYC-translocatie door de xC^- antiporter op moleculair niveau, kan leiden tot het vinden van effectievere methoden voor het remmen van de opname van CYC. Na de bouw van drie modelsystemen (d.w.z. de OF-, OCC- en IF-structuren), heb ik de permeatie van CYC in deze systemen gesimuleerd, waarbij verschillende simulatietechnieken werden toegepast. De nauwkeurigheid van deze modelsystemen werd geverifieerd met behulp van ERRAT, Verify3D, Procheck en PSQS en de structuren van de kanalen van deze modelsystemen werden bepaald door berekening van hun "trechter" stralen.

Op basis van SMD-simulaties om CYC door zijn substraatbindingsplaats in de OF-structuur te trekken, vond ik dat CYC gevangen zat tussen Arg_{135} en Arg_{396}, wat een sterke elektrostatische aantrekking met CYC-substraat veroorzaakt. In dit proefschrift onderzocht ik de niet-gebonden energie tussen CYC en alle aminozuren van de OF-, OCC- en IF-structuur, gelokaliseerd op een afstand van minder dan 12 Å van CYC, en ik kon de zeven aminozuren bepalen die de belangrijkste wisselwerking uitoefenden. Arg_{135}, Arg_{396} en Arg_{126} hadden een sterke aantrekkingsinteractie met CYC in de OF-structuur. Aan de andere kant vertoonde Glu_{130} een sterke afstotingsinteractie. Overgang van OF naar OCC evenals OCC naar IF-structuur, met behulp van TMD-simulaties, leidde tot een verandering in de positie van de aminozuurresiduen, inclusief die zich in de substraatbindingsplaats bevinden. Terwijl de aantrekkingsenergie tussen CYC en Arg_{396} afnam, als gevolg van een toenemende afstand tussen hen, nam de energie toe tussen CYC en Lys_{198}. Bovendien oefende Arg_{135} nog steeds de belangrijkste aantrekkingskracht uit op CYC in OCC-conformatie. In de IF-structuur speelde Lys_{198} een belangrijke rol in de substraatbindingsplaats. Bovendien was de aantrekkingsenergie van Arg_{135} vergeleken met OF- en OCC-structuren afgenomen in IF-conformatie vergeleken met de OF- en OCC-structuren. In het algemeen was de totale niet-gebonden energie tussen CYC en alle residuen gevonden binnen 12 Å van CYC gelijk aan $-53.68 \pm 0.67\ kJ.mol^{-1}$, $-55.23 \pm 0.12\ kJ.mol^{-1}$ en $-42.72 \pm 0.50\ kJ.mol^{-1}$ voor respectievelijk de OF-, OCC- en IF-structuren.

De vrije energieprofielen van CYC over de OF-, OCC- en IF-structuren, berekend met US simulaties, toonden aan dat de minimale energie van CYC hoger is in de IF-conformatie. Dit geeft aan dat een lagere energie nodig is om CYC uit de antiporter af te geven. Deze vrije energieminima waren respectievelijk -33,09 ± 4,16 kJ mol^{-1} en -17,14 ± 2,38 kJ mol^{-1}, voor de OF- en IF-structuren. Ten slotte

heb ik het effect van de mutatie van Cys_{327} naar Ala in de OF-structuur bestudeerd, door de vrije energieprofielen van de oorspronkelijke en gemuteerde OF-structuren te berekenen, opnieuw met US simulaties. De mutatie van Cys_{327} naar Ala in de OF-structuur creëerde een extra barrière van 32,4 kJ mol^{-1}, in het vrije energieprofiel, waardoor het CYC-transport over de xCT^- antiporter moeilijker werd en uiteindelijk leidde tot een afname van de CYC-permeatiesnelheid. Dit komt kwalitatief overeen met experimenten.

Deze studie is belangrijk, omdat het de mechanismen op moleculair niveau van de CYC-opname door de xCT-subeenheid van de xC^- antiporter opheldert, die de intracellulaire oxidatieve stress beïnvloedt. Daarom kan dit inzicht zeer relevant zijn voor nieuwe onderzoeken naar kankertherapie.

Effect van oxidatieve stress op cystinetransport door xC^- antiporter

Mijn berekeningsresultaten tonen aan dat oxidatie van Cys_{327} resulteert in een vrije energiebarrière voor CYC-translocatie, waardoor de toegang van CYC tot de substraatbindingsplaats van het OF-systeem wordt geblokkeerd. De vorming van de energiebarrière bleek te wijten aan de conformationele veranderingen in het kanaal. Analyse van de MD-trajecten onthulde dat de reorganisatie van de zijketens van de Tyr_{244} en CYO_{327} residuen een cruciale rol speelt in de OF-kanaalblokkering. De berekende afstand tussen Tyr_{244} en Cys_{327} of CYO_{327} vertoonde inderdaad een vernauwing van het kanaal na oxidatie. De berekende vrije energiebarrière voor CYC-translocatie was 33,9 kJ mol^{-1}, wat aangeeft dat oxidatie van Cys^{327}, door bijvoorbeeld CAP, effectiever is bij het remmen van de xC^- antiporter dan bij de mutatie van dit aminozuur naar Ala (hetgeen een barrière van 32,4 kJ mol^{-1} oplevert). De remming van de xC^- antiporter kan leiden tot Cys-uithongering in sommige kankercellen, wat uiteindelijk kan leiden tot de dood van kankercellen.

Tot slot onderzocht ik het effect van lipide-oxidatie als gevolg van CAP-interacties op de trechterstralen van het eiwitkanaal voor de OF-, OCC- en IF-toestand van de xCT-subeenheid en de stabiliteit van de xCT-structuur. De resultaten toonden aan dat, door het percentage POPC (d.w.z. 1-palmitoyl-2-oleoyl-sn-glycero-3-fosfocholine) oxidatie te verhogen, het eiwitkanaal van de xCT-subeenheid compacter zal zijn. Verder nam door de oxidatie van het membraan de stabiliteit van de xCT-structuur, vooral in de OCC- en IF-configuratie, af.

Ideeën voor toekomstig onderzoek

In vervolgstudies zou het interessant zijn om de interactie van plasmadeeltjes met andere aminozuren van de xCT-subeenheid of andere transporters te simuleren. Gebaseerd op literatuur, remt fosforylering van Ser_{26} van de xCT-subeenheid ook de CYC-opname [187]. Daarom kan het bestuderen van de oxidatie van andere aminozuurresiduen van de xCT-subeenheid, die zich in de buurt van het extracellulaire milieu bevinden, nuttig zijn om de beste methoden te vinden voor

het remmen van de opname van CYC, met behulp van CAP-behandeling. Bovendien zou het gebruik van kwantummechanische MD-simulaties het mogelijk maken om de dynamica van de reacties van CAP-deeltjes met Cys_{327} te bestuderen, of meer inzicht te krijgen in de mogelijke interactiemechanismen. Tenslotte kunnen we met behulp van US simulaties zien of de sluiting van het xCT-subeenheidkanaal als gevolg van lipide-oxidatie effectief zal zijn bij het verminderen van de CYC-opname of niet.

Academic curriculum vitae

List of publications included in this thesis

1. **M. Ghasemitarei**, M. Yusupov, J. Razzokov, B. Shokri, A. Bogaerts, Transport of cystine across xC− antiporter, Archives of biochemistry and biophysics 664 (2019) 117-126.
2. **M. Ghasemitarei**, M. Yusupov, J. Razzokov, B. Shokri, A. Bogaerts, Effect of oxidative stress on cystine transportation by xC^- antiporter, Archives of biochemistry and biophysics (2019) 108114.

Conference contributions

1. Parisa Shali, Pegah Asadi, **Maryam Ghasemitarei**, Fateme Rezaei, Neda Hafez Khiabani, Mohammad Asna Ashari, Babak Shokri, "*In vitro decontamination of infected tooth root canals by single electrode plasma jet*", 22nd International Symposium on Plasma, Belgium (2015)
2. Morteza Akhlaghi, **Maryam Ghasemitarei** , Hamed Mehdikia, Shahriar Mashayekh, Hajar rajaee, Mohammadreza Khani, Babak Shokri, "*Parametric study of interaction between Lung cancer and cold atmospheric plasma*", 3th National Conference in Plasma Engineering and Physics, Tabriz, Iran (2015)
3. Morteza Akhlaghi, **Maryam Ghasemitarei** ,Shahriar Mashayekh, Marefat Feyzi, Mohammadreza Khani, Babak Shokri, " *Construction and characterization of a new cold plasma jet suitable for biological and medical application*", 1th International Plasma Technologies Congress, Kayseri, Turkey (2014)
4. **Maryam Ghasemitarei**, Mohammadali Ansari, Ahmad Amjadi, "*Study of light depolarization in biological tissue by means of the Monte Carlo simulation*", 11th Iranian conference of Medical Science, Tehran, Iran (2014)
5. Morteza Akhlaghi, **Maryam Ghasemi Tarei** ,Shahriar Mashayekh, Hajar rajaee, Mohammadreza Khani, Babak Shokri, "*Study of cold atmospheric plasma effects on lung cancer cells*", 11th Iranian conference of Medical Science, Tehran, Iran (2014)
6. Morteza Akhlaghi, Shahriar Mashayekh, Hajar rajaee, **Maryam Ghasemi**

Tarei, Mohammadreza Khani, Babak Shokri, "*Feasibility of breast cancer treatment by cold atmospheric plasma*", 11th Iranian conference of Medical Science, Tehran, Iran (2014)

Bibliography

[1] D. Dobrynin, G. Fridman, G. Friedman, A. Fridman, Physical and biological mechanisms of direct plasma interaction with living tissue, New Journal of Physics 11(11) (2009) 115020.
[2] J. Van der Paal, E.C. Neyts, C.C. Verlackt, A. Bogaerts, Effect of lipid peroxidation on membrane permeability of cancer and normal cells subjected to oxidative stress, Chemical science 7(1) (2016) 489-498.
[3] R. Ranjan, P. Krishnamraju, T. Shankar, S. Gowd, Nonthermal plasma in dentistry: an update, Journal of International Society of Preventive & Community Dentistry 7(3) (2017) 71.
[4] G. Fridman, M. Peddinghaus, M. Balasubramanian, H. Ayan, A. Fridman, A. Gutsol, A. Brooks, Blood coagulation and living tissue sterilization by floating-electrode dielectric barrier discharge in air, Plasma Chemistry and plasma processing 26(4) (2006) 425-442.
[5] M. Keidar, A. Shashurin, O. Volotskova, M. Ann Stepp, P. Srinivasan, A. Sandler, B. Trink, Cold atmospheric plasma in cancer therapy, Physics of Plasmas 20(5) (2013) 057101.
[6] S. Fathollah, S. Mirpour, P. Mansouri, A.R. Dehpour, M. Ghoranneviss, N. Rahimi, Z.S. Naraghi, R. Chalangari, K.M. Chalangari, Investigation on the effects of the atmospheric pressure plasma on wound healing in diabetic rats, Scientific reports 6 (2016) 19144.
[7] E.A. Ratovitski, X. Cheng, D. Yan, J.H. Sherman, J. Canady, B. Trink, M. Keidar, Anti-cancer therapies of 21st century: novel approach to treat human cancers using cold atmospheric plasma, Plasma Processes and Polymers 11(12) (2014) 1128-1137.
[8] G. Fridman, A. Shereshevsky, M.M. Jost, A.D. Brooks, A. Fridman, A. Gutsol, V. Vasilets, G. Friedman, Floating electrode dielectric barrier discharge plasma in air promoting apoptotic behavior in melanoma skin cancer cell lines, Plasma Chemistry and Plasma Processing 27(2) (2007) 163-176.
[9] M. Laroussi, From killing bacteria to destroying cancer cells: 20 years of plasma medicine, Plasma Processes and Polymers 11(12) (2014) 1138-1141.
[10] S. Mashayekh, H. Rajaee, M. Akhlaghi, B. Shokri, Z.M. Hassan, Atmospheric-pressure plasma jet characterization and applications on melanoma cancer treatment (B/16-F10), Physics of Plasmas 22(9) (2015) 093508.
[11] X. Yan, Z. Xiong, F. Zou, S. Zhao, X. Lu, G. Yang, G. He, K. Ostrikov, Plasma-induced death of HepG2 cancer cells: intracellular effects of reactive species, Plasma Processes and Polymers 9(1) (2012) 59-66.
[12] H. Lee, C. Shon, Y. Kim, S. Kim, G. Kim, M.G. Kong, Degradation of adhesion molecules of G361 melanoma cells by a non-thermal atmospheric pressure microplasma, New Journal of Physics 11(11) (2009) 115026.
[13] X. Cheng, W. Murphy, N. Recek, D. Yan, U. Cvelbar, A. Vesel, M. Mozetič, J. Canady, M. Keidar, J.H. Sherman, Synergistic effect of gold nanoparticles and cold plasma on glioblastoma cancer therapy, Journal of Physics D: Applied Physics 47(33) (2014) 335402.
[14] N. Barekzi, M. Laroussi, Dose-dependent killing of leukemia cells by low-temperature plasma, Journal of Physics D: Applied Physics 45(42) (2012) 422002.
[15] G.-Y. Liou, P. Storz, Reactive oxygen species in cancer, Free radical research 44(5) (2010) 479-496.
[16] M. Keidar, R. Walk, A. Shashurin, P. Srinivasan, A. Sandler, S. Dasgupta, R. Ravi, R. Guerrero-Preston, B. Trink, Cold plasma selectivity and the possibility of a paradigm shift in cancer therapy, British journal of cancer 105(9) (2011) 1295.
[17] R.A. Cairns, I.S. Harris, T.W. Mak, Regulation of cancer cell metabolism, Nature Reviews Cancer 11 (2011) 85.
[18] D. Yan, A. Talbot, N. Nourmohammadi, J.H. Sherman, X. Cheng, M. Keidar, Toward understanding the selective anticancer capacity of cold atmospheric plasma—A model based on aquaporins, Biointerphases 10(4) (2015) 040801.

[19] D. Yan, H. Xiao, W. Zhu, N. Nourmohammadi, L.G. Zhang, K. Bian, M. Keidar, The role of aquaporins in the anti-glioblastoma capacity of the cold plasma-stimulated medium, Journal of Physics D: Applied Physics 50(5) (2017) 055401.
[20] S. Zhao, Z. Xiong, X. Mao, D. Meng, Q. Lei, Y. Li, P. Deng, M. Chen, M. Tu, X. Lu, Atmospheric pressure room temperature plasma jets facilitate oxidative and nitrative stress and lead to endoplasmic reticulum stress dependent apoptosis in HepG2 cells, PloS one 8(8) (2013) e73665.
[21] D. Yan, A. Talbot, N. Nourmohammadi, X. Cheng, J. Canady, J. Sherman, M. Keidar, Principles of using cold atmospheric plasma stimulated media for cancer treatment, Scientific reports 5 (2015) 18339.
[22] E. Cabiscol, J. Ros, Oxidative damage to proteins: structural modifications and consequences in cell function, Redox proteomics: from protein modification to cellular dysfunction and disease (2006) 399-471.
[23] M. Yusupov, J.W. Lackmann, J. Razzokov, S. Kumar, K. Stapelmann, A. Bogaerts, Impact of plasma oxidation on structural features of human epidermal growth factor, Plasma Processes and Polymers 15(8) (2018) 1800022.
[24] L. Gibellini, M. Pinti, M. Nasi, S. De Biasi, E. Roat, L. Bertoncelli, A. Cossarizza, Interfering with ROS metabolism in cancer cells: the potential role of quercetin, Cancers 2(2) (2010) 1288-1311.
[25] S.G. Rhee, H2O2, a necessary evil for cell signaling, Science 312(5782) (2006) 1882-1883.
[26] H. Pelicano, D. Carney, P. Huang, ROS stress in cancer cells and therapeutic implications, Drug resistance updates 7(2) (2004) 97-110.
[27] D.A. Tennant, R.V. Durán, H. Boulahbel, E. Gottlieb, Metabolic transformation in cancer, Carcinogenesis 30(8) (2009) 1269-1280.
[28] T. Pfeiffer, S. Schuster, S. Bonhoeffer, Cooperation and competition in the evolution of ATP-producing pathways, Science 292(5516) (2001) 504-507.
[29] A.L. Rubin, B.J. Ellison, Induction of transformation in NIH3T3 cells by moderate growth constraint: evidence that neoplasia is driven by adaptational change, Carcinogenesis 12(10) (1991) 1801-1806.
[30] Y. Hu, D.G. Rosen, Y. Zhou, L. Feng, G. Yang, J. Liu, P. Huang, Mitochondrial manganese-superoxide dismutase expression in ovarian cancer role in cell proliferation and response to oxidative stress, Journal of Biological Chemistry 280(47) (2005) 39485-39492.
[31] E.O. Hileman, J. Liu, M. Albitar, M.J. Keating, P. Huang, Intrinsic oxidative stress in cancer cells: a biochemical basis for therapeutic selectivity, Cancer chemotherapy and pharmacology 53(3) (2004) 209-219.
[32] I. Dalle-Donne, D. Giustarini, R. Colombo, R. Rossi, A. Milzani, Protein carbonylation in human diseases, Trends in molecular medicine 9(4) (2003) 169-176.
[33] T. Nyström, Role of oxidative carbonylation in protein quality control and senescence, The EMBO journal 24(7) (2005) 1311-1317.
[34] I. Dalle-Donne, G. Aldini, M. Carini, R. Colombo, R. Rossi, A. Milzani, Protein carbonylation, cellular dysfunction, and disease progression, Journal of cellular and molecular medicine 10(2) (2006) 389-406.
[35] I. Dalle-Donne, R. Rossi, D. Giustarini, N. Gagliano, L. Lusini, A. Milzani, P. Di Simplicio, R. Colombo, Actin carbonylation: from a simple marker of protein oxidation to relevant signs of severe functional impairment, Free Radical Biology and Medicine 31(9) (2001) 1075-1083.
[36] D. Trachootham, J. Alexandre, P. Huang, Targeting cancer cells by ROS-mediated mechanisms: a radical therapeutic approach?, Nature reviews Drug discovery 8(7) (2009) 579.
[37] H. Sies, Glutathione and its role in cellular functions, Free Radical Biology and Medicine 27(9-10) (1999) 916-921.
[38] M. Lo, Y.Z. Wang, P.W. Gout, The x cystine/glutamate antiporter: A potential target for therapy of cancer and other diseases, Journal of cellular physiology 215(3) (2008) 593-602.
[39] M. Lo, V. Ling, Y. Wang, P. Gout, The xc− cystine/glutamate antiporter: a mediator of pancreatic cancer growth with a role in drug resistance, British journal of cancer 99(3) (2008) 464-472.

[40] J. Guan, M. Lo, P. Dockery, S. Mahon, C.M. Karp, A.R. Buckley, S. Lam, P.W. Gout, Y.-Z. Wang, The x c− cystine/glutamate antiporter as a potential therapeutic target for small-cell lung cancer: use of sulfasalazine, Cancer chemotherapy and pharmacology 64(3) (2009) 463-472.
[41] D.L. Nelson, A.L. Lehninger, M.M. Cox, Lehninger principles of biochemistry, Macmillan2008.
[42] S.A. El-Debaiky, Antagonistic studies and hyphal interactions of the new antagonist Aspergillus piperis against some phytopathogenic fungi in vitro in comparison with Trichoderma harzianum, Microbial pathogenesis 113 (2017) 135-143.
[43] D.A. Dougherty, Cation-π interactions involving aromatic amino acids, The Journal of nutrition 137(6) (2007) 1504S-1508S.
[44] G.D. Fasman, Practical handbook of biochemistry and molecular biology, CRC press1989.
[45] J. Lewerenz, R. Dargusch, P. Maher, Lactacidosis modulates glutathione metabolism and oxidative glutamate toxicity, Journal of neurochemistry 113(2) (2010) 502-514.
[46] M. Bassi, E. Gasol, M. Manzoni, M. Pineda, M. Riboni, R. Martín, A. Zorzano, G. Borsani, M. Palacín, Identification and characterisation of human xCT that co-expresses, with 4F2 heavy chain, the amino acid transport activity system x c–, Pflügers Archiv 442(2) (2001) 286-296.
[47] G. Khelashvili, H. Weinstein, Functional mechanisms of neurotransmitter transporters regulated by lipid–protein interactions of their terminal loops, Biochimica et Biophysica Acta (BBA)-Biomembranes 1848(9) (2015) 1765-1774.
[48] R.J. Kathawala, P. Gupta, C.R. Ashby Jr, Z.-S. Chen, The modulation of ABC transporter-mediated multidrug resistance in cancer: a review of the past decade, Drug resistance updates 18 (2015) 1-17.
[49] X. Zha, Z. Hu, S. Ji, F. Jin, K. Jiang, C. Li, P. Zhao, Z. Tu, X. Chen, L. Di, NFκB up-regulation of glucose transporter 3 is essential for hyperactive mammalian target of rapamycin-induced aerobic glycolysis and tumor growth, Cancer letters 359(1) (2015) 97-106.
[50] M.H. Saier Jr, V.S. Reddy, D.G. Tamang, Å. Västermark, The transporter classification database, Nucleic acids research 42(D1) (2013) D251-D258.
[51] E. Padan, H. Michel, NhaA: A unique structural fold of secondary active transporters, Israel Journal of Chemistry 55(11-12) (2015) 1233-1239.
[52] E.M. Quistgaard, C. Löw, F. Guettou, P. Nordlund, Understanding transport by the major facilitator superfamily (MFS): structures pave the way, Nature Reviews Molecular Cell Biology 17(2) (2016) 123.
[53] J. Chillaron, R. Roca, A. Valencia, A. Zorzano, M. Palacín, Heteromeric amino acid transporters: biochemistry, genetics, and physiology, American Journal of Physiology-Renal Physiology 281(6) (2001) F995-F1018.
[54] H. Gmünder, H.-P. Eck, B. Benninghoff, S. Roth, W. Dröge, Macrophages regulate intracellular glutathione levels of lymphocytes. Evidence for an immunoregulatory role of cysteine, Cellular immunology 129(1) (1990) 32-46.
[55] T.B. Levring, M. Kongsbak, A.K.O. Rode, A. Woetmann, N. Ødum, C.M. Bonefeld, C. Geisler, Human CD4+ T cells require exogenous cystine for glutathione and DNA synthesis, Oncotarget 6(26) (2015) 21853.
[56] G. Wu, Y.-Z. Fang, S. Yang, J.R. Lupton, N.D. Turner, Glutathione metabolism and its implications for health, The Journal of nutrition 134(3) (2004) 489-492.
[57] X. Yu, Y.C. Long, Crosstalk between cystine and glutathione is critical for the regulation of amino acid signaling pathways and ferroptosis, Scientific reports 6 (2016) 30033.
[58] Y. Dun, B. Mysona, T. Van Ells, L. Amarnath, M.S. Ola, V. Ganapathy, S.B. Smith, Expression of the cystine-glutamate exchanger (x c−) in retinal ganglion cells and regulation by nitric oxide and oxidative stress, Cell and tissue research 324(2) (2006) 189-202.
[59] J. Lewerenz, S.J. Hewett, Y. Huang, M. Lambros, P.W. Gout, P.W. Kalivas, A. Massie, I. Smolders, A. Methner, M. Pergande, The cystine/glutamate antiporter system xc− in health and disease: from molecular mechanisms to novel therapeutic opportunities, Antioxidants & redox signaling 18(5) (2013) 522-555.
[60] A.L. Edinger, C.B. Thompson, Antigen-presenting cells control T cell proliferation by regulating amino acid availability, Proceedings of the National Academy of Sciences 99(3) (2002) 1107-1109.

[61] R.J. Bridges, N.R. Natale, S.A. Patel, System xc-cystine/glutamate antiporter: an update on molecular pharmacology and roles within the CNS, British journal of pharmacology 165(1) (2012) 20-34.
[62] L.M. Slosky, N.M. BassiriRad, A.M. Symons, M. Thompson, T. Doyle, B.L. Forte, W.D. Staatz, L. Bui, W.L. Neumann, P.W. Mantyh, The cystine/glutamate antiporter system xc− drives breast tumor cell glutamate release and cancer-induced bone pain, Pain 157(11) (2016) 2605.
[63] K. Linher-Melville, M.G. Nashed, R. Ungard, S. Haftchenary, P.T. Gunning, G. Singh, Abstract P3-03-13: Chronic inhibition of signal transducer and activator of transcription 3/5 in treatment-resistant human breast cancer cell subtypes: Convergence on the reactive oxyten species/SUMOylation pathway and its effects on xCT expression and system xc-activity, AACR, 2017.
[64] P.W. Gout, Y.J. Kang, D.J. Buckley, N. Bruchovsky, A.R. Buckley, Increased cystine uptake capability associated with malignant progression of Nb2 lymphoma cells, Leukemia 11(8) (1997) 1329.
[65] J. Liu, L. Feng, E.M. Stone, J. Tyler, S.W. Rowlinson, M.J. Keating, P. Huang, Targeting chronic lymphocytic leukemia by interfering glutathione synthesis using a novel therapeutic enzyme cyst (e) inase (AEB3103), AACR, 2016.
[66] K. Tsuchihashi, S. Okazaki, M. Ohmura, M. Ishikawa, O. Sampetrean, N. Onishi, H. Wakimoto, M. Yoshikawa, R. Seishima, Y. Iwasaki, The EGF Receptor Promotes the Malignant Potential of Glioma by Regulating Amino Acid Transport System xc (—), Cancer research 76(10) (2016) 2954-2963.
[67] S. Lanzardo, L. Conti, R. Rooke, R. Ruiu, N. Accart, E. Bolli, M. Arigoni, M. Macagno, G. Barrera, S. Pizzimenti, Immunotargeting of antigen xCT attenuates stem-like cell behavior and metastatic progression in breast cancer, Cancer research 76(1) (2016) 62-72.
[68] L. Dai, Y. Cao, Y. Chen, C. Parsons, Z. Qin, Targeting xCT, a cystine-glutamate transporter induces apoptosis and tumor regression for KSHV/HIV-associated lymphoma, Journal of hematology & oncology 7(1) (2014) 30.
[69] M.-z. Ma, G. Chen, P. Wang, W.-h. Lu, C.-f. Zhu, M. Song, J. Yang, S. Wen, R.-h. Xu, Y. Hu, Xc− inhibitor sulfasalazine sensitizes colorectal cancer to cisplatin by a GSH-dependent mechanism, Cancer letters 368(1) (2015) 88-96.
[70] L. Sleire, B.S. Skeie, I.A. Netland, H.E. Førde, E. Dodoo, F. Selheim, L. Leiss, J.I. Heggdal, P.H. Pedersen, J. Wang, Drug repurposing: sulfasalazine sensitizes gliomas to gamma knife radiosurgery by blocking cystine uptake through system Xc−, leading to glutathione depletion, Oncogene 34(49) (2015) 5951.
[71] J.-L. Roh, E.H. Kim, H. Jang, D. Shin, Aspirin plus sorafenib potentiates cisplatin cytotoxicity in resistant head and neck cancer cells through xCT inhibition, Free Radical Biology and Medicine 104 (2017) 1-9.
[72] W. Wang, I. Kryczek, L. Dostál, H. Lin, L. Tan, L. Zhao, F. Lu, S. Wei, T. Maj, D. Peng, Effector T cells abrogate stroma-mediated chemoresistance in ovarian cancer, Cell 165(5) (2016) 1092-1105.
[73] D. Patel, P.S. Kharkar, M. Nandave, Emerging roles of system antiporter and its inhibition in CNS disorders, Molecular membrane biology 32(4) (2015) 89-116.
[74] H. Sato, M. Tamba, T. Ishii, S. Bannai, Cloning and expression of a plasma membrane cystine/glutamate exchange transporter composed of two distinct proteins, Journal of Biological Chemistry 274(17) (1999) 11455-11458.
[75] F. Verrey, E.I. Closs, C.A. Wagner, M. Palacin, H. Endou, Y. Kanai, CATs and HATs: the SLC7 family of amino acid transporters, Pflügers Archiv 447(5) (2004) 532-542.
[76] D. Fotiadis, Y. Kanai, M. Palacín, The SLC3 and SLC7 families of amino acid transporters, Molecular aspects of medicine 34(2-3) (2013) 139-158.
[77] M. Jiménez-Vidal, E. Gasol, A. Zorzano, V. Nunes, M. Palacín, J. Chillarón, Thiol modification of cysteine 327 in the eighth transmembrane domain of the light subunit xCT of the heteromeric cystine/glutamate antiporter suggests close proximity to the substrate binding site/permeation pathway, Journal of Biological Chemistry 279(12) (2004) 11214-11221.
[78] L. Gardner, P.G. Corn, Hypoxic regulation of mRNA expression, Cell Cycle 7(13) (2008) 1916-1924.
[79] J.R. Cantor, D.M. Sabatini, Cancer cell metabolism: one hallmark, many faces, Cancer discovery

2(10) (2012) 881-898.
[80] T. Ishimoto, O. Nagano, T. Yae, M. Tamada, T. Motohara, H. Oshima, M. Oshima, T. Ikeda, R. Asaba, H. Yagi, CD44 variant regulates redox status in cancer cells by stabilizing the xCT subunit of system xc− and thereby promotes tumor growth, Cancer cell 19(3) (2011) 387-400.
[81] L. Martin, L. Gardner, Stress-induced inhibition of nonsense-mediated RNA decay regulates intracellular cystine transport and intracellular glutathione through regulation of the cystine/glutamate exchanger SLC7A11, Oncogene 34(32) (2015) 4211-4218.
[82] R.A. Gatenby, R.J. Gillies, Why do cancers have high aerobic glycolysis?, Nature Reviews Cancer 4(11) (2004) 891-899.
[83] H. Izumi, T. Torigoe, H. Ishiguchi, H. Uramoto, Y. Yoshida, M. Tanabe, T. Ise, T. Murakami, T. Yoshida, M. Nomoto, Cellular pH regulators: potentially promising molecular targets for cancer chemotherapy, Cancer treatment reviews 29(6) (2003) 541-549.
[84] S. Bannai, E. Kitamura, Role of proton dissociation in the transport of cystine and glutamate in human diploid fibroblasts in culture, Journal of Biological Chemistry 256(11) (1981) 5770-5772.
[85] S. Bannai, H. Sato, T. Ishii, Y. Sugita, Induction of cystine transport activity in human fibroblasts by oxygen, Journal of Biological Chemistry 264(31) (1989) 18480-18484.
[86] W. Vogt, Oxidation of methionyl residues in proteins: tools, targets, and reversal, Free Radical Biology and Medicine 18(1) (1995) 93-105.
[87] A.R. Katritzky, N.G. Akhmedov, O.V. Denisko, 1H and 13C NMR spectroscopic study of oxidation of d, l-cystine and 3, 3′-dithiobis (propionic acid) with hydrogen peroxide in aqueous solution, Magnetic Resonance in Chemistry 41(1) (2003) 37-41.
[88] J.W. Purdie, γ radiolysis of cystine in aqueous solution. Dose-rate effects and a proposed mechanism, Journal of the American Chemical Society 89(2) (1967) 226-230.
[89] T. Enache, A. Oliveira-Brett, Boron doped diamond and glassy carbon electrodes comparative study of the oxidation behaviour of cysteine and methionine, Bioelectrochemistry 81(1) (2011) 46-52.
[90] P.L. Shaffer, A. Goehring, A. Shankaranarayanan, E. Gouaux, Structure and mechanism of a Na+-independent amino acid transporter, Science 325(5943) (2009) 1010-1014.
[91] Y. Shi, Common folds and transport mechanisms of secondary active transporters, Annual review of biophysics 42 (2013) 51-72.
[92] B.J. Alder, T.E. Wainwright, Phase transition for a hard sphere system, The Journal of chemical physics 27(5) (1957) 1208-1209.
[93] D. Frenkel, B. Smit, Understanding molecular simulation: From algorithms to applications, Elsevier (formerly published by Academic Press), 2002, pp. 1-638.
[94] R. Car, M. Parrinello, Unified approach for molecular dynamics and density-functional theory, Physical review letters 55(22) (1985) 2471.
[95] J. Li, P.-C. Wen, M. Moradi, E. Tajkhorshid, Computational characterization of structural dynamics underlying function in active membrane transporters, Current opinion in structural biology 31 (2015) 96-105.
[96] J.S. Patel, A. Berteotti, S. Ronsisvalle, W. Rocchia, A. Cavalli, Steered molecular dynamics simulations for studying protein–ligand interaction in cyclin-dependent kinase 5, Journal of chemical information and modeling 54(2) (2014) 470-480.
[97] P. Ferrara, J. Apostolakis, A. Caflisch, Targeted molecular dynamics simulations of protein unfolding, The Journal of Physical Chemistry B 104(18) (2000) 4511-4518.
[98] K. Kappel, Y. Miao, J.A. McCammon, Accelerated molecular dynamics simulations of ligand binding to a muscarinic G-protein-coupled receptor, Quarterly reviews of biophysics 48(4) (2015) 479-487.
[99] A.J. Clark, P. Tiwary, K. Borrelli, S. Feng, E.B. Miller, R. Abel, R.A. Friesner, B.J. Berne, Prediction of protein–ligand binding poses via a combination of induced fit docking and metadynamics simulations, Journal of chemical theory and computation 12(6) (2016) 2990-2998.
[100] J. Kästner, Umbrella sampling, Wiley Interdisciplinary Reviews: Computational Molecular Science 1(6) (2011) 932-942.
[101] M. Gur, E. Zomot, M.H. Cheng, I. Bahar, Energy landscape of LeuT from molecular simulations,

The Journal of chemical physics 143(24) (2015) 12B611_1.
[102] H.D. Song, F. Zhu, Conformational changes in two inter-helical loops of Mhp1 membrane transporter, PloS one 10(7) (2015) e0133388.
[103] A.J. Stone, The theory of intermolecular forces. Clarendon, Oxford, 1996.
[104] M. Sprik, Effective pair potentials and beyond, Computer simulation in chemical physics, Springer1993, pp. 211-259.
[105] G.C. Maitland, Intermolecular forces: their origin and determination, Oxford University Press1981.
[106] M. Kouza, Numerical Simulation of Folding and Unfolding of Proteins, arXiv preprint arXiv:1308.2380 (2013).
[107] L. Verlet, Computer" experiments" on classical fluids. I. Thermodynamical properties of Lennard-Jones molecules, Physical review 159(1) (1967) 98.
[108] J. Wang, R.M. Wolf, J.W. Caldwell, P.A. Kollman, D. Case, Erratum: Development and testing of a general amber force field (Journal of Computational Chemistry (2004) 25 (1157)), Journal of Computational Chemistry 26(1) (2005).
[109] K. Vanommeslaeghe, E. Hatcher, C. Acharya, S. Kundu, S. Zhong, J. Shim, E. Darian, O. Guvench, P. Lopes, I. Vorobyov, CHARMM general force field: A force field for drug-like molecules compatible with the CHARMM all-atom additive biological force fields, Journal of computational chemistry 31(4) (2010) 671-690.
[110] W.L. Jorgensen, D.S. Maxwell, J. Tirado-Rives, Development and testing of the OPLS all-atom force field on conformational energetics and properties of organic liquids, Journal of the American Chemical Society 118(45) (1996) 11225-11236.
[111] C. Oostenbrink, A. Villa, A.E. Mark, W.F. Van Gunsteren, A biomolecular force field based on the free enthalpy of hydration and solvation: the GROMOS force-field parameter sets 53A5 and 53A6, Journal of computational chemistry 25(13) (2004) 1656-1676.
[112] S.J. Marrink, H.J. Risselada, S. Yefimov, D.P. Tieleman, A.H. De Vries, The MARTINI force field: coarse grained model for biomolecular simulations, The journal of physical chemistry B 111(27) (2007) 7812-7824.
[113] I.R. Cooke, K. Kremer, M. Deserno, Tunable generic model for fluid bilayer membranes, Physical Review E 72(1) (2005) 011506.
[114] J.B. Klauda, R.M. Venable, J.A. Freites, J.W. O'Connor, D.J. Tobias, C. Mondragon-Ramirez, I. Vorobyov, A.D. MacKerell Jr, R.W. Pastor, Update of the CHARMM all-atom additive force field for lipids: validation on six lipid types, The journal of physical chemistry B 114(23) (2010) 7830-7843.
[115] P. Bjelkmar, P. Larsson, M.A. Cuendet, B. Hess, E. Lindahl, Implementation of the CHARMM force field in GROMACS: analysis of protein stability effects from correction maps, virtual interaction sites, and water models, Journal of Chemical Theory and Computation 6(2) (2010) 459-466.
[116] K. Vanommeslaeghe, A.D. MacKerell Jr, Automation of the CHARMM General Force Field (CGenFF) I: bond perception and atom typing, Journal of chemical information and modeling 52(12) (2012) 3144-3154.
[117] K. Vanommeslaeghe, E.P. Raman, A.D. MacKerell Jr, Automation of the CHARMM General Force Field (CGenFF) II: assignment of bonded parameters and partial atomic charges, Journal of chemical information and modeling 52(12) (2012) 3155-3168.
[118] J.B.J. Chapman, Improving the Functional Control of Ferroelectrics Using Insights from Atomistic Modelling, (2018).
[119] H. Bekker, J.P. Van Den Berg, T.A. Wassenaar, A method to obtain a near-minimal-volume molecular simulation of a macromolecule, using periodic boundary conditions and rotational constraints, Journal of computational chemistry 25(8) (2004) 1037-1046.
[120] J. Razzokov, Molecular level simulations for plasma medicine applications, (2019).
[121] T. Kraska, Molecular-dynamics simulation of argon nucleation from supersaturated vapor in the NVE ensemble, The Journal of chemical physics 124(5) (2006) 054507.
[122] S. Nosé, A molecular dynamics method for simulations in the canonical ensemble, Molecular

physics 52(2) (1984) 255-268.
[123] H.C. Andersen, Molecular dynamics simulations at constant pressure and/or temperature, The Journal of chemical physics 72(4) (1980) 2384-2393.
[124] G.C. Lynch, B.M. Pettitt, Grand canonical ensemble molecular dynamics simulations: Reformulation of extended system dynamics approaches, The Journal of chemical physics 107(20) (1997) 8594-8610.
[125] P.H. Hünenberger, Thermostat algorithms for molecular dynamics simulations, Advanced computer simulation, Springer2005, pp. 105-149.
[126] W.G. Hoover, Canonical dynamics: Equilibrium phase-space distributions, Physical review A 31(3) (1985) 1695.
[127] H.J.C. Berendsen, J.P.M.v. Postma, W.F. van Gunsteren, A. DiNola, J.R. Haak, Molecular dynamics with coupling to an external bath, The Journal of chemical physics 81(8) (1984) 3684-3690.
[128] V. Rühle, Berendsen and nose-hoover thermostats, Am. J. Phys (2007).
[129] Y. Zhao, Brief introduction to the thermostats, Tech. Rep. Research-Cerca con Google.
[130] S. Izrailev, S. Stepaniants, B. Isralewitz, D. Kosztin, H. Lu, F. Molnar, W. Wriggers, K. Schulten, Steered molecular dynamics, Computational molecular dynamics: challenges, methods, ideas, Springer1999, pp. 39-65.
[131] G. Binnig, C.F. Quate, C. Gerber, Atomic force microscope, Physical review letters 56(9) (1986) 930.
[132] D.J. Brockwell, Probing the mechanical stability of proteins using the atomic force microscope, Portland Press Limited, 2007.
[133] K. Svoboda, S.M. Block, Biological applications of optical forces, Annual review of biophysics and biomolecular structure 23(1) (1994) 247-285.
[134] L. Novotny, R.X. Bian, X.S. Xie, Theory of nanometric optical tweezers, Physical Review Letters 79(4) (1997) 645.
[135] M. Dienerowitz, M. Mazilu, K. Dholakia, Optical manipulation of nanoparticles: a review, Journal of Nanophotonics 2(1) (2008) 021875.
[136] C. Gourier, A. Jegou, J. Husson, F. Pincet, A nanospring named erythrocyte. The biomembrane force probe, Cellular and Molecular Bioengineering 1(4) (2008) 263.
[137] J.C. Phillips, R. Braun, W. Wang, J. Gumbart, E. Tajkhorshid, E. Villa, C. Chipot, R.D. Skeel, L. Kale, K. Schulten, Scalable molecular dynamics with NAMD, Journal of computational chemistry 26(16) (2005) 1781-1802.
[138] J. Schlitter, M. Engels, P. Krüger, Targeted molecular dynamics: a new approach for searching pathways of conformational transitions, Journal of molecular graphics 12(2) (1994) 84-89.
[139] J. Schlitter, M. Engels, P. Krüger, E. Jacoby, A. Wollmer, Targeted molecular dynamics simulation of conformational change-application to the T↔ R transition in insulin, Molecular Simulation 10(2-6) (1993) 291-308.
[140] S. Kumar, J.M. Rosenberg, D. Bouzida, R.H. Swendsen, P.A. Kollman, The weighted histogram analysis method for free-energy calculations on biomolecules. I. The method, Journal of computational chemistry 13(8) (1992) 1011-1021.
[141] C. Daday, M. Bauer, P. Redondo, H.E. Gaub, D. Lietha, F. Gräter, Unfolding Focal Adhesion Kinase: Getting Cellular Insight Through AFM and MD, Biophysical Journal 116(3) (2019) 429a.
[142] N. Rathore, Q. Yan, J.J. de Pablo, Molecular simulation of the reversible mechanical unfolding of proteins, The Journal of chemical physics 120(12) (2004) 5781-5788.
[143] J.A. Lemkul, D.R. Bevan, Assessing the stability of Alzheimer's amyloid protofibrils using molecular dynamics, The Journal of Physical Chemistry B 114(4) (2010) 1652-1660.
[144] A.K. Pathak, T. Bandyopadhyay, Unbinding free energy of acetylcholinesterase bound oxime drugs along the gorge pathway from metadynamics-umbrella sampling investigation, Proteins: Structure, Function, and Bioinformatics 82(9) (2014) 1799-1818.
[145] S.J. Irudayam, M.L. Berkowitz, Binding and reorientation of melittin in a POPC bilayer: Computer simulations, Biochimica et Biophysica Acta (BBA)-Biomembranes 1818(12) (2012) 2975-2981.

[146] F. Meng, W. Xu, Drug permeability prediction using PMF method, Journal of molecular modeling 19(3) (2013) 991-997.
[147] J. Razzokov, M. Yusupov, R.M. Cordeiro, A. Bogaerts, Atomic scale understanding of the permeation of plasma species across native and oxidized membranes, Journal of Physics D: Applied Physics 51(36) (2018) 365203.
[148] M.S. Smyth, J.H.J. Martin, x Ray crystallography, Molecular Pathology 53(1) (2000) 8.
[149] M. Palacín, E. Errasti-Murugarren, A. Rosell, Heteromeric amino acid transporters. In search of the molecular bases of transport cycle mechanisms, Biochemical Society Transactions 44(3) (2016) 745-752.
[150] R. Rodriguez, G. Chinea, N. Lopez, T. Pons, G. Vriend, Homology modeling, model and software evaluation: three related resources, Bioinformatics (Oxford, England) 14(6) (1998) 523-528.
[151] G. Ciccotti, M. Ferrario, Dynamical non-equilibrium molecular dynamics, Entropy 16(1) (2014) 233-257.
[152] A. Waterhouse, M. Bertoni, S. Bienert, G. Studer, G. Tauriello, R. Gumienny, F.T. Heer, T.A.P. de Beer, C. Rempfer, L. Bordoli, SWISS-MODEL: homology modelling of protein structures and complexes, Nucleic acids research 46(W1) (2018) W296-W303.
[153] X. Gao, L. Zhou, X. Jiao, F. Lu, C. Yan, X. Zeng, J. Wang, Y. Shi, Mechanism of substrate recognition and transport by an amino acid antiporter, Nature 463(7282) (2010) 828.
[154] H. Berman, K. Henrick, H. Nakamura, Announcing the worldwide protein data bank, Nature Structural & Molecular Biology 10(12) (2003) 980.
[155] H. Nielsen, J. Engelbrecht, G. von Heijne, S. Brunak, Defining a similarity threshold for a functional protein sequence pattern: the signal peptide cleavage site, Proteins: Structure, Function, and Bioinformatics 24(2) (1996) 165-177.
[156] L. Kowalczyk, M. Ratera, A. Paladino, P. Bartoccioni, E. Errasti-Murugarren, E. Valencia, G. Portella, S. Bial, A. Zorzano, I. Fita, Molecular basis of substrate-induced permeation by an amino acid antiporter, Proceedings of the National Academy of Sciences 108(10) (2011) 3935-3940.
[157] D. Ma, P. Lu, C. Yan, C. Fan, P. Yin, J. Wang, Y. Shi, Structure and mechanism of a glutamate–GABA antiporter, Nature 483(7391) (2012) 632.
[158] E. Gasol, M. Jiménez-Vidal, J. Chillarón, A. Zorzano, M. Palacín, Membrane topology of system xc-light subunit reveals a re-entrant loop with substrate-restricted accessibility, Journal of Biological Chemistry 279(30) (2004) 31228-31236.
[159] M.A. Lomize, I.D. Pogozheva, H. Joo, H.I. Mosberg, A.L. Lomize, OPM database and PPM web server: resources for positioning of proteins in membranes, Nucleic acids research 40(D1) (2011) D370-D376.
[160] S. Jo, T. Kim, V.G. Iyer, W. Im, CHARMM-GUI: a web-based graphical user interface for CHARMM, Journal of computational chemistry 29(11) (2008) 1859-1865.
[161] E.L. Wu, X. Cheng, S. Jo, H. Rui, K.C. Song, E.M. Dávila-Contreras, Y. Qi, J. Lee, V. Monje-Galvan, R.M. Venable, CHARMM-GUI membrane builder toward realistic biological membrane simulations, Journal of computational chemistry 35(27) (2014) 1997-2004.
[162] D. van der Spoel, P.J. van Maaren, C. Caleman, GROMACS molecule & liquid database, Bioinformatics 28(5) (2012) 752-753.
[163] R.A. Gaussian, 1, mj frisch, gw trucks, hb schlegel, ge scuseria, ma robb, jr cheeseman, g. Scalmani, v. Barone, b. Mennucci, ga petersson et al., gaussian, Inc., Wallingford CT 121 (2009) 150-166.
[164] J. Pontius, J. Richelle, S.J. Wodak, Deviations from standard atomic volumes as a quality measure for protein crystal structures, Journal of molecular biology 264(1) (1996) 121-136.
[165] R.B. Best, X. Zhu, J. Shim, P.E.M. Lopes, J. Mittal, M. Feig, A.D. MacKerell Jr, Optimization of the additive CHARMM all-atom protein force field targeting improved sampling of the backbone φ, ψ and side-chain χ1 and χ2 dihedral angles, Journal of chemical theory and computation 8(9) (2012) 3257-3273.
[166] D.J. Evans, B.L. Holian, The nose–hoover thermostat, The Journal of chemical physics 83(8)

(1985) 4069-4074.
[167] M. Parrinello, A. Rahman, Polymorphic transitions in single crystals: A new molecular dynamics method, Journal of Applied physics 52(12) (1981) 7182-7190.
[168] O.S. Smart, J.G. Neduvelil, X. Wang, B.A. Wallace, M.S.P. Sansom, HOLE: a program for the analysis of the pore dimensions of ion channel structural models, Journal of molecular graphics 14(6) (1996) 354-360.
[169] W. Humphrey, A. Dalke, K. Schulten, VMD: visual molecular dynamics, Journal of molecular graphics 14(1) (1996) 33-38.
[170] S. Pronk, S. Páll, R. Schulz, P. Larsson, P. Bjelkmar, R. Apostolov, M.R. Shirts, J.C. Smith, P.M. Kasson, D. Van Der Spoel, GROMACS 4.5: a high-throughput and highly parallel open source molecular simulation toolkit, Bioinformatics 29(7) (2013) 845-854.
[171] M.J. Abraham, T. Murtola, R. Schulz, S. Páll, J.C. Smith, B. Hess, E. Lindahl, GROMACS: High performance molecular simulations through multi-level parallelism from laptops to supercomputers, SoftwareX 1 (2015) 19-25.
[172] W.L. DeLano, Pymol: An open-source molecular graphics tool, CCP4 Newsletter On Protein Crystallography 40(1) (2002) 82-92.
[173] J.S. Hub, B.L. De Groot, D. Van Der Spoel, g_wham・ A Free Weighted Histogram Analysis Implementation Including Robust Error and Autocorrelation Estimates, Journal of Chemical Theory and Computation 6(12) (2010) 3713-3720.
[174] B.J. Williams, C.K. Barlow, K.L. Kmiec, W.K. Russell, D.H. Russell, Negative ion fragmentation of cysteic acid containing peptides: cysteic acid as a fixed negative charge, Journal of The American Society for Mass Spectrometry 22(9) (2011) 1622-1630.
[175] M. Ghasemitarei, M. Yusupov, J. Razzokov, B. Shokri, A. Bogaerts, Transport of cystine across xC− antiporter, Archives of biochemistry and biophysics 664 (2019) 117-126.
[176] E.L. Wu, X. Cheng, S. Jo, H. Rui, K.C. Song, E.M. Dávila-Contreras, Y. Qi, J. Lee, V. Monje-Galvan, R.M. Venable, J.B. Klauda, W. Im, CHARMM-GUI Membrane Builder toward realistic biological membrane simulations, Journal of Computational Chemistry 35(27) (2014) 1997-2004.
[177] A. Frisch, H.P. Hratchian, R.D. Dennington Ii, T.A. Keith, J. Millam, B. Nielsen, A.J. Holder, J. Hiscocks, GaussView Version 5.0. 8, Gaussian, Inc., Wallingford, CT (2009).
[178] T. Darden, D. York, L. Pedersen, Particle mesh Ewald: An N· log (N) method for Ewald sums in large systems, The Journal of chemical physics 98(12) (1993) 10089-10092.
[179] U. Essmann, L. Perera, M.L. Berkowitz, T. Darden, H. Lee, L.G. Pedersen, A smooth particle mesh Ewald method, The Journal of chemical physics 103(19) (1995) 8577-8593.
[180] R.A. Gaussian09, 1, MJ Frisch, GW Trucks, HB Schlegel, GE Scuseria, MA Robb, JR Cheeseman, G. Scalmani, V. Barone, B. Mennucci, GA Petersson et al., Gaussian, Inc., Wallingford CT 121 (2009) 150-166.
[181] L. Martínez, R. Andrade, E.G. Birgin, J.M. Martínez, PACKMOL: a package for building initial configurations for molecular dynamics simulations, Journal of computational chemistry 30(13) (2009) 2157-2164.
[182] J. Wong-Ekkabut, Z. Xu, W. Triampo, I.M. Tang, D.P. Tieleman, L. Monticelli, Effect of lipid peroxidation on the properties of lipid bilayers: a molecular dynamics study, Biophysical journal 93(12) (2007) 4225-4236.
[183] O.S. Smart, J.G. Neduvelil, X. Wang, B. Wallace, M.S. Sansom, HOLE: a program for the analysis of the pore dimensions of ion channel structural models, Journal of molecular graphics 14(6) (1996) 354-360.
[184] D. Xu, S.I. Jalal, G.W. Sledge, S.O. Meroueh, Small-molecule binding sites to explore protein–protein interactions in the cancer proteome, Molecular BioSystems 12(10) (2016) 3067-3087.
[185] E.-M. Krammer, K. Ghaddar, B. André, M. Prévost, Unveiling the mechanism of arginine transport through AdiC with molecular dynamics simulations: the guiding role of aromatic residues, PloS one 11(8) (2016) e0160219.
[186] H.S. Biswal, P.R. Shirhatti, S. Wategaonkar, O− H··· O versus O− H··· S Hydrogen Bonding I:

Experimental and Computational Studies on the p-Cresol· H2O and p-Cresol· H2S Complexes, The Journal of Physical Chemistry A 113(19) (2009) 5633-5643.
[187] Y. Gu, C.P. Albuquerque, D. Braas, W. Zhang, G.R. Villa, J. Bi, S. Ikegami, K. Masui, B. Gini, H. Yang, mTORC2 regulates amino acid metabolism in cancer by phosphorylation of the cystine-glutamate antiporter xCT, Molecular cell 67(1) (2017) 128-138.